

**COMPACT HARSH ENVIRONMENT ENERGY CONVERSION SYSTEMS**

A Dissertation

by

**SHEHAB AHMED**

Submitted to the Office of Graduate Studies of  
Texas A&M University  
in partial fulfillment of the requirements for the degree of

**DOCTOR OF PHILOSOPHY**

May 2007

Major Subject: Electrical Engineering

# COMPACT HARSH ENVIRONMENT ENERGY CONVERSION SYSTEMS

A Dissertation

by

SHEHAB AHMED

Submitted to the Office of Graduate Studies of  
Texas A&M University  
in partial fulfillment of the requirements for the degree of

DOCTOR OF PHILOSOPHY

Approved by:

Chair of Committee,  
Committee Memembers,

Head of Department,

Hamid Toliyat  
Prasad Enjeti  
Shankar Bhattacharyya  
Alan Palazzolo  
Costas N. Georghiades

May 2007

Major Subject: Electrical Engineering

**ABSTRACT**

Compact Harsh Environment Energy Conversion Systems.

(May 2007)

Shehab Ahmed, B.S., Alexandria University, Egypt;

M.S., Texas A&M University

Chair of Advisory Committee: Dr. Hamid Toliyat

The quest for energy is leading the industry into drilling deeper wells. Typically, a temperature gradient of  $1^{\circ}\text{C}/150\text{ ft}$  can be expected, with bottom hole temperatures reaching beyond  $200^{\circ}\text{C}$  in many areas of the world. Moreover, the increased recovery benefits and cost reductions possible with the use of horizontal and multilateral wells has triggered a need for higher power energy conversion systems in bottom hole assemblies, such as rotary steerable tools and downhole tractors. The concepts developed throughout this work address some of these new needs.

This research investigated improvements, novel solutions and considerations that will lead to significant advantages in terms of reliability, extended temperature operation, increased power capability and reduced size and cost of compact harsh environment energy conversion systems. Improvements to both the electromechanical subsystem and the power electronic subsystem are introduced.

Air gap viscous losses were shown to have a significant effect on the optimal design of submersible PM (permanent magnet) machines, and a design procedure to

account for this loss component in the design was developed. The application of a dual winding exterior rotor PM machine in a downhole environment enabled a significant increase in the application's torque capability, provided protection against generator winding over voltage, and reduced parts count. Comprehensive switching device qualification, testing, and simulation lead to a simple failure mitigation technique for the operation of the most suitable devices at elevated temperature. A flying capacitor multilevel inverter was then successfully constructed and temperature tested. A novel motor drive concept suited for elevated temperature oil filled environment applications concluded the research.

In The Name of Allah, Most Gracious, Most Merciful:

To Allah Almighty:

All praise be to Him, The Lord of the Worlds

To My Family:

with love and prayer

## ACKNOWLEDGMENTS

I would like to express my heartfelt gratitude to Dr. Toliyat for his continuous support, guidance and encouragement throughout my studies. Not being under his direct supervision during the largest portion of this work did make it hard; however, he was always willing to help and support. I would also like to extend my thanks to the other committee members for serving on my committee and for their contributions toward my studies. I also wish to acknowledge the huge support of everyone at Schlumberger Technology Corporation for helping bring this work to reality, and for providing me with the opportunity to do many things that really weren't crucial for the project's success, but mattered most for this work.

I would also like to thank all my family members for their love and support in all my endeavors. And to my great friends, your care and support was always a great motivation. Lastly, my wife and life partner and our little one, Abdurrahman, you sacrificed a lot to help me bring this to completion, and I wanted to thank you from the bottom of my heart.

## TABLE OF CONTENTS

CHAPTER	Page
I INTRODUCTION.....	1
1.1. Introduction.....	1
1.2. Components of a Compact Harsh Environment Energy Conversion System.....	3
1.2.1. Electromechanical Subsystem.....	3
1.2.2. Power Electronics Subsystem.....	5
1.3. Objective of the Research.....	6
1.4. Dissertation Outline.....	7
1.5. Conclusion.....	9
II A NEW CONSIDERATION IN THE DESIGN OPTIMIZATION OF SUBMERSIBLE ELECTRIC MOTORS.....	11
2.1. Introduction.....	11
2.2. Conventional Analytical Design of a PMSM.....	14
2.2.1. Parameterization of the Geometry.....	14
2.2.2. Calculation of the Flux.....	15
2.2.3. Calculation of the Necessary Torque and Current.....	18
2.2.4. Calculation of the Copper Losses.....	18
2.2.5. Calculation of the Iron Losses.....	20
2.2.6. Design Constraints.....	20
2.2.7. Sample Outputs.....	21
2.3. Analytical Design of a PMSM Including the Effects of Viscous Drag Losses.....	23
2.3.1. Motivation for the Study.....	23
2.3.2. The Analytical Approach.....	23
2.3.3. Utilization of Computational Fluid Dynamics Simulation Tools.....	25
2.3.3.1. Effect of Stator Slots.....	27
2.3.3.2. Effect of Air Gap Width.....	27
2.3.3.3. Effect of Temperature.....	29
2.3.3.4. Effect of Machine Geometry.....	30
2.3.3.5. Machine Design Procedure Considering Viscous Power Losses.....	31
2.4. Conclusion.....	33

CHAPTER	Page
III APPLICATION OF A DUAL VOLTAGE EXTERIOR ROTOR PM ACTUATOR IN COMPACT HARSH ENVIRONMENTS.....	35
3.1. Introduction.....	35
3.2. Application Considerations.....	36
3.3. Analysis and Testing of the Existing Actuator.....	39
3.4. Design and Testing of the Initial Improvement.....	42
3.5. A Dual Winding PM Actuator.....	48
3.5.1. Arrangement of the Machine’s Winding.....	48
3.5.2. Dynamic Model of the Machine.....	49
3.5.3. Rotor Reference Frame Equivalent Circuit Model.....	57
3.5.4. Experimental Results.....	61
3.6. Conclusion.....	64
IV APPLICATION CONSIDERATIONS IN HARSH ENVIRONMENT POWER ELECTRONIC ENERGY CONVERSION SYSTEMS.....	65
4.1. Introduction.....	66
4.2. Power Device Selection and Testing.....	66
4.2.1. Description of the Qualification Tests.....	67
4.2.2. System Impact of Si vs SiC.....	71
4.2.2.1. Silicon Carbide Technology and Impacts.....	71
4.2.2.2. Switching Device Test Results – SiC Case.....	72
4.2.2.3. Switching Device Test Results – Si Case.....	77
4.2.2.4. Diode Test Results.....	81
4.2.3. Basic Switching Unit.....	83
4.2.3.1. The Mosfet’s Performance in the Basic Switching Unit.....	85
4.2.3.2. Addressing the Challenges and Failure Mode.....	93
4.2.3.2.1. Failure Mode Equivalent Circuits.....	97
4.2.3.2.2. Passive Mitigation of the Failure Mode.....	100
4.3. Design and Testing of a Custom High Temperature Power Module.....	103
4.3.1. Simulation Results.....	104
4.3.2. Experimental Results.....	106
4.4. Conclusion.....	108
V MULTILEVEL POWER CONVERTERS – AN ENABLING TECHNOLOGY FOR HARSH ENVIRONMENT POWER CONVERSION.....	110
5.1. Introduction.....	110
5.2. Multilevel Power Conversion Solutions for Compact Harsh Environments.....	112

CHAPTER	Page
5.2.1. Topology Selection for a Compact Harsh Environment PMSM Drive.....	115
5.2.2. Algebraic SVPWM.....	117
5.3. Limitations of a Compact Harsh Environment Implementation.....	122
5.4. Experimental Results.....	125
5.5. Conclusion.....	127
 VI EXTENDED TEMPERATURE HIGH RELIABILITY MOTOR DRIVE SYSTEMS FOR HARSH ENVIRONMENT APPLICATIONS.....	 129
6.1. Introduction.....	129
6.2. Prior Art.....	129
6.3. Summary of the Principle.....	131
6.4. Detailed Description of the Principle.....	132
6.5. Commutator Design Considerations.....	139
6.6. Soft Commutation.....	143
6.7. Brush Assembly.....	145
6.8. Magnetic Coupling.....	146
6.9. System Progress and Experimental Results.....	149
6.10. Conclusion and Recommendations.....	151
 VII CONCLUSIONS AND FUTURE WORK.....	 153
7.1. Dissertation Conclusions.....	153
7.2. Recommendations for Future Work.....	156
 REFERENCES.....	 158
 APPENDIX A.....	 162
 VITA.....	 165

## LIST OF FIGURES

	Page
Fig. 1.1. Typical offshore oil rig.....	2
Fig. 1.2. Offshore field of multilateral and horizontal wells.....	3
Fig. 1.3. Prototype wireline open hole tractor tool .....	3
Fig. 2.1. The sequence of the calculations.....	12
Fig. 2.2. Machine design parameters.....	15
Fig. 2.3. Comparison of 6 pole 15 slot designs with different lamination.....	22
Fig. 2.4. Comparison of 8 pole 21 slot designs with different lamination.....	22
Fig. 2.5. Theoretical effect of oil shear loss.....	24
Fig. 2.6. Simple geometry of the problem.....	25
Fig. 2.7. Comparison of the analytical and CFD viscous loss calculations for an 8” long stack at two different temperatures.....	27
Fig. 2.8. Effect of the stator slots on the viscous power loss at 200°C.....	28
Fig. 2.9. Effect of the air gap width on the viscous power loss at 200°C.....	29
Fig. 2.10. Effect of temperature on the viscous power loss at 200°C.....	29
Fig. 2.11. Effect of machine geometry on viscous power loss at two temperatures...	31
Fig. 2.12. Simulation results of Motor 1 in air and in oil for different air gaps.....	32
Fig. 2.13. Iterative machine design including the effect of viscous losses.....	33
Fig. 3.1. Basic layout of a rotary steerable drilling tool.....	37
Fig. 3.2. Original layout of the dual voltage actuator with the generator winding (left) and electromagnetic brake winding.....	37
Fig. 3.3. Actuator lamination design.....	39

	Page
Fig. 3.4. Brake winding back emf vs rotor position at 2000 rpm.....	40
Fig. 3.5. Brake winding torque vs rotor position at 2000 rpm from an analytical model of the machine.....	41
Fig. 3.6. Brake winding torque vs rotor position at 2000 rpm using FE analysis....	41
Fig. 3.7. Brake winding flux plot using FE analysis.....	41
Fig. 3.8. Brake winding experimental results for different short circuit duty cycles.....	42
Fig. 3.9. Effect of manufacturing on the brake winding demonstrated through the testing of five prototypes.....	42
Fig. 3.10. Winding factors of the improved brake winding.....	43
Fig. 3.11. Effect of skew on the tooth flux density (red) skew = 0 slots, (blue) skew=1 slot.....	44
Fig. 3.12. Effect of skew = 0 on the machine's back emf at 2000 rpm.....	45
Fig. 3.13. Effect of skew on the machine's torque (red) skew = 1 slot, and (blue) skew = 0 slot at 2000 rpm.....	45
Fig. 3.14. FE analysis of the effect of skew = 0 slots on the machine's back emf at 2000 rpm.....	46
Fig. 3.15. FE analysis showing the effect of skew = 0 on the brake winding torque at 2000 rpm.....	46
Fig. 3.16. Prototype of brake winding with skew = 0.....	46
Fig. 3.17. Experimental results of improved brake winding torque at various short circuit duty cycles.....	46
Fig. 3.18. Winding arrangement schematic of a dual winding PM actuator with an arbitrary angle, $\zeta$ , between the two windings.....	49
Fig. 3.19. Effect of phase displacement angle, $\xi$ , on the mutual coupling between the dc and brake windings.....	53
Fig. 3.20. Simulation model of a dual winding PM actuator.....	55

	Page
Fig. 3.21. Brake winding terminal voltages and generator winding rectified voltage (red) for 0 % braking.....	55
Fig. 3.22. Brake winding terminal voltage (blue, green) and generator winding rectified voltage for 95 % braking.....	56
Fig. 3.23. d-q equivalent circuit model of the dual winding machine.....	58
Fig. 3.24. Phasor diagram for normal operating conditions.....	59
Fig. 3.25. Phasor diagram for operation with shorted terminals.....	59
Fig. 3.26. Prototype dual winding stator.....	62
Fig. 3.27. Brake winding current (10 A/div) .....	63
Fig. 3.28. Braking winding torque at various braking duty cycles.....	63
Fig. 3.29. Dc output voltage at various brake winding duty cycles over the speed range.....	63
Fig. 4.1. Static $R_{dson}$ setup.....	68
Fig. 4.2. Dynamic $R_{dson}$ measurement setup (a) and principle (b).....	69
Fig. 4.3. Diode $V_f$ drop experimental setup.....	70
Fig. 4.4. $V_{ceon}$ for different $V_{ge}$ at various temperatures for the IGBT.....	70
Fig. 4.5. SiC 1500 V Cascode Power Mosfet Static $R_{dson}$ at 650 V/ 1A versus temperature.....	72
Fig. 4.6. SiC 1500 V Cascode Power Mosfet Static $R_{dson}$ at 650 V/ 1A versus time.....	73
Fig. 4.7. SiC 1500 V Cascode Power Mosfet Dynamic $R_{dson}$ 650 V/1A vs temperature.....	74
Fig. 4.8. SiC 1500 V Cascode Power Mosfet Dynamic $R_{dson}$ 650 V/1A vs time...	74
Fig. 4.9. SiC 1500 V Cascode Power Mosfet Body Diode $V_f$ vs temperature.....	75

	Page
Fig. 4.10. SiC 1500 V Cascode Power Mosfet Leakage Current vs. temperature at 650 V.....	76
Fig. 4.11. 1500 V Cascode Power Mosfet Leakage Current vs. time at 230°C.....	77
Fig. 4.12. Static leakage current test on the best performing IGBT versus temperature.....	78
Fig. 4.13. Static leakage current test on the best performing Mosfet versus temperature.....	79
Fig. 4.14. Static leakage vs accrued time at 210°C for different $V_{gs}$ .....	80
Fig. 4.15. Static $R_{dson}$ vs accrued time at different temperatures.....	81
Fig. 4.16. Leakage current experimental results of the best performing schottky device.....	81
Fig. 4.17. Leakage current of the SiC diode at full voltage versus temperature.....	82
Fig. 4.18. SiC diode forward characteristics.....	82
Fig. 4.19. Experimental results demonstrating the SiC diode paralleling considerations.....	83
Fig. 4.20. Basic Mosfet and diode switching unit for the motor drive application....	84
Fig. 4.21. Schematic of the experimental and simulation setups used in the Mosfet loss analysis.....	85
Fig. 4.22. Experimental results with FETs alone.....	87
Fig. 4.23. Simulation results with FETs alone.....	88
Fig. 4.24. Experimental results with the blocking and parallel diodes.....	89
Fig. 4.25. Simulation results with the blocking and parallel diodes.....	89
Fig. 4.26. Experimental results with the blocking diode across a capacitor and the parallel diode.....	90
Fig. 4.27. Simulation results with the blocking diode across a capacitor and the parallel diode.....	90

	Page
Fig. 4.28. Experimental results with an inductive turn on snubber.....	91
Fig. 4.29. Simulation results with an inductive turn on snubber.....	91
Fig. 4.30. Experimental results with diodes but at a higher voltage.....	92
Fig. 4.31. Simulation results with diodes but at a higher voltage.....	92
Fig. 4.32. Experimental results of switch $V_{gs}$ (black) and blocking diode voltage (red).....	94
Fig. 4.33. Simulation results of switch $V_{gs}$ (black) and blocking diode voltage (red).....	94
Fig. 4.34. Current flow in bottom fet (green) top fet (blue) top parallel diode (red).....	96
Fig. 4.35. Power loss in antiparallel blocking diode.....	96
Fig. 4.36. Simplified equivalent circuit of failure mode.....	97
Fig. 4.37. I(leg) (blue) and leg voltage with low (brown) and high values (red) for the diode capacitance.....	98
Fig. 4.38. More realistic equivalent circuit of failure mode.....	99
Fig. 4.39. I(leg) (green), I (diode) (blue), FET Voltage (light blue – small cap, red – big cap), leg voltage (light brown).....	100
Fig. 4.40. Simulation results of switch $V_{gs}$ (green) and blocking diode voltage (red) with external capacitor.....	101
Fig. 4.41. Current flow in bottom fet (green) top fet (blue) top parallel diode (red).....	102
Fig. 4.42. Power loss in the blocking diode without the parallel capacitor (red) with it (green).....	102
Fig. 4.43. Thermal simulation results for full multilevel inverter phase leg in one leg (left) and half (right).....	105
Fig. 4.44. Theoretical and experimental module losses at various values of current.....	106

	Page
Fig. 4.45. Thermal image and the corresponding module used for the test.....	107
Fig. 4.46. Experimental setup used for mechanical (left) and burn in tests (right)...	107
Fig. 5.1. Typical setup of a well logging application.....	110
Fig. 5.2. Simplified distribution system model.....	111
Fig. 5.3. Simplified schematic of the prototype multilevel dc-dc converter.....	113
Fig. 5.4. Experimental and simulation results of a prototype NPC multilevel dc-dc converter.....	113
Fig. 5.5. Experimental results at no load (a) and load (b) showing the effect of not using middle point voltage balancing.....	114
Fig. 5.6. Switching patterns for different voltage levels for the flying capacitor inverter (a) and NPC (b).....	116
Fig. 5.7. Simplified schematic of the three phase flying capacitor multilevel inverter prototype.....	117
Fig. 5.8. Voltage space vectors of a three level inverter.....	118
Fig. 5.9. Inverter switching states (P, A, B, N) and the relevant capacitor current control paths.....	119
Fig. 5.10. Simulation results of the SVPWM showing phase A flying capacitor voltage $V_{dc} = 1kV$ .....	122
Fig. 5.11. Basic switching unit (left) simulation results of the blocking diode overvoltage problem (right).....	123
Fig. 5.12. Experimental results showing the effect of temperature on high voltage ceramic capacitors.....	124
Fig. 5.13. Performance of the prototype inverter under sudden load changes, load current (top) and device and bus voltage (bottom).....	125
Fig. 5.14. Motor drive efficiency vs temperature.....	126
Fig. 5.15. Layout showing a tool with two multilevel inverters; each black heat sink is for one phase leg.....	127

	Page
Fig. 6.1. Simplistic view of a brushed dc motor.....	133
Fig. 6.2. Principle of operation of brushed dc motors.....	133
Fig. 6.3. Production of alternating current in an R-L circuit.....	134
Fig. 6.4. Current flow in a 3 phase brushless dc motor winding.....	135
Fig. 6.5. Conventional electronic commutation using an inverter.....	136
Fig. 6.6. Apparatus used for motor commutation.....	137
Fig. 6.7. Final assembly including commutation apparatus.....	138
Fig. 6.8. Thought process used .....	138
Fig. 6.9. Short-circuited winding element in dc machine commutation.....	139
Fig. 6.10. Illustration of the different types of commutation.....	141
Fig. 6.11. First commutator prototype (left) latest prototype (right).....	142
Fig. 6.12. Mitigation of the arcing using a freewheeling diode.....	143
Fig. 6.13. Current commutation in the proposed system.....	143
Fig. 6.14. Basic principle of soft commutation.....	144
Fig. 6.15. First brush holder prototype (left) latest prototype (right).....	146
Fig. 6.16. Initial magnetic coupling concept, test results (left) and test setup (right).....	147
Fig. 6.17. Schematic illustration of the proposed system.....	148
Fig. 6.18. Components of the magnet coupling of the second prototype.....	148
Fig. 6.19. Stages of the development.....	149
Fig. 6.20. First prototype of the commutator installed on the torque side of the motor.....	150
Fig. 6.21. Line current (left) and voltage (right) waveforms.....	150

Fig. 6.22. Second prototype of the commutator installed on the resolver side of  
the motor.....151

**LIST OF TABLES**

	Page
Table 2.1. Machine design parameters.....	14
Table 2.2. Comparison of theoretical and experimental results on the effect of oil shear losses.....	24
Table 4.1. Waveforms legend for all figures of this section.....	86
Table 4.2. Main range of materials used in the module construction with some thermal properties.....	103

# CHAPTER I

## INTRODUCTION

### 1.1 Introduction

Well logging, the automotive industry, nuclear power, industrial processing plants and space exploration are just a few examples of applications that are highly dependent on the existence of compact harsh environment energy conversion systems. State of the art power components are limited to a maximum operating temperature of 150°C. There is significant research effort today focusing on dielectric and insulating materials and the development and characterization of high-temperature components. This dissertation will take this effort a step forward by approaching the topic from a system point of view. Compact harsh environment energy conversion systems will be the main focus of the work.

The unique needs of the well logging industry place stringent demands on the power conversion systems. The quest for energy is leading the industry into drilling deeper wells. Typically, a temperature gradient of 1°C/150 ft can be expected, with bottom hole temperatures reaching beyond 200°C in many areas of the world today. With the current prices of energy, running a rig similar to that shown in Fig. 1.1 can easily fall in the six digit zone. This has placed even more stringent needs on the energy conversion systems used in such environments. Moreover, the increased recovery benefits and cost reductions possible with the use of horizontal and multilateral wells has triggered a need for higher power energy conversion systems in bottom hole assemblies.

---

This dissertation follows the style of *IEEE Transactions on Industry Applications*.

Electrical machine technologies are now very common in today's industry. Early market entries relied mainly on hydraulic energy conversion systems, but the latest power electronic systems have demonstrated superior performance and reliability. The concepts developed throughout this work were developed to address some of these new needs.



Fig. 1.1. Typical offshore oil rig.

A typical arrangement of horizontals and multilaterals is shown in Fig. 1.2. It is evident here that a means of drilling such wells and conveying logging tools in such wells would be needed. An illustration of a down hole tractor tool still underdevelopment is shown in Fig. 1.3. Such a tool provides very demanding traction requirements on the motor drive system which is magnified by the compact nature and the harsh environment of the application. It is also evident that power delivery to the downhole tools will also have its effect on the electrical performance of the system. These issues will be addressed in this dissertation in detail along with other aspects.

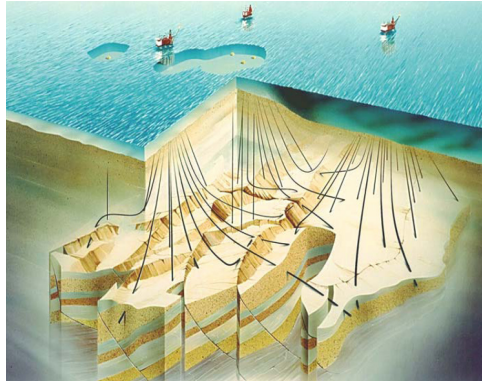


Fig. 1.2. Offshore field of multilateral and horizontal wells.

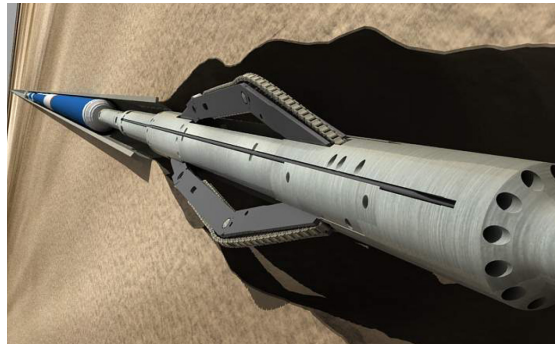


Fig. 1.3. Prototype wireline open hole tractor tool.

## **1.2 Components of a Compact Harsh Environment Energy Conversion System**

### **1.2.1 Electromechanical Subsystem**

Motors, generators and brakes are generally referred to in this dissertation as being a part of the electromechanical subsystem. The design optimization of these components needs to be closely tied to a good understanding of the operating conditions that they will be exposed to. Without such an understanding, designs optimized for operation under normal ambient operating conditions, will suffer in the compact harsh environments addressed by this dissertation. This will be clearly demonstrated in several chapters of the dissertation.

The design and optimization of electric machines will be addressed using methods common to machine designers and readily reported in literature. It will then be shown that such methods will produce results that are not optimal in nature and that environmental conditions need to be taken into consideration for a successful implementation.

The proper choice of machine topology will also be seen as a major contributor to the improved performance of electromechanical systems in compact harsh environments. Such machine topology options may not be apparent at first as suitable candidates to the solution, but an understanding of the environment and how it affects the machine topology did prove to be of great benefit.

It will also be shown that the specific nature of compact harsh environments may give rise to means of electromechanical energy conversion that would be completely irrelevant to conventional surface applications. However, their use in compact harsh environments can bring massive benefits on both the operational and business sides.

Although an understanding of the insulation systems and material properties as they apply to the design of electromechanical devices for compact harsh environments was crucial to the successful implementation of such systems, it is not the main focus of the dissertation. Whereas the main focus of the dissertation as it relates to the electromechanical subsystem is to devise novel means of machine design analysis and optimization, to assess the feasibility of novel applications of machine topologies, and to introduce novel driving and control mechanisms for electrical machines suitable for operation in such environments.

### **1.2.2 Power Electronics Subsystem**

The power electronics subsystem is another crucial component of the harsh environment energy conversion system. Both DC/DC and DC/AC converters were part of the current research. Introducing novel converter topologies was not the objective of the dissertation, however, the application aspects and novel solutions to the limitations of current converter topologies was the main objective here. The harsh environmental conditions and limited space available for the electronic components make the design of a reliable power electronics subsystem a challenge. The limited temperature capability of commercial power devices and the difficult and sometimes impossible integration of proper cooling means are only two of the challenges. Power electronic device manufactures are currently focusing their efforts on solving what the automotive industry is addressing, which is, electronic modules for 125°C operation. What is required by the high tier oil well logging and drilling market is an order of magnitude more, and operation between 175°C and 200°C can be seen as common.

In order to deal with such requirements, comprehensive qualification and testing is carried out. A portion of the dissertation will be dedicated to demonstrating the procedures and techniques used in qualifying devices for elevated temperature operation. The limitations faced are then outlined and equivalent circuit modeling of the major issues and the proposed solutions will be provided. Because the requirements of the new bottom hole assemblies are orders of magnitude different in power than previous work presented in literature and carried out in industry, there was a need to design a custom power module. The logic behind the design process and the tradeoffs are linked to the environmental conditions faced by the assembly.

Building upon the results of device qualification and custom power module construction, a look at the system from a different perspective is needed. It is shown that the power delivery method will have a large impact on the topologies of choice in the power electronics subsystem. This is dictated by the nature of the application and how it is affected by the presence of long resistive cables between the surface supply system architecture and the bottom hole assemblies. The conflicting nature between the compact packaging requirements, complex topologies, and thermal considerations are then demonstrated and the research provides a successful account of dealing with such constraints.

### **1.3 Objective of the Research**

The objective of this work is to present novel solutions to many of the challenges faced in the development of compact harsh environment energy conversion systems. Today's systems have been limited in their power capability and thus performance. This is due to the absence of suitable switching devices, the migration of conventional design techniques to the downhole industry without significant consideration of the new environment, inheritance of previous designs, and a concentration on the improvement of conventional methods instead of devising methods that would benefit from the operating environment.

The specific goals of the present research are to alleviate the limitations of the existing compact harsh environment energy conversion systems by providing:

- A comprehensive study of the effect of the operating environment on the electrical machines used in bottom hole assemblies and the development of a

new electrical machine design procedure that considers these environmental aspects.

- Design optimization of an external rotor permanent magnet actuator, and the development of a dual three phase winding permanent magnet machine that utilizes the coupling between the two sets of windings to the application's advantage.
- An investigation of the application limitations of power semiconductor devices in compact harsh environments. The mitigation of failure modes of the switching unit using a simple novel application consideration that is verified using simplified equivalent circuits and experimentally.
- A study of the effect of power delivery to bottom hole tools on the feasible topologies for harsh environment high power applications, and the successful implementation of the proposed solution.
- Combine the understanding of the limitations of the electromechanical energy conversion subsystem and the power electronic subsystem into an appreciation of what novel ideas can bring to the table. This is demonstrated through the development of a novel motor drive solution that offers the advantages of extended temperature operation, compactness, low cost, and high reliability.

#### **1.4 Dissertation Outline**

A brief introduction and overview of the dissertation have been provided in the preceding sections. The work should be viewed as a comprehensive study of the needs of energy conversion systems in compact harsh environments. To that end, each chapter

will tackle a specific aspect and present recommendations and novel solutions to the aspect at hand.

In chapter II, the migration of conventional design techniques to the downhole industry without significant consideration of the new environment is addressed as it pertains to the design of electrical machines. The specific case of the three phase permanent magnet synchronous machine is used, however, the study is applicable to any machine topology. The chapter introduces the problems associated with the operation of high speed motors submersed in a viscous fluid. A new loss component that is found to have a significant effect on the machine design is studied in detail and a design procedure to help take that loss component into consideration is proposed.

Chapter III demonstrates how the application considerations and the nature of the connected load are a main consideration in a successful design of a dual voltage exterior rotor PM actuator. The physical coupling between the two sets of windings was used in favor of the application. Although such a machine topology is common in large machines typical of generating stations and rail road cars, it was found to be the ideal candidate for the system at hand.

Chapter IV begins with an investigation into the power electronic subsystem of the energy conversion chain. A demonstration of the rigorous work needed to design high temperature power conversion systems is presented. A novel simple mitigation technique to the main failure mode exhibited during the development and its explanation using simplified equivalent circuits is provided. Finally, a custom high temperature power module is designed and successful prototype testing and comparison with simulation results is provided.

Chapter V builds on the testing and qualification results presented in chapter IV. However, it takes this a step further by investigating the effects that the nature of the application has on the topology selection. Multilevel power conversion is found to be the ideal candidate for high power down hole energy conversion systems. The successful implementation of the three level flying capacitor multilevel inverter is demonstrated. The advantages of using a Mosfet multilevel inverter due to limitations on capacitor technology are then shown.

Chapter VI demonstrates the advantages of novel ideas and the benefits that may bring to the design of compact harsh environment energy conversion systems. A novel three phase brushless PM motor drive system that has little or no electronics is presented. The advantages this brings in terms of reduced cost, high reliability, extended temperature operation, lower wire count, and lower product development cost are illustrated.

Chapter VII presents a review of the main ideas presented in the work. It also provides recommendations for future work in the different subsystems presented in throughout this research.

## **1.5 Conclusion**

Finally, it is safe to say that the research proposed as the subject of this dissertation will provide an essential contribution to current research in the field of compact harsh environment energy conversion systems. A comprehensive study of the previous literature presented in the area has been thoroughly carried out. The significance of the research in solving current practical industry needs has been stressed. A need for future

research in this area can highly benefit from the recommendations and conclusions made in this work. The work can be seen as divided into three main areas:

1. Electromechanical subsystems
2. Power electronic subsystems
3. A novel energy conversion system development that combines the understanding of the first two subsystems and an appreciation of the operating environment.

## CHAPTER II

### A NEW CONSIDERATION IN THE DESIGN OPTIMIZATION OF SUBMERSIBLE ELECTRIC MOTORS

#### 2.1 Introduction

PM synchronous servo motors are in widespread industrial use today, performing as the main drive system in highly demanding applications such as welding, machine tending, material handling, grinding, submersible pumps and conveyance tools. A drive cycle can characterize the demands on a servo motor in an industrial application. The drive cycle usually consists of an acceleration, a part with constant speed, and a retardation and standstill portion. The drive cycle usually has a low intermittence, i.e. the motor has to supply high torque during the cycle, but only during a small fraction of the total cycle time. The losses are large when the motor is producing high torque, but as they are produced under a fraction of a drive cycle, the average losses will be lower. The thermal time constant of a motor is much longer than the cycle time of a drive cycle. By sizing the motor considering the thermal demands instead of the peak torque during the cycle, a smaller and less expensive motor can accomplish the desired task.

The inertia of the motor is very important in all servo drives, as during the acceleration, the motor not only has to supply torque to accelerate the load, but also has to supply torque to accelerate itself. What is important is the ratio between the motor inertia and the load inertia. If the motor inertia is negligible compared to the load inertia, the benefit of reducing the motor inertia is small, as most of the motor torque anyway is used to accelerate the load. On the other hand, if the motor and load inertia

are of comparable sizes, reducing the motor inertia gives the benefit of less torque requirement for the same acceleration.

When optimizing an electric machine, there are different criteria of the optimum to choose from, for example minimum weight, minimum cost, maximum torque etc. For every criteria of optimum there must be a set of constraints like minimum permissible torque, maximum allowable volume etc. Here, the criterion of the optimum has been chosen to be the minimization of the losses of a machine capable of performing a specific task. The total loss is the objective function of the optimization along with the demands of the drive cycle, together with some geometric conditions as constraints.

A procedure has been written that calculates the performance of the machine. Input to the routine is a vector with variables describing the geometry of the machine. The output of the procedure is the value of the objective function, total losses in this case, and the values of the set constraints. The design optimization procedure is based on non-linear constrained optimization using sequential quadratic programming. There are upper and lower bounds on the optimization variables. The material properties are constants for every program run.

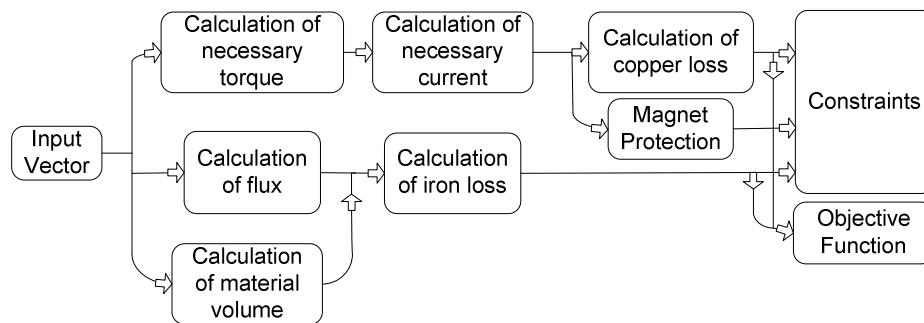


Fig. 2.1. The sequence of the calculations.

As the optimization strategy is to minimize the losses of a machine capable of giving a desired torque during a drive cycle, the calculations of the performance of a specific design has to start with calculation of the necessary torque given the drive system specifications. Figure 2.1 shows the sequence of the calculations and their dependence. The calculations are have been derived from available literature [1].

The conventional approach to machine design optimization has been described above. Its use is not seen as a contribution to the current state of the art, but is a necessary introduction to what will be presented in this chapter. The main objective of this chapter is to address how the migration of conventional design techniques to the downhole industry without significant consideration of the new environment will not produce an optimal design. This is demonstrated through the example of electrical machine design optimization. The specific case of the three phase permanent magnet synchronous machine is used, however, the study is applicable to any machine topology. The chapter introduces the problems associated with the operation of high speed motors submersed in a viscous fluid. A new loss component that is found to have a significant effect on the machine design is studied in detail and a design procedure to help take that loss component into consideration is proposed. Thus, the chapter is divided into two main sections. The first will present the conventional method of machine design optimization and the application of that on a three phase PMSM. The second section demonstrates the ineffectiveness of blindly using the same technique without considering the additional loss component due to the presence of the viscous loss in the air gap. The chapter concludes with a proposed design procedure that builds upon the

conventional design methods, and expands that to the optimal design of electrical machines submersed in a viscous fluid.

## 2.2 Conventional Analytical Design of a PMSM

### 2.2.1 Parameterization of the Geometry

Parameterization of the geometry of Fig. 2.2 as shown in Table 2.1 was first performed. The rest of the dimensions can be derived from those used in the parameterization. Because of the application's space constraint, the machine's diameter was kept constant. Several assumptions will be made in the design procedure and when possible, will be verified using finite element analysis.

Table 2.1. Machine design parameters.

Parameter Number	Symbol	Description
1	$l_{ge}$	effective gap length
2	$r_{my}$	External rotor radius
3	$l_{stack}$	Stack length
4	$l_m$	Height of magnet
5	$h_{tw}$	Height of tooth wedge
6	$w_t$	Width of tooth
7	$h_t$	Height of tooth
8	$d_c$	Depth of stator core
9	$w_s$	Width of slot

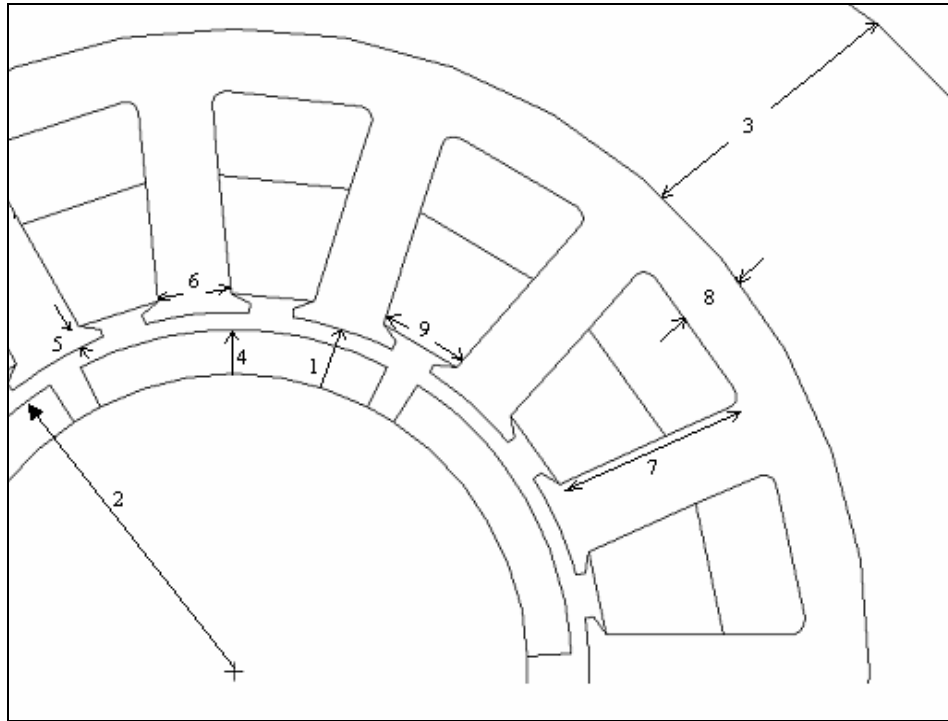


Fig. 2.2. Machine design parameters.

### 2.2.2 Calculation of the Flux

When calculating the flux, there is always a tradeoff between model complexity and computing time. The classical way of dealing with the nonlinear permeability of the iron is to assume that the iron is infinitely permeable and that all the MMF is consumed in the airgap. To avoid that the optimization yields a design with infinitely small tooth and stator yoke, a maximum flux density in the iron is introduced as a constraint. The maximum flux density is the choice of the designer. This is the kind of model used to formulate the design software. Due to the fact that an accurate finite element (FE) design package will use the obtained results in order to fine tune them, it was found adequate to use such an approach. A more complex model is the Magnetic Equivalent Circuit (MEC). The model consists of an arbitrary number of nonlinear and linear reluctances, and accuracy, complexity, and computing time are determined by the

number of elements. In the model at hand, it is also easy to change the pole and slot numbers. This can aid in determining the optimal tradeoff between rotor yoke thickness (flux density) and inertia for various designs. The flux density in the magnets is assumed to be uniform.

The equations used to define the analytical model of the machine, are ones presented in previous literature [1]. A myriad of approximations and assumptions have been incorporated in them in order to simplify the model. However, as previously stated, they do give a good quick general guide to the designer. The average flux density in the air gap is calculated from (2.1) as follows:

$$B_{go} = \frac{l_m}{l_{ge}} B_r \quad (2.1)$$

where,

$l_m$  is the magnet height ,

$l_{ge}$  is the effective gap width,

$B_r$  is the magnet residual flux density.

The maximum flux density in the stator tooth above a magnet is calculated from (2.2) as follows:

$$\hat{B}_t = B_{go} \frac{(w_s + w_t)}{w_t} \quad (2.2)$$

where,

$w_s$  is the slot width

$w_t$  is the tooth width.

If each magnet spans an angle of  $2\alpha$ , the root mean square value of the fundamental sinusoidal space component of the airgap flux density as derived from a Fourier series is given by (2.3)

$$B_{1g} = \frac{2\sqrt{2}}{\pi} B_{go} \sin(\alpha), \quad (2.3)$$

with a maximum value given by (2.4)

$$\hat{B}_{1g} = \sqrt{2} B_{1g}. \quad (2.4)$$

As mentioned earlier, the flux in the stator yoke should be calculated using an iterative technique based on theory from the machine's magnetic equivalent circuit. However our current implementation uses (2.4) and (2.5) to provide an approximate value of this physical quantity based on [2].

$$\phi_c(90^\circ) = \frac{2}{p} l_{stack} r_{si} B_{go}, \quad (2.5)$$

$$B_{core}(90^\circ) = \frac{\phi_c(90^\circ)}{d_c k_i l_{stack}}. \quad (2.6)$$

where,

- $r_{si}$  is the stator inner radius
- $l_{stack}$  is the active length of the machine
- $d_c$  is the depth of the stator core
- $k_i$  is a factor depending on the iron material used
- $\phi_c$  is the core flux.

### 2.2.3 Calculation of the Necessary Torque and Current

The calculation of the necessary torque has a lot of safety, thermal and compensation factors, which of course could all be included into one. It is beneficial though to have control over what compensates what and to what degree, and that is best done by adding a factor for each requirement. The torque calculation can easily be extended for a more complicated drive cycle, with for example a number of different torque levels during the acceleration (and braking) cycle. Torque linearity is not considered in the model and no measures are taken to assure that the assumption of no armature reaction is violated. This will be checked in the future work using FEM. The required torque and peak ampere turns are calculated from (2.7) and (2.8)

$$T = \pi r_{my}^2 l_{stack} \hat{A} B_{1g} \quad (2.7)$$

$$N\hat{I} = \hat{A} \frac{3}{\pi} \frac{r_{si}}{pk_w} \quad (2.8)$$

where, torque is basically expressed as the product of the electrical and mechanical loading of the machine multiplied by the rotor volume, and (2.8) gives the relation between the peak ampere turns and the motor's electrical loading. Where,

$r_{my}$  is the rotor outer radius

$\hat{A}$  is a representative of the machine's electric loading

$N\hat{I}$  is the machine's peak ampere turns

$p$  is the machine's number of poles.

### 2.2.4 Calculation of the Copper Losses

The copper length of half a coil is shown in (2.9) where,  $l_{ec}$  is the length of the end turns. The current density in the copper is calculated from (2.10)

$$\frac{l_{coil}}{2} = l_{stack} + l_{ec} , \quad (2.9)$$

$$j_{cu} = \frac{NI_{slot\_RMS}}{A_{slot}k_{fill}} , \quad (2.10)$$

where,

$NI_{slot\_RMS}$  is the rms ampere turns

$A_{slot}$  is the slot area

$k_{fill}$  is the copper fill factor.

An approximate formula for the calculation of the slot area is shown in (2.11)

$$A_{slot} = \frac{\pi(r_{so}^2 - (r_{si} + h_{tw})^2) - Q(w_t h_t) - \pi(r_{so}^2 - (r_{so} - d_c)^2)}{Q} \quad (2.11)$$

where,

$Q$  is the number of slots

$r_{so}$  is the stator outer radius

$r_{si}$  is the stator inner radius.

The copper volume is then given by (2.12) and the total copper loss by (2.13).

$$V_{cu} = A_{slot}k_{fill} \frac{l_{coil}}{2} Q \quad (2.12)$$

$$P_{cu} = \rho_{cu} j_{cu}^2 V_{cu} . \quad (2.13)$$

where,

$\rho_{cu}$  is the resistivity of copper in  $\Omega m$

$j_{cu}$  is the current density in  $A/m^2$ .

### 2.2.5 Calculation of the Iron Losses

The machine's iron loss is calculated from (2.14). The coefficients  $k_h$  and  $k_e$  are the classical eddy and hysteresis loss coefficients which can be calculated at various frequencies and flux densities from curve fitting of manufacturer data sheets. The obtained design's maximum flux density is used in the equation to calculate the loss. This is accomplished by calculating the weight of the iron in the machine from (2.15) and (2.16) and finding the total loss of the machine from the obtained per unit weight loss curves. The details of the calculation are given in the Appendix.

$$P_{fe} = k_h B_{\max}^2 f + k_e (B_{\max} f)^2, \quad (2.14)$$

$$\begin{aligned} A_{lam} &= A_{yoke} + A_{teeth} + A_{teeth\_wedges} \\ &= \pi(r_{so}^2 - (r_{so} - d_c)^2) + Q(w_t h_t) + Q(w_t h_{tw}) \end{aligned} \quad (2.15)$$

$$W_{lam} = \rho_{iron} V_{iron}. \quad (2.16)$$

### 2.2.6 Design Constraints

The constraints are the relations that must not be violated. Examples of geometrical constraints are:

- The rotor outer radius plus the airgap must not be larger than the stator inner radius
- The magnet angle times the number of poles must not be larger than  $2\pi$
- The airgap should be set between certain limits in order to prevent unrealistic results
- The maximum allowable flux densities in the various machine parts should be taken into consideration, depending on the material being used

- The number of slots and teeth multiplied by the slot and tooth pitches should equal  $2\pi$ .

Other constraints are the demagnetization and thermal constraints previously touched upon. As previously stated such constraints were not adequately represented in the current model. It should be noted that, the addition of such constraints is highly dependant on experimental results in order to corroborate the theory.

The materials that were investigated were Hiperco 50, M – 19 (0.025”), and M – 19 (0.01”) thick. Manufacturer data sheets were obtained in order to model the material losses at various flux densities and frequencies of excitation. Hiperco 50 is a high grade expensive material usually used for high performance applications ranging from submersible equipment to space exploration vehicles. M –19 steels, are a more common silicon steel, well known to the motor manufacturing industry, highly applicable for medium performance applications. The allowable operating flux density of Hiperco is higher than that of M-19, in the optimization it was set to 1.6 T, and 1.2 T for M-19. These settings can be varied and are currently dependant on the designer’s choice.

### **2.2.7 Sample Outputs**

This section provides some sample results obtained from the machine optimization routine. Two different pole/slot combinations and three different lamination materials were investigated. The algorithm was run at various load points for every lamination material. Thus, three different machines were designed for every lamination material. This quick means of comparison between machine properties at various load points enables a designer to pursue further optimization only for the most promising design.

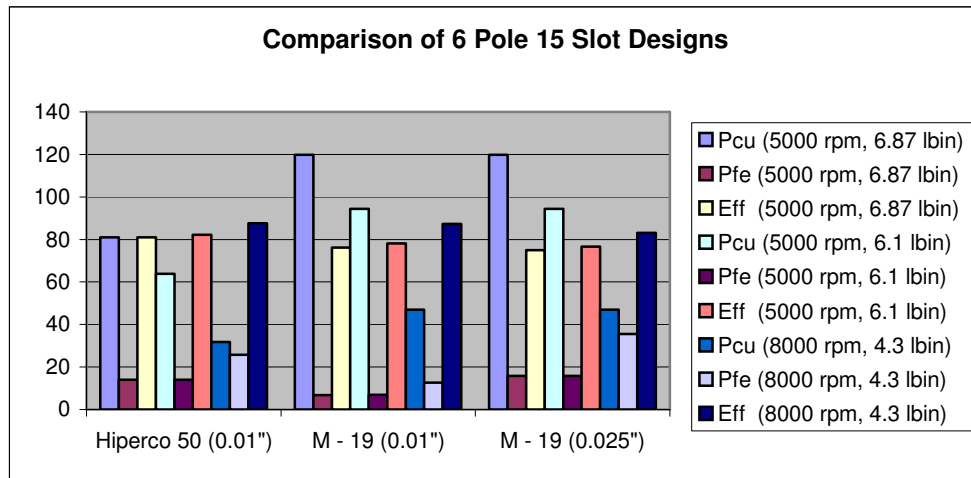


Fig. 2.3. Comparison of 6 pole 15 slot designs with different lamination.

The application of the design procedure on a six pole machine is shown in Fig. 2.3 and the application to an 8 pole 21 slot design is shown in Fig. 2.4. These two sets of data are for a machine with the same diameter and length. It is clear from a study of the two sets of results that the six pole machine is a more suitable candidate for the application at hand since the efficiency for all the designs exceeds that of the eight pole design for every load condition and for the three different lamination material choices.

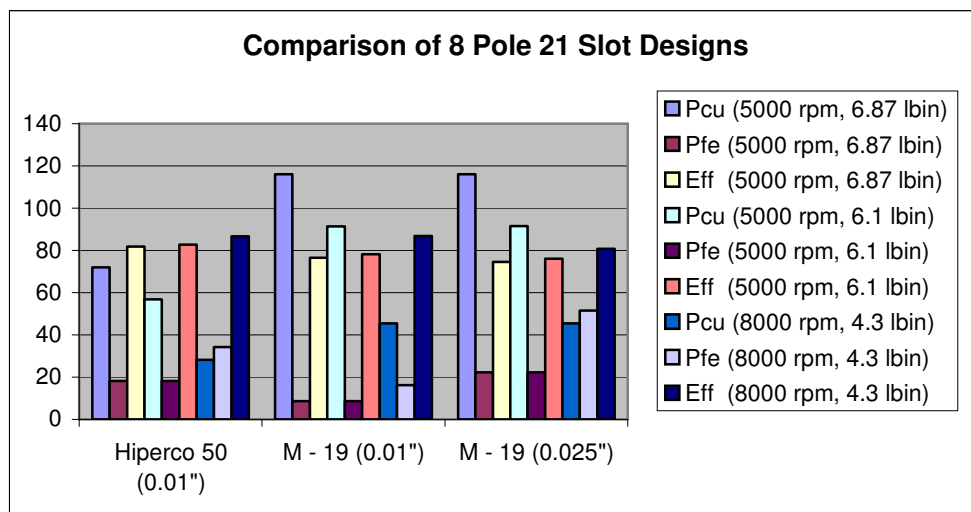


Fig. 2.4. Comparison of 8 pole 21 slot designs with different lamination

## **2.3 Analytical Design of a PMSM Including the Effects of Viscous Drag Losses**

### **2.3.1 Motivation for the Study**

Due to the nature of oil well logging and drilling applications, the tool pieces are usually submersed in oil in order to prevent the tool from overheating by acting as a medium of conduction for the heat to the external surface of the tool and to prevent the build up of any air bubbles and the collapse of the tool under the high pressures found in the wells. Lubrication of the gearbox and bearings is another use of this oil. Testing of the prototype motor while submerged in oil, however, didn't truly comply with the simulations or with the testing in air. The prototype motor was rated for 400 W of output power at 10000 rpm, however, its efficiency at the same load point was reduced significantly when submerged in oil. This prompted an investigation into the effect of oil in the motor's air gap on the machine's losses. Thus, besides the presence of a myriad of electromagnetic aspects when a novel motor design is put in question, there comes the added effect of oil shear or viscous losses.

### **2.3.2 The Analytical Approach**

A review of fluid dynamics theory [3][4], indicated that this type of loss can be calculated and is found to be dependant on the airgap thickness, temperature, and in turn the fluid viscosity and other geometric factors. Table 2.2 shows a comparison between the theoretical laminar flow calculations and experimental results. It can be seen that the theoretical results are indeed quite low indicating a high degree of turbulent fluid losses. Please note that the results were obtained at a temperature of 40 deg C measured with a thermocouple glued to the end turns of the winding.

Table 2.2. Comparison of theoretical and experimental results on the effect of oil shear losses.

Speed (rpm)	Theoretical (W)	Experimental Rough (W)	Experimental Smooth (W)
1000	0.54	4.5	4
5000	13.6	16	10
7500	30.5	58	27

Fig. 2.5 shows a plot of the analytically calculated power loss due to oil shear effect at various temperatures. This was calculated using (2.17), where,  $\rho$  is the specific gravity,  $\nu$  is the fluid viscosity at the ambient temperature,  $d$  is the rotor outer diameter,  $N$  is the rotor speed,  $L$  is the stack length, and  $c$  is the air gap length. It is apparent that this loss is highest at lower temperatures due to the high viscosity of the oil, however, as previously stated, the theoretical values provide very low values when compared with the experimental ones. Thus, it was seen that further study of this phenomenon is needed in order to better understand the difference between the analytical and experimental results.

$$P_v = \rho \nu \pi^3 d^3 N^2 L / c 10^{15} \quad (2.17)$$

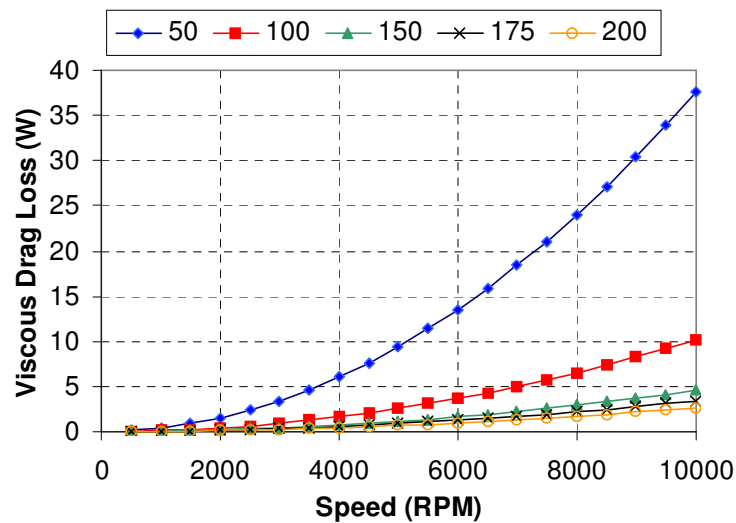


Fig. 2.5. Theoretical effect of oil shear loss.

### 2.3.3 Utilization of Computational Fluid Dynamics Simulation Tools

This discussion presented in this section was triggered by the results reached in the previous section involving the analytical calculation of the fluid viscous or friction loss. The aim of this section is the calculation of the frictional losses occurring due to the lubricating oil in the air gap between the stator and the rotor in an electrical motor. The impacts of the operating temperature and the gap thickness on the power losses are studied. Comparisons between the analytical and numerical solutions are also made. Two different motor geometries are used in the study. The first geometry M1 has a rotor diameter that is 0.6422 times larger than the second geometry M2.

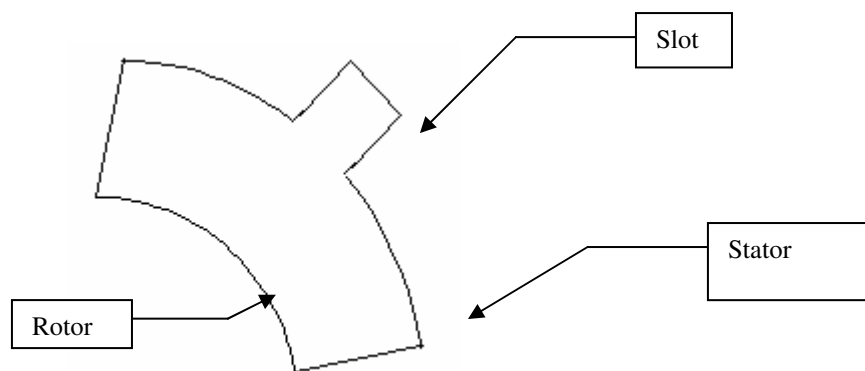


Fig. 2.6. Simple geometry of the problem.

The problem involves the simplified geometry of Fig. 2.6. Lubricating oil is present in between the stator and the rotor. The oil, due to its viscosity presents a resistance to the motion of the rotor. The goal is to estimate the power losses due to this resistance.

The transition Reynolds number for the oil filling the gap was calculated from (2.18) as 18,413 [3]

$$\frac{\Omega R^2 \rho}{\mu} = \frac{41.3}{(1-k)^{1.5}} \quad (2.18)$$

where  $R$  is the transition Reynolds number,  $k$  is the ratio of the inner and outer diameters,  $\rho$  is the density and  $\mu$  is the dynamic viscosity of the fluid. The viscosity of the oil to be used in the application drops approximately 200 times as the temperature is increased from 20 °C to 200 °C. The Reynolds number of the flow at 200 °C is  $3.8 \times 10^6$ . This requires remarkable changes in the numerical modeling, as the flow is no longer laminar. The standard  $k$ - $\epsilon$  model is employed in Fluent to solve the turbulent flow with all other parameters remaining the same.

Since an analytical solution for the turbulent flow does not exist, we need to estimate the optimum grid size and the convergence criterion necessary for solving the flow. This is done by taking different grid sizes and comparing the results at various convergence criteria. Four different grids are taken into consideration. The base case of 0.0086 mm x 0.0086 mm is called 1 x 1. This size of 0.0086 mm was taken so that the first cell placed in the domain falls within a  $y^+$  range of 30 – 120 as required for the standard wall treatment. A grid size of 2 x 1 means that the grid has been refined two times in the  $x$ -direction with the  $y$ -interval remaining the same as 0.0086 mm. The simulation was carried out for the two concentric cylinders case. From this exercise, we can conclude that all the grids converge to give a shear stress between 60 Pa and 70 Pa. So it was concluded that the 1 x 1 grid was fine enough if a convergence criterion of  $10^{-6}$  is used. Therefore, this was the grid used in all the following turbulent study cases.

A comparison between the laminar flow results and CFD results is shown in Fig. 2.7 for the two concentric cylinders case. It is evident that as the flow becomes turbulent at

200°C, the difference between the two methods becomes apparent. Thus, the absence of an analytical approach to accurately model turbulence was the main motivation to the use of CFD [5],[6].

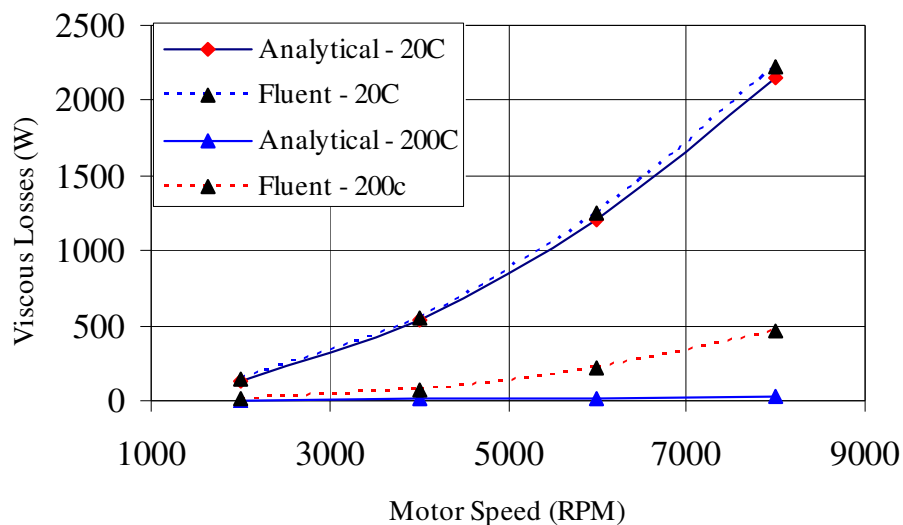


Fig. 2.7. Comparison of the analytical and CFD viscous loss calculations for an 8" long stack at two different temperatures.

### 2.3.3.1 Effect of Stator Slots

The effect of the slot width on the power loss is also studied. Fig. 2.8 shows the power losses for a gap width of 0.017 inch for simulation models with the slot and without the slot. The power loss increases by an average value of 14 % in the presence of the slot at the higher speeds. This can be explained by the presence of eddies in the slot, which results in increasing velocity gradients at the wall, which thereby increases the shear stress leading to an increased power loss.

### 2.3.3.2 Effect of Air Gap Width

The slotted model was solved for different air gap sizes. Gap thickness was varied by

changing the rotor radius keeping the stator radius fixed. Gap widths of 0.017, 0.02, 0.04, 0.06 and 0.08 inches were used. The power losses for the M1 motor for these gap widths are shown in Fig. 2.9. We can see that the power loss increases approximately 35 times as the speed increases from 2000 rpm to 8000 rpm for the same gap thickness. And the power loss drops by a factor of two as the gap width increases from 0.017 in to 0.08 in.

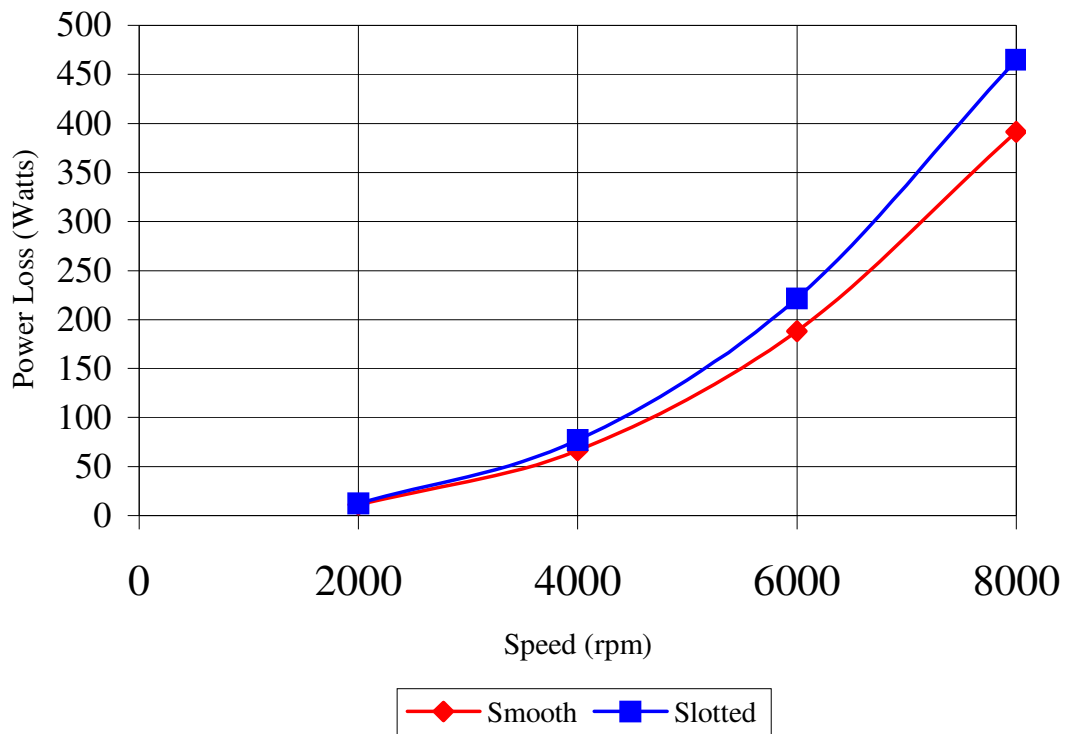


Fig. 2.8. Effect of the stator slots on the viscous power loss at 200°C.

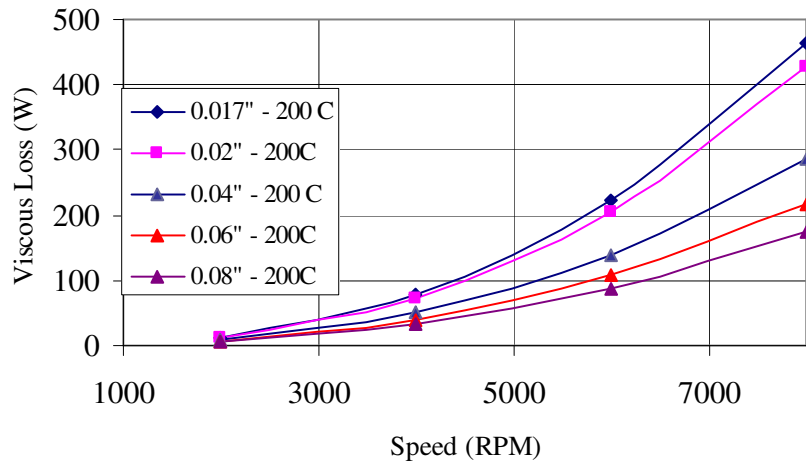


Fig. 2.9. Effect of the air gap width on the viscous power loss at 200°C.

### 2.3.3.3 Effect of Temperature

The effect of temperature on the power loss was also investigated. Even though the energy equation is not solved in the model, temperature comes into play in the fluid properties as mentioned earlier. The model was solved for a range of temperatures with an air gap width of 0.04 inch and the results are presented in Fig. 2.10.

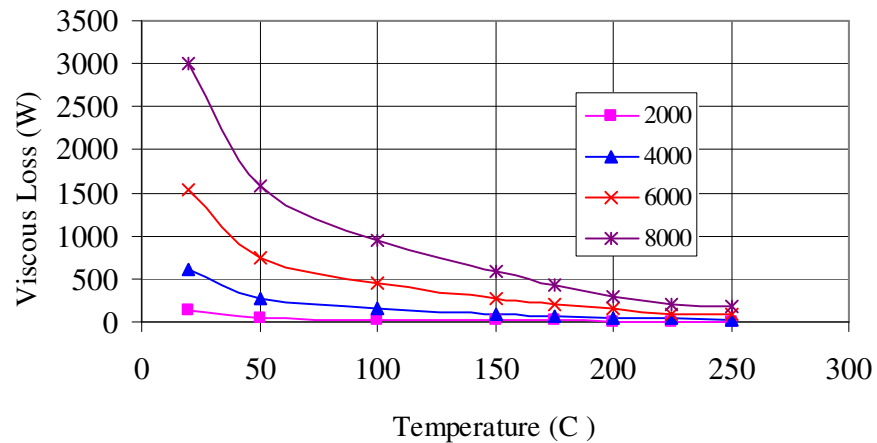


Fig. 2.10. Effect of temperature on the viscous power loss at 200°C.

### 2.3.3.4 Effect of Machine Geometry

The analysis of viscous loss in the previous subsections was done using one stator and rotor geometry. In order to assess the effect of the machine geometry on the viscous loss, a comparison with a different machine geometry was done. The new machine, called M2 (M1 will be used for the first geometry) has a rotor diameter that is 0.6422 times smaller than the M1 rotor. Fig. 2.11 shows the power losses for the two motors for an air gap width of 0.017". We can see that the highest power losses for the M2 model occurring at a temperature of 20 °C are still less than the M1 loss at 100 °C. The first and the most influencing parameter in this reduction of power loss is the rotor radius. Which is a parameter that conflicts with the torque production capability of the machine from an electromagnetic point of view. The rotor of the M2 motor is 0.6442 times smaller than that of the M1 model as mentioned above. And as we have seen earlier from (2.17), the power loss is proportional to the rotor diameter cubed. Although we mentioned that the analytical equations don't truly apply, they do however give a good indication of the proportionalities. This clearly explains the nearly 400 % ( $0.6442^3 = 0.2673$ ;  $1/0.2673 = 3.741$ ) reduction in the power losses in the M2 model as compared to the M1 model. Another factor in reducing the power losses is the number of slots. The number of slots was changed from 39 to 12 in the simulation model between M1 and M2. The effect of the stator slotting was seen in an earlier section to affect the value of viscous power loss by upto 14%. Hence all these effects combine to give less viscous power loss in the M2 model as compared to the M1 model.

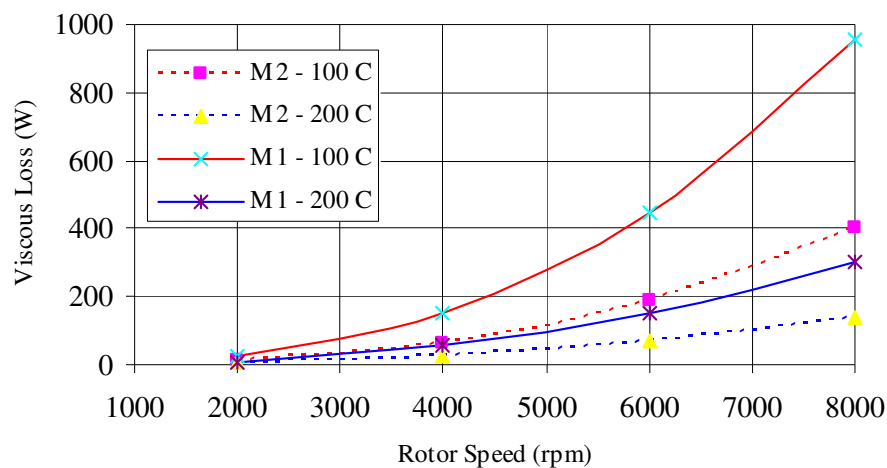


Fig. 2.11. Effect of machine geometry on viscous power loss at two temperatures.

### 2.3.3.5 Machine Design Procedure Considering Viscous Power Losses

In the previous sections, an attempt to familiarize the reader with a submersible machine's viscous losses was made. It is now clear that this loss component is conflicting in nature with the electromagnetic optimization of the machine in air, and that an accurate estimation of this loss component would require the use of CFD software. This section will present a design procedure that should be used in the design and optimization of motors submersed in viscous fluids. The efficiency plots of Fig. 2.12 will be used to support the formulation of the design procedure. Maintaining the same outside dimensions and load, two machines with two different air gaps (0.017' and 0.04') were optimized. Fig. 2.12 shows that a very minor difference, approximately 1-2%, is expected when the machines are running with no viscous fluid in the air gap. The CFD results of Fig. 2.9 were then included in the calculation of the machine performance, and demonstrate the expected drop in efficiency at higher speeds. The reduction in efficiency for the machine with a 0.04' air gap is, however, less than the

0.017' air gap machine. This is an expected outcome after assessing the results of the previous sections. A point will however be reached when the increase in the air gap will not provide a favorable solution to the machine design problem. This is due to the dominance of the electromagnetic losses when that point is reached. This leads us to the need for an iterative motor design procedure. A sample flow chart demonstrating what was concluded from the previous discussion is shown in Fig. 2.13. The machine optimization algorithm presented at the beginning of this chapter is only a step in the complete procedure. After the machine performance is calculated, including the effect of viscous losses obtained from CFD, the designer needs to check the efficiency at the higher speed range and follow the logic used to describe Fig. 2.12 until a suitable geometry is retained.

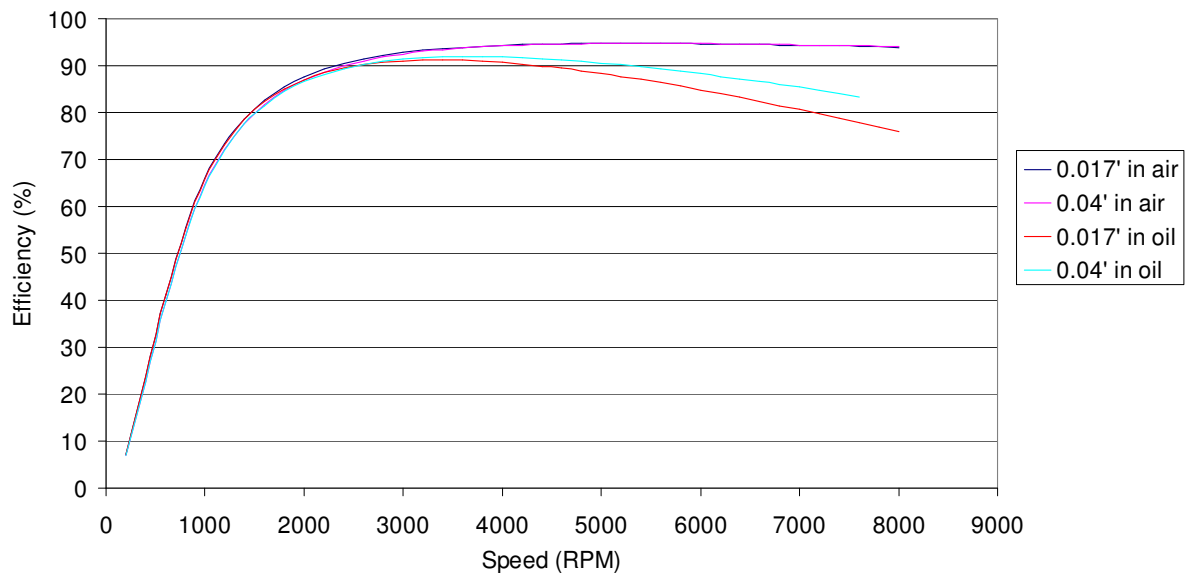


Fig. 2.12. Simulation results of Motor 1 in air and in oil for different air gaps.

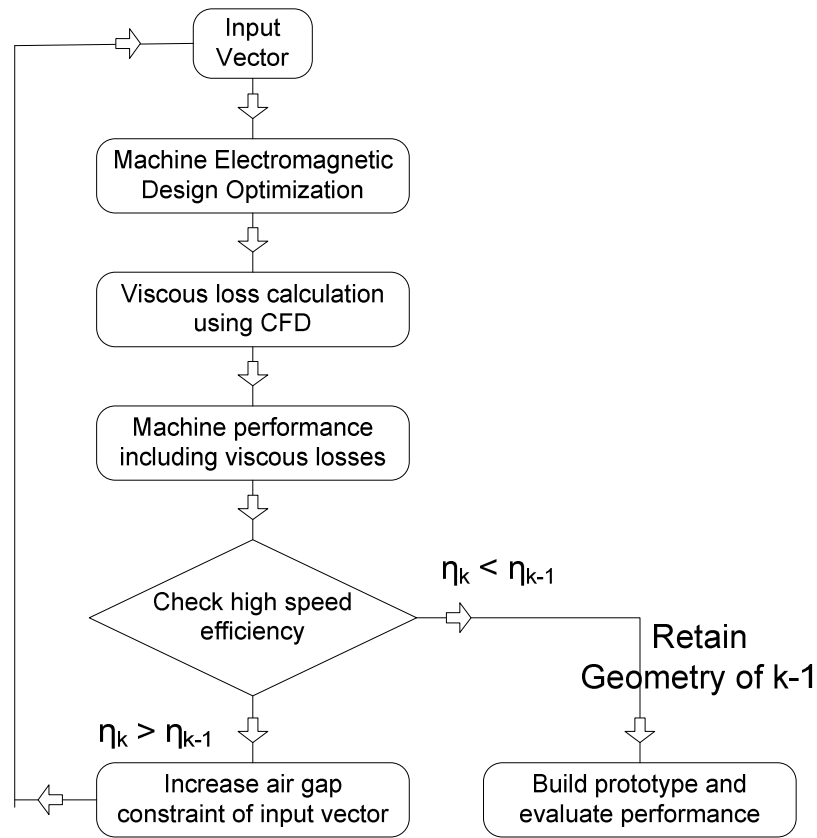


Fig. 2.13. Iterative machine design including the effect of viscous losses.

## 2.4 Conclusion

The influence of the operating environment plays an important role in the design of electrical machines. This fact was illustrated in the work at hand by investigating the design of a permanent magnet synchronous machine submersed in a viscous fluid. The work was prompted by a significant difference between an experimental setup tested in air and one tested in oil. After compiling the results of current literature into a machine design optimization algorithm, analytical and CFD analysis of the submersible machine was also presented. The need to use CFD for the estimation of the viscous loss component was demonstrated by the inadequacy of the analytical solutions in the presence of the turbulent flow properties of the fluid present in the air gap. Different

factors that affect the viscous loss component were analyzed in detail. An iterative machine design procedure is then presented as a complement to the conventional optimization methods. This can possibly trigger further research into coupled field analysis and optimization of electrical machines [7],[8].

## **CHAPTER III**

### **APPLICATION OF A DUAL VOLTAGE EXTERIOR ROTOR PM ACTUATOR IN COMPACT HARSH ENVIRONMENTS**

#### **3.1 Introduction**

Permanent magnet actuators are the natural electromechanical energy conversion choice for compact demanding applications. This is evident in their widespread use in automotive applications, engine-generator applications, aircraft applications, military applications, and oil well exploration applications. Their use in motoring, generation, and braking modes has been documented extensively in literature.

The environmental and loading conditions and their effect on permanent magnet machines have also seen a fair review in literature. It has been shown that application considerations and the nature of the connected load are a main input in the design of electrical machines for demanding applications. These factors were utilized in the design of a dual voltage exterior rotor permanent magnet (PM) actuator. The actuator is used in an oil well exploration application for a rotary steerable drilling tool. Dual voltage PM actuator applications, however, have seen wide application in other industries. The pending use of 42 V dc power for automotive and other vehicle electrical systems will require dual-voltage 42V/14V systems for the transition period [9]. In engine-generator applications, the output of a second winding can provide battery charging, field excitation, second load voltage ie. 480V/208V ac service. A 24 V rectified output dc power is in need in aircraft applications where the main winding is providing the 400 Hz, 208 V power. Compact dual voltage power supplies can also prove beneficial in military applications providing great flexibility especially in mobile

applications. The advantage of such an approach over the use of a dedicated dc/dc converter is the increased reliability of an electromechanical device.

The dual voltage PM actuator under investigation is used in a rotary steerable drilling tool Fig. 3.1 to help maintain the control electronics geostationary inside a rotating drill string. It also serves as the power source of the control electronics. The improvement of the existing actuator assembly was carried out on different phases. The different phases of the actuator improvement were concluded with the design of a dual winding PM actuator. The mutual coupling between the two sets of windings was used in favor of the application. Analytical and finite element (FE) analysis of the actuator and its various improvements will be presented in this work. A dynamic model of the dual winding exterior rotor PM actuator will also be developed. The advantage of utilizing the mutual coupling between the sets of windings for the application at hand will then build upon the understanding of the dynamic model. Experimental results corroborating the presented theory will demonstrate the effectiveness of the design.

### **3.2 Application Considerations**

The effectiveness of a certain machine design is highly dependant on the consideration of the end application. This proved to be especially true in the application at hand. The control electronics in Fig. 3.1 is shown supported with bearings on either side. This is typical of rotary steerable drilling tools used in oil well drilling. The reason for that is the need to keep this control unit geostationary with respect to the rotating drill string. If the unit is kept geostationary, it will enable the driller to control the direction of the bit and hence, the well profile. This is achieved by utilizing the on board accelerometers. This can provide huge returns and enable more efficient extraction of

the oil. Hence, the first function of the actuator at hand is to provide the braking torque required to keep the control electronics geostationary against the rotation of the string. The second function of the actuator at hand is to generate electrical power for the control unit.

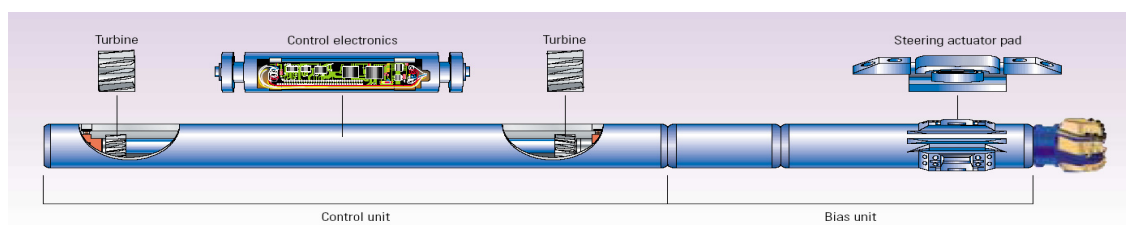


Fig. 3.1. Basic layout of a rotary steerable drilling tool.

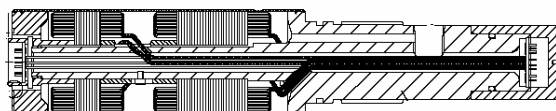


Fig. 3.2. Original layout of the dual voltage actuator with the generator winding (left) and electromagnetic brake winding (right).

It is now obvious that from the physical layout of the application, one would need to use an exterior rotor PM actuator. The terminals of the generator will thus be connected directly to the control unit without a need for brushes or slip rings.

The sequence of operation is such that initially, the control unit will rotate with the rotating drill string, and inertia, viscous air gap losses, and friction will be opposing this motion. This relative motion between the drill string that contains the PM rotor and the control unit will provide terminal voltage at the generator output. After a lower limit for this output voltage is exceeded, the control electronics is started and can control the

drive electronics that will provide the control logic to keep the unit geostationary. This is done by using the other winding as an electromagnetic brake. Thus, there exists a need to have the generator electrical constant as high as possible to enable low speed operation of the tool. The second winding is operated only as a brake, which is done by shorting its terminals with different duty cycles. Moreover, at the higher relative speeds and loads, the generator output voltage was seen to produce over voltage failures in the downhole power supply. While such problems may easily be resolved in a standard application, the nature of downhole applications requires significant derating of electronic modules due to the excessive temperatures experienced by the electronics. Thus, simply using a higher voltage rated device was not an option.

So, a need to “vary” the terminal voltage of the generator was needed at higher speeds and loads. Although achieving field weakening using complex electronics or control maybe a possibility, a simple and rugged means of achieving this goal was needed. This was done by using the mutual coupling in the dual winding machine in favor of the application at hand. This will be presented in detail in a later section. A need to increase the amount of braking torque delivered by the actuator was also addressed. This would provide the advantage of being able to achieve higher speeds under higher flow rates or loading conditions. These needs were to be achieved while maintaining the exact same assembly volume. The current assembly shown in Fig. 3.2 is composed of two separate machines. It should be noted here that only the stator (inner) winding is shown since the magnets are part of the tool body. The permanent magnet assembly will not be addressed with any design improvements in this work. Its length is equal to the combined length of the two PM actuators.

### 3.3 Analysis and Testing of the Existing Actuator

The current design was a legacy undocumented design that was treated as a black box. Thus, an analysis of the current design and testing was required to establish a basis for the improvement. The lamination design was traced as shown in Fig. 3.3 and used in the analytical and FE analysis.

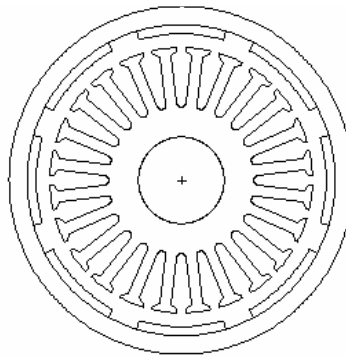


Fig. 3.3. Actuator lamination design.

The laminations of both windings, the generator and brake, are identical; however, they had different winding layouts and properties due to the difference in current carrying capacity and machine constants. One apparent point seen from Fig. 3.3 is the presence of a large air gap. This is very typical of submersible applications, and will be addressed in an ongoing work by the authors.

Both an analytical analysis of the machine based on [10] [11] and a FE analysis were carried out. It should be noted that the actual magnet housing is composed of segmented magnets as shown in the last figure of page 41. This was one of the reasons a FE approach was coupled to the analytical analysis. Such a magnet topology was easily modeled using FE software, whereas the development of an analytical model for this

architecture would have been needed. The back emf of the brake winding at 2000 rpm is shown in Fig. 3.4. This matched very well with the machine's terminal voltage constant of  $67 \text{ V}_{\text{pk}}/1000 \text{ rpm}$ . The corresponding machine torque is also shown in Fig. 3.5 using the analytical calculations and Fig. 3.6 using FE analysis. It should be noted that the differences between the analytical and FE results were not investigated in detail, since relative improvement and the effect of the mutual inductances are the main objectives of the work at hand. A flux density plot from the FE analysis is shown in Fig. 3.7.

Experimental results were then conducted to compare the mathematical analysis with the actual machine as shown in Fig. 3.8. A comparison of the analytical and FE results with Fig. 3.8 shows that a significant difference in the performance of the actual brake winding and the simulations exists. Five more prototypes were tested to aid the analysis and help provide insight into the difference in torque. The result of this testing, Fig. 3.9, does in fact show the significant effect of manufacturing on the machine's performance. Thus, the modeling was found to be sufficient for the work at hand.

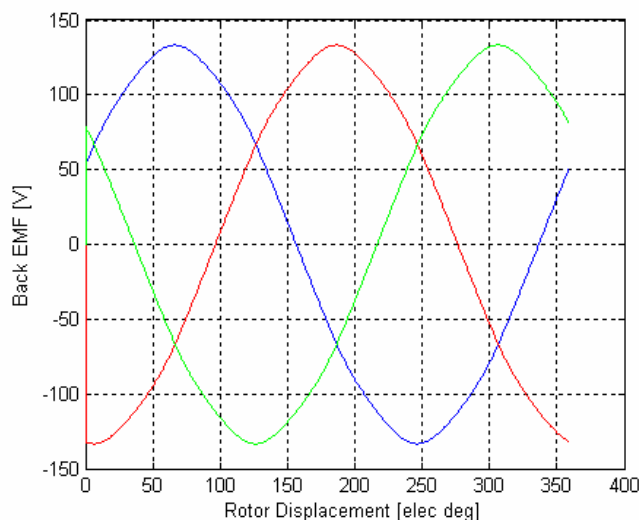


Fig. 3.4. Brake winding back emf vs rotor position at 2000 rpm.

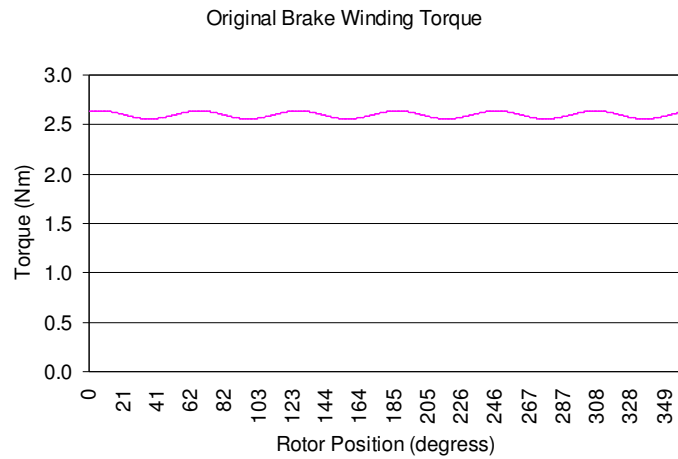


Fig. 3.5. Brake winding torque vs rotor position at 2000 rpm from an analytical model of the machine.

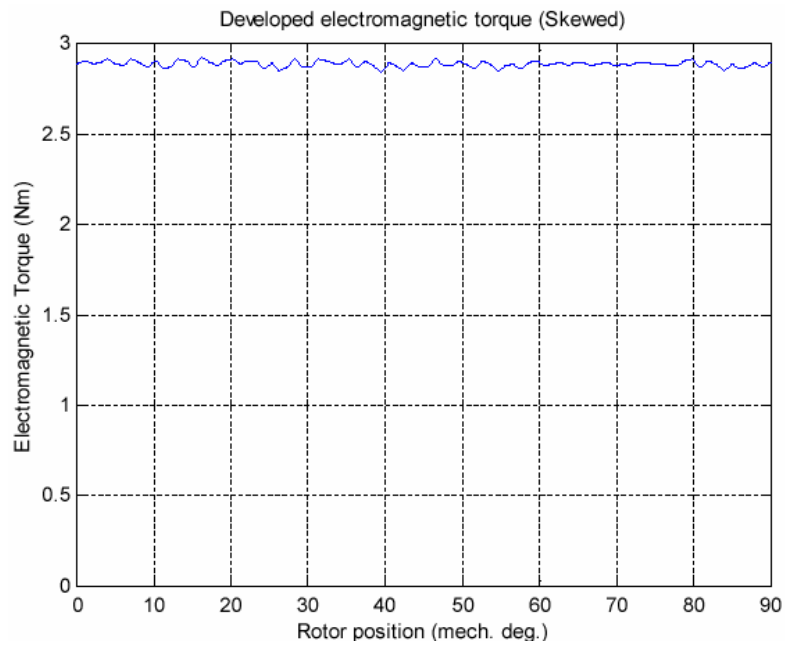


Fig. 3.6. Brake winding torque vs rotor position at 2000 rpm using FE analysis.

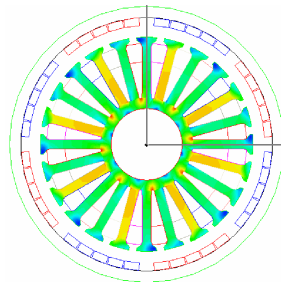


Fig. 3.7. Brake winding flux plot using FE analysis.

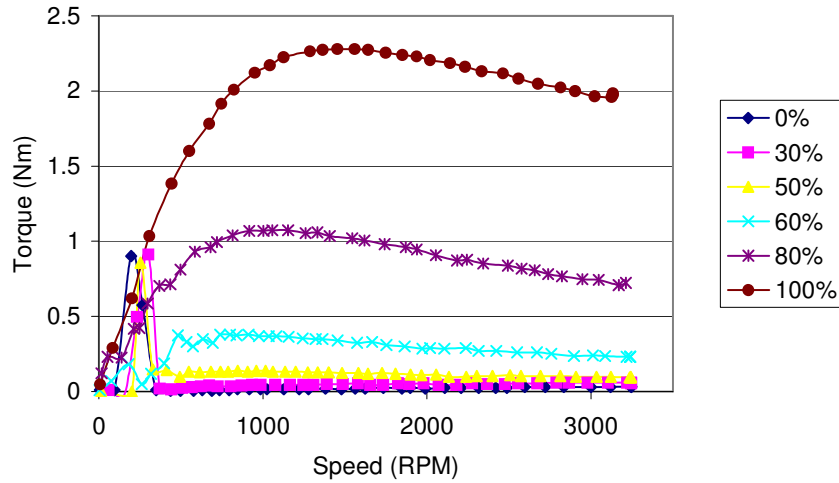


Fig. 3.8. Brake winding experimental results for different short circuit duty cycles.

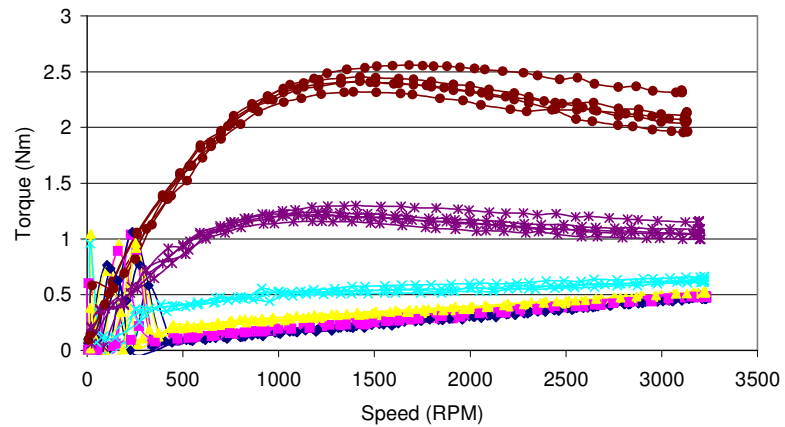


Fig. 3.9. Effect of manufacturing on the brake winding demonstrated through the testing of five prototypes.

A similar analysis was conducted on the generator winding, and both analysis and experimental results were compliant.

### 3.4 Design and Testing of the Initial Improvement

The initial improvement of the actuator will not take into consideration the need to “vary” the generator terminal voltage, but will concentrate on improving the brake

winding. This decision was driven by project needs, and was seen as an intermediate solution. Because the lamination was to remain fixed, finding a suitable winding layout was the first task. Winding factors were calculated for several configurations, and Fig. 3.10 shows the winding factors for the winding layout used.

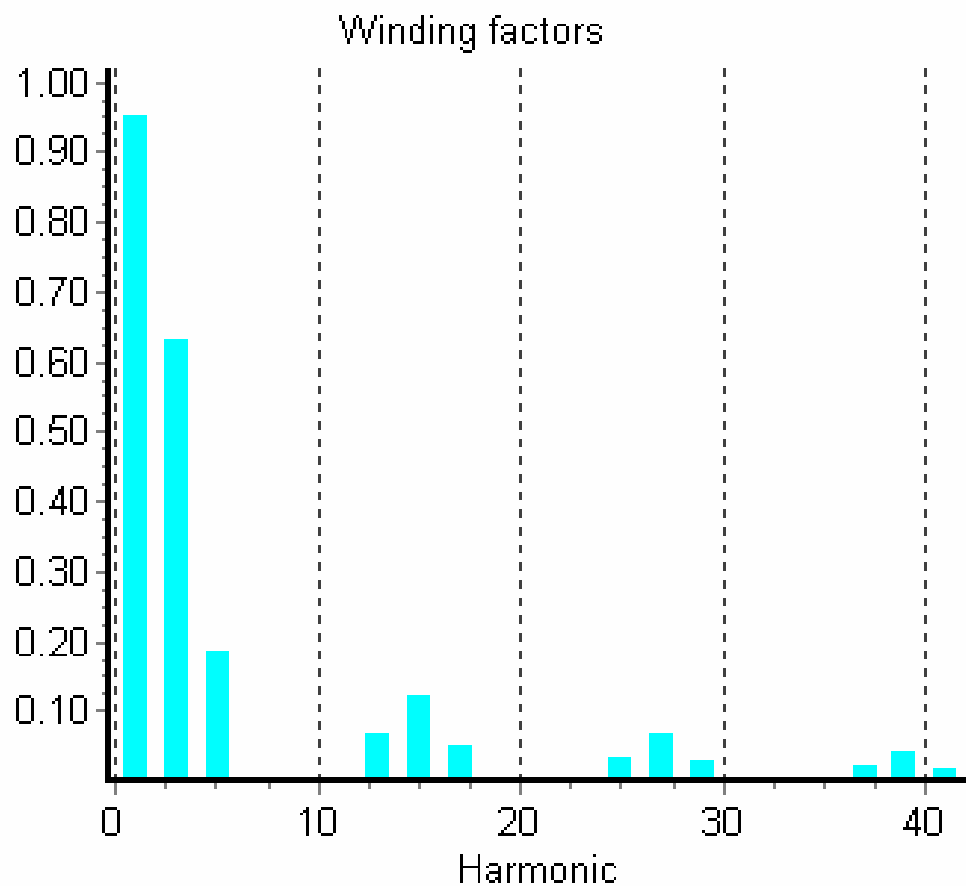


Fig. 3.10. Winding factors of the improved brake winding.

It is understood from the application needs that the machine is to operate in the presence of significant mechanical vibration, thus, torque pulsation is not a major concern. Unskewing the stator stack was investigated as a means of increasing the machine's torque. The effect of skew on several machine parameters will thus be

investigated using simulations. Fig. 3.11 shows the effect of a skew on the tooth flux density. It can be seen that unskewing the stator does flatten the top of the tooth flux density. Correspondingly, the effect of unskewing the winding on the machine's terminal voltage is shown in Fig. 3.12. The machine's torque was then calculated and plotted in Fig. 3.13. It is apparent from the calculations that unskewing the winding, will provide an increase in the braking torque capability of the machine. The corresponding FE analysis was carried out, and the back emf and torque waveforms are shown in Figs. 3.14 and 3.15. The increase in torque pulsation is can be seen from the analytical and FE results.

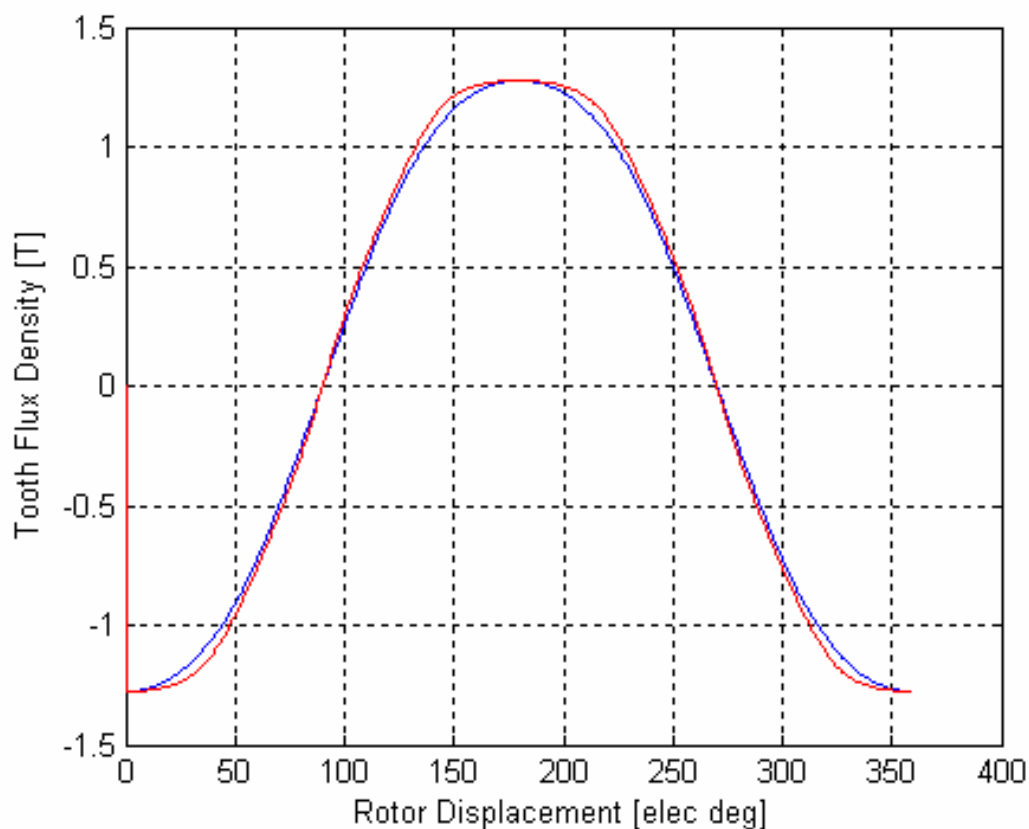


Fig. 3.11. Effect of skew on the tooth flux density (red) skew = 0 slots, (blue) skew = 1 slot.

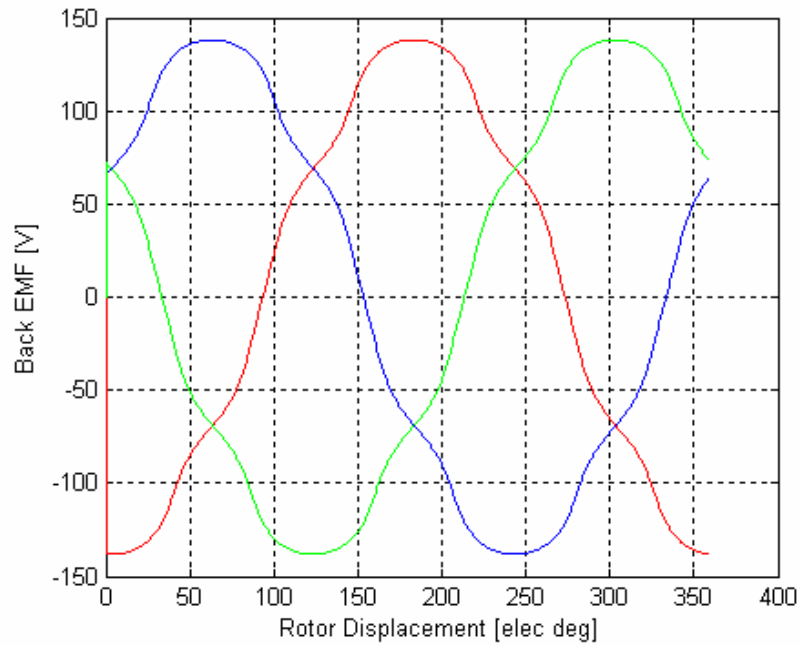


Fig. 3.12. Effect of skew = 0 on the machine's back emf at 2000 rpm.

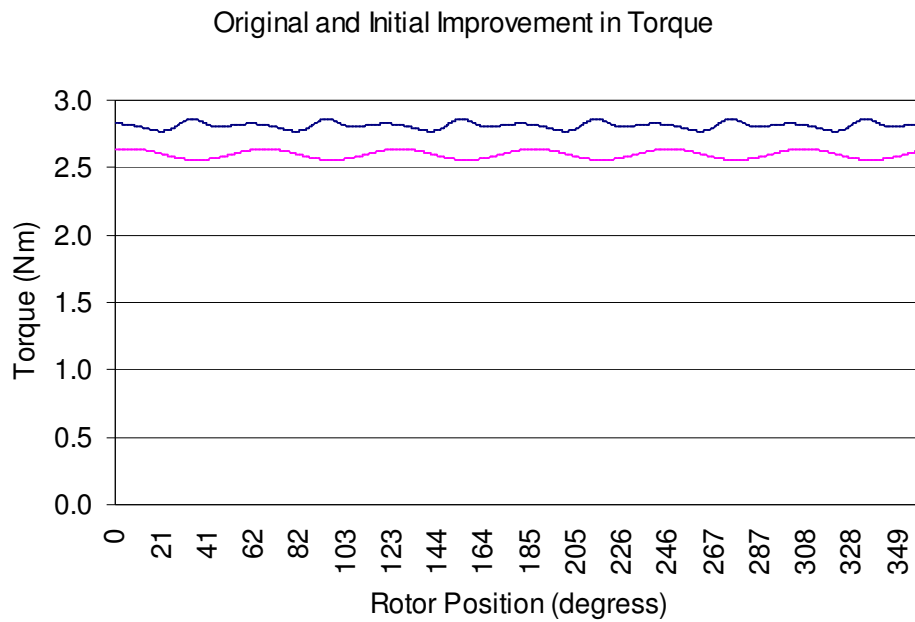


Fig. 3.13. Effect of skew on the machine's torque (red) skew = 1 slot, and (blue) skew = 0 slot at 2000 rpm.

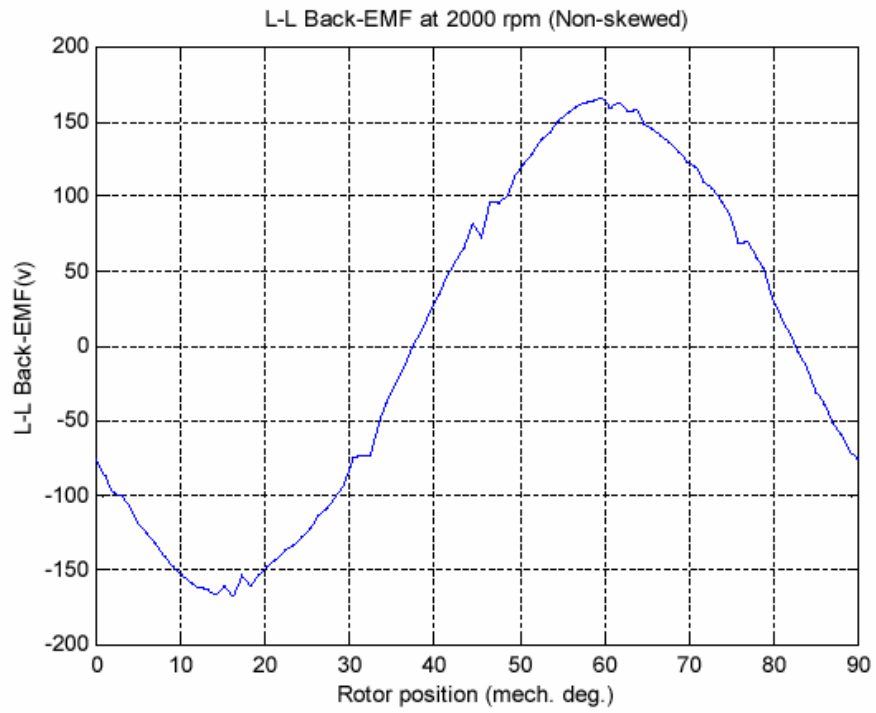


Fig. 3.14. FE analysis of the effect of skew = 0 slots on the machine's back emf at 2000 rpm.

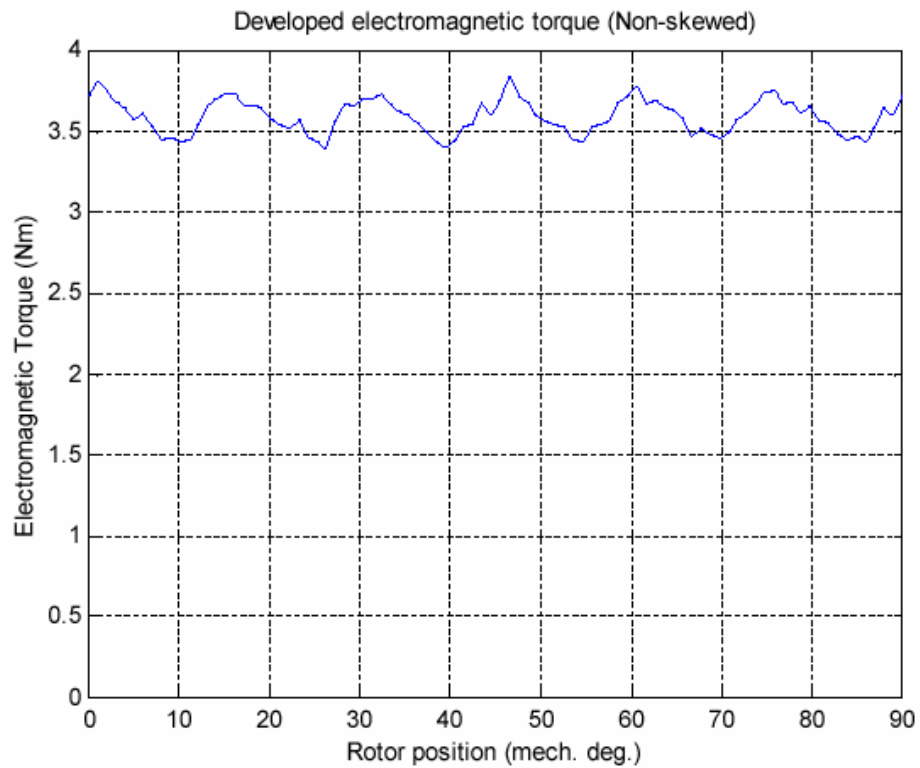


Fig. 3.15. FE analysis showing the effect of skew = 0 on the brake winding torque at 2000 rpm.

A prototype was then constructed to validate the modeling (Fig. 3.16) and experimental testing was conducted with the results shown in Fig. 3.17. Unlike the original brake winding, and increase in torque pulsation can be seen in Fig. 3.17. The relative increase in torque is in accordance with both the analytical and FE simulations.

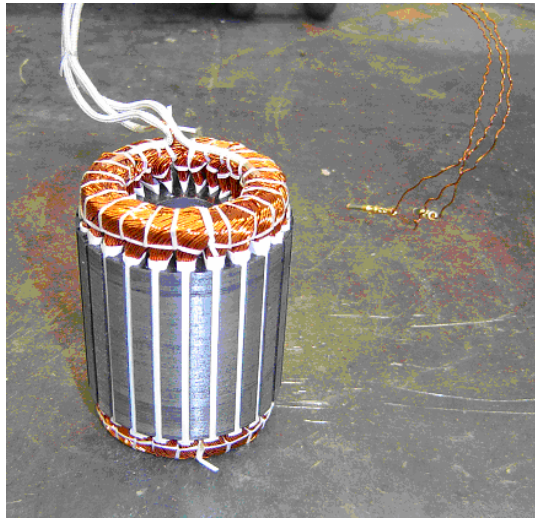


Fig. 3.16. Prototype of brake winding with skew = 0.

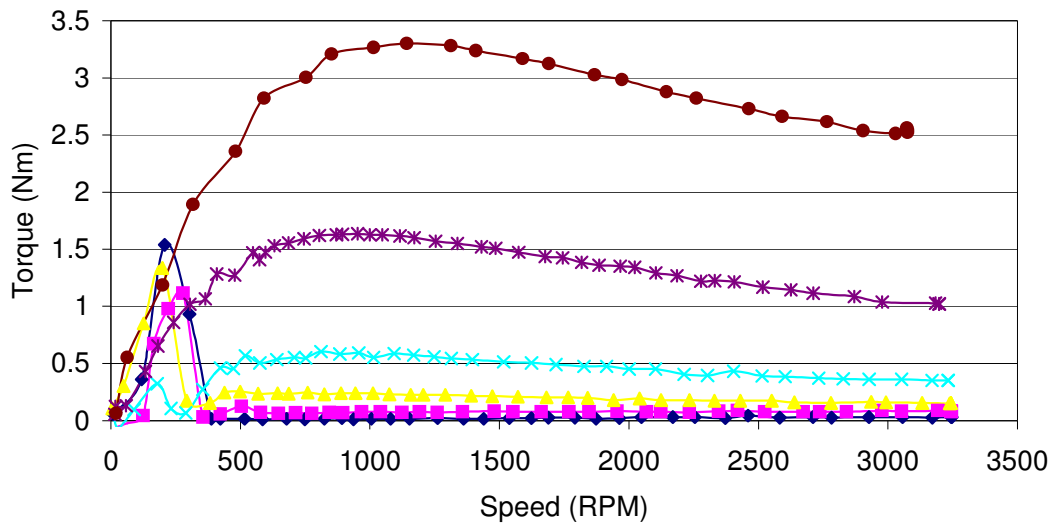


Fig. 3.17. Experimental results of improved brake winding torque at various short circuit duty cycles.

### 3.5 A Dual Winding PM Actuator

It was found that the optimal solution to the problem at hand may be solved using a dual winding PM machine. A look at Fig. 3.2 will help point this out. If one were to construct a single winding stack that can utilize the complete volume, it would have many advantages. The main advantage is the elimination of the two inner end windings of both machines. Because both machines have a relatively short stack, the end windings occupy a significant amount of space, which can be better utilized if a single stack is used. The use of a single stack will also reduce the component count, and installation time of the assembly. It will also improve reliability by providing a better means of wiring the assembly. Moreover, it can provide a simple means of “varying” or controlling the generator winding output voltage without the need for complex field weakening control systems or electronics. This will become evident in the discussions presented in this section.

#### 3.5.1 Arrangement of the Machine’s Windings

The arrangement of the two stator windings and permanent magnet field (represented here as a field winding) is shown schematically in Fig. 3.18. The three phase system ABC is displaced with respect to the abc system by  $\zeta$  electrical degrees [12]. The machine inductances will be presented in terms of  $\zeta$  whenever that is applicable to investigate the influence of this displacement angle on the performance of the PM actuator. To simplify the analysis, the effect of saturation is neglected and the two windings are assumed to have an equal number of turns.

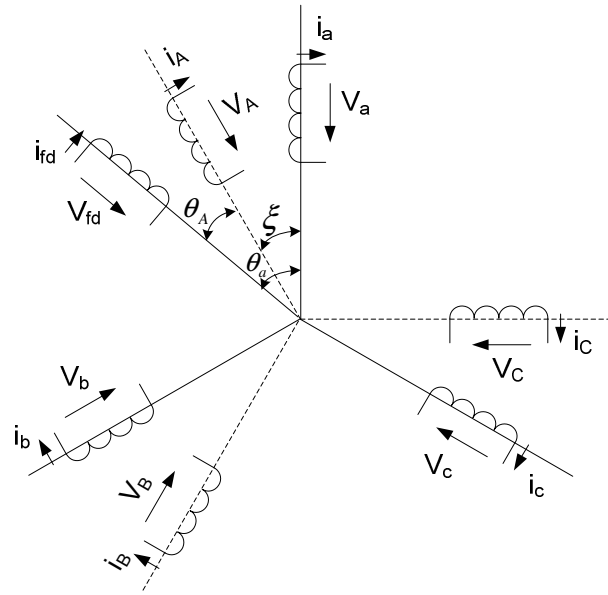


Fig. 3.18. Winding arrangement schematic of a dual winding PM actuator with an arbitrary angle,  $\zeta$ , between the two windings.

### 3.5.2 Dynamic Model of the Machine

This section approaches and studies the nonlinear analysis of the dual winding PM actuator and develops the nonlinear machine model.

Using Kirchoff's second law, one obtains the voltage equations of the stator circuits

(3.1).

$$v_x = p \phi_x - r i_x \quad (3.1)$$

where,  $x = a, b, c; A, B, C$ . The flux linkages in (3.1) can be written in matrix form as seen in (3.2).

$$[\phi_x] = [L_{x,y}] [i_x] \quad (3.2)$$

where,  $x = a, b, c; A, B, C$  and  $y = a, b, c; A, B, C$ . The terms on the diagonal of the inductance matrix are the self inductances and the off-diagonals are the mutual inductances. Equations (3.1) and (3.2) can thus be written in matrix form as shown in (3.3), where  $\Theta$  is the rotor position, and  $e_x$  is the back emf component generated by the

permanent magnet rotor. The first term of (3.3) represents the ohmic voltage drop in the six windings. The second term represents the transformer voltage component, and the last two terms represent the rotational voltage components [13].

$$\begin{aligned}
\begin{bmatrix} v_a \\ v_b \\ v_c \\ v_A \\ v_B \\ v_C \end{bmatrix} &= \begin{bmatrix} r_a & 0 & 0 & 0 & 0 & 0 \\ 0 & r_b & 0 & 0 & 0 & 0 \\ 0 & 0 & r_c & 0 & 0 & 0 \\ 0 & 0 & 0 & r_A & 0 & 0 \\ 0 & 0 & 0 & 0 & r_B & 0 \\ 0 & 0 & 0 & 0 & 0 & r_C \end{bmatrix} \begin{bmatrix} i_a \\ i_b \\ i_c \\ i_A \\ i_B \\ i_C \end{bmatrix} \\
&+ \begin{bmatrix} L_{aa} & L_{ab} & L_{ac} & L_{aA} & L_{aB} & L_{aC} \\ L_{ba} & L_{bb} & L_{bc} & L_{bA} & L_{bB} & L_{bC} \\ L_{ca} & L_{cb} & L_{cc} & L_{cA} & L_{cB} & L_{cC} \\ L_{Aa} & L_{Ab} & L_{Ac} & L_{AA} & L_{AB} & L_{AC} \\ L_{Ba} & L_{Bb} & L_{Bc} & L_{BA} & L_{BB} & L_{BC} \\ L_{Ca} & L_{Cb} & L_{Cc} & L_{CA} & L_{CB} & L_{CC} \end{bmatrix} \cdot \frac{d}{dt} \begin{bmatrix} i_a \\ i_b \\ i_c \\ i_A \\ i_B \\ i_C \end{bmatrix} \\
&+ \omega \left\{ \frac{d}{d\theta} \begin{bmatrix} L_{aa} & L_{ab} & L_{ac} & L_{aA} & L_{aB} & L_{aC} \\ L_{ba} & L_{bb} & L_{bc} & L_{bA} & L_{bB} & L_{bC} \\ L_{ca} & L_{cb} & L_{cc} & L_{cA} & L_{cB} & L_{cC} \\ L_{Aa} & L_{Ab} & L_{Ac} & L_{AA} & L_{AB} & L_{AC} \\ L_{Ba} & L_{Bb} & L_{Bc} & L_{BA} & L_{BB} & L_{BC} \\ L_{Ca} & L_{Cb} & L_{Cc} & L_{CA} & L_{CB} & L_{CC} \end{bmatrix} \right\} \cdot \begin{bmatrix} i_a \\ i_b \\ i_c \\ i_A \\ i_B \\ i_C \end{bmatrix} + \begin{bmatrix} e_a \\ e_b \\ e_c \\ e_A \\ e_B \\ e_C \end{bmatrix} \quad (3.3)
\end{aligned}$$

An expansion of the third term of (3.3) is shown in (3.4) – (3.9).

$$\begin{aligned}
v_{ar} &= \omega \left[ i_a \frac{d}{d\theta} L_{aa} + i_b \frac{d}{d\theta} L_{ab} + i_c \frac{d}{d\theta} L_{ac} \right. \\
&\quad \left. + i_A \frac{d}{d\theta} L_{aA} + i_B \frac{d}{d\theta} L_{aB} + i_C \frac{d}{d\theta} L_{aC} \right] \quad (3.4)
\end{aligned}$$

$$\begin{aligned}
v_{br} &= \omega \left[ i_a \frac{d}{d\theta} L_{ba} + i_b \frac{d}{d\theta} L_{bb} + i_c \frac{d}{d\theta} L_{bc} \right. \\
&\quad \left. + i_A \frac{d}{d\theta} L_{bA} + i_B \frac{d}{d\theta} L_{bB} + i_C \frac{d}{d\theta} L_{bC} \right] \quad (3.5)
\end{aligned}$$

$$\begin{aligned}
v_{cr} &= \omega \left[ i_a \frac{d}{d\theta} L_{ca} + i_b \frac{d}{d\theta} L_{cb} + i_c \frac{d}{d\theta} L_{cc} \right. \\
&\quad \left. + i_A \frac{d}{d\theta} L_{cA} + i_B \frac{d}{d\theta} L_{cB} + i_C \frac{d}{d\theta} L_{cC} \right] \quad (3.6)
\end{aligned}$$

$$v_{Ar} = \omega \left[ i_a \frac{d}{d\theta} L_{Aa} + i_b \frac{d}{d\theta} L_{Ab} + i_c \frac{d}{d\theta} L_{Ac} \right. \\ \left. + i_A \frac{d}{d\theta} L_{AA} + i_B \frac{d}{d\theta} L_{AB} + i_C \frac{d}{d\theta} L_{AC} \right] \quad (3.7)$$

$$v_{Br} = \omega \left[ i_a \frac{d}{d\theta} L_{Ba} + i_b \frac{d}{d\theta} L_{Bb} + i_c \frac{d}{d\theta} L_{Bc} \right. \\ \left. + i_A \frac{d}{d\theta} L_{BA} + i_B \frac{d}{d\theta} L_{BB} + i_C \frac{d}{d\theta} L_{BC} \right] \quad (3.8)$$

$$v_{Cr} = \omega \left[ i_a \frac{d}{d\theta} L_{Ca} + i_b \frac{d}{d\theta} L_{Cb} + i_c \frac{d}{d\theta} L_{Cc} \right. \\ \left. + i_A \frac{d}{d\theta} L_{CA} + i_B \frac{d}{d\theta} L_{CB} + i_C \frac{d}{d\theta} L_{CC} \right] \quad (3.9)$$

An understanding of the value of the inductances in (3.4) – (3.9) was derived in detail in [13]. We will only use the results reached by the previous work to help us develop the dynamic model of the machine. It is assumed that the stator winding is sinusoidally distributed. Thus, the self inductances for the stator windings can be written as shown in (3.10).

$$L_{xx} = L_{aa0} + L_{aa2} \cos(2\theta_x) \quad (3.10)$$

where  $x = a, b, c$ ;  $A, B, C$ ,  $\theta_a = \omega t + \theta_0$ ,  $\theta_b = \omega t + \theta_0 - 120^\circ$ ,  $\theta_c = \omega t + \theta_0 + 120^\circ$ ,  $\theta_A = \theta_a - \xi$ ,  $\theta_B = \theta_b - \xi$ ,  $\theta_C = \theta_c - \xi$ ,  $L_{aa0} \propto^l (P_d + P_q)/2$ ,  $L_{aa2} \propto^l (P_d - P_q)/2$ . For surface mount permanent magnet machines,  $L_{aa2} = 0$ . This is the ideal case, and will simplify the discussions in the following sections. Thus, all the position dependent terms of the self inductances are zero. The mutual inductances of (3.11) can also be reduced to (3.12). The mutual inductance between the two sets of windings can also be reduced to a set of three mutual inductance values as shown in (3.13) – (3.15). Similar to the self inductances, the position dependent terms equal zero. Thus, all terms of (3.4) – (3.9) are reduced to zero. The mutual inductance proportionalities shown in (3.16) – (3.18) are

crucial terms for the work at hand. The objective is to utilize these mutual inductances to “vary” or reduce the output dc voltage of the dc winding when the brake winding is at higher speeds and loads while maintaining the higher terminal voltage at lower speeds to enable a wider operating speed range for the tool.

$$\begin{aligned} L_{ab} &= L_{ba} = L_{bc} = L_{cb} = L_{ca} = L_{ac} = L_{AB} \\ &= L_{BA} = L_{BC} = L_{CB} = L_{CA} = L_{AC} = -L_{ab0} \end{aligned} \quad (3.11)$$

$$L_{ab0} \propto^l (P_d + P_q)/4 \quad (3.12)$$

$$L_{aA} = L_{Aa} = L_{bB} = L_{Bb} = L_{cC} = L_{Cc} = -L_{aA0} \quad (3.13)$$

$$L_{aB} = L_{Ba} = L_{bC} = L_{Cb} = L_{cA} = L_{Ac} = -L_{aB0} \quad (3.14)$$

$$L_{aC} = L_{Ca} = L_{bA} = L_{Ab} = L_{cB} = L_{Bc} = -L_{aC0} \quad (3.15)$$

$$L_{aA0} \propto^l -(P_d + P_q)(\cos(\xi))/2 \quad (3.16)$$

$$L_{aB0} \propto^l (P_d + P_q)(\cos(\xi) + \sqrt{3} \sin(\xi))/4 \quad (3.17)$$

$$L_{aC0} \propto^l (P_d + P_q)(\cos(\xi) - \sqrt{3} \sin(\xi))/4 \quad (3.18)$$

The general form for the value of inductance is given by (3.19). One can thus come to the conclusion that if  $i_1 = i_2 = i_3$  then, (3.20) can be reduced to the proportionality in (3.21)

$$L = \phi/i \quad (3.19)$$

$$L_{aA} + L_{bA} + L_{cA} = \phi_1/i_1 + \phi_2/i_2 + \phi_3/i_3 \quad (3.20)$$

$$L_{aA} + L_{bA} + L_{cA} \propto^l \phi_1 + \phi_2 + \phi_3 \quad (3.21)$$

An observation of (3.22) – (3.24) does in fact show that the currents in (3.20) are all equal to  $i_A$ , thus, it is safe to conclude that (3.21) will hold true. Using (3.16) – (3.18) as

values for the inductances in (3.21), one can see the apparent effect of phase displacement  $\xi$  on the terminal quantities. It is also clear that the sum of the inductances does give an indication of amount of coupling due to the mutual inductances between the two winding sets. Thus, it is termed as the coupling factor in Fig. 3.19. Similar relationships can be derived for the inductances, and hence flux, caused by the other phase currents. The top plot of Fig. 3.19 shows a plot of the absolute value of the variation of the mutual inductances of (3.16) – (3.18) with the phase displacement,  $\xi$ . The bottom plot of Fig. 3.19 is the sum of the three values plotted against the same variable as shown in (3.21). It can be seen that mutual coupling is most significant at integer multiples of  $\pm\pi/3$ , and least at integer multiples of  $\pm\pi/6$ . Thus, for the application at hand, the two sets of windings will be placed in phase with one another. This is one value of  $\xi$  that will provide maximum coupling as shown in Fig. 3.19.

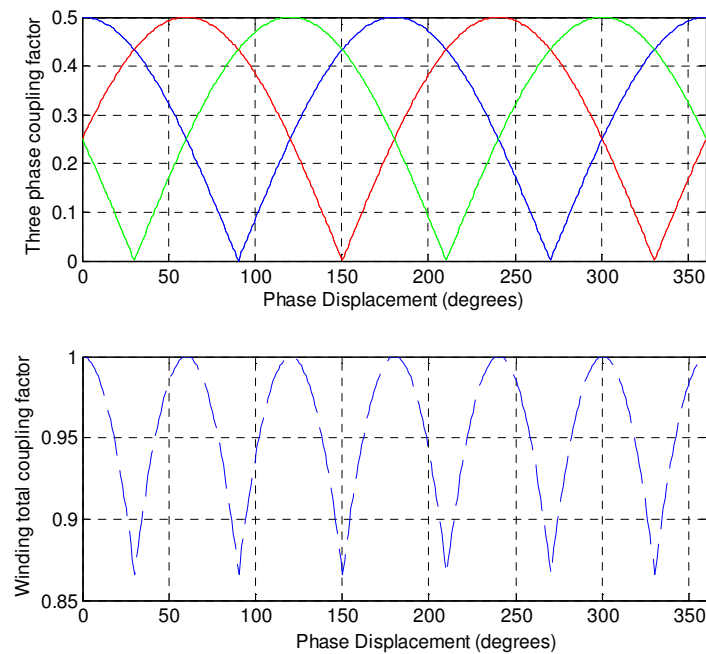


Fig. 3.19. Effect of phase displacement,  $\xi$ , on the mutual coupling between the dc and brake windings.

The transformer voltage terms of equation three can be written as shown in (3.19) – (3.24).

$$v_{Ma} = L_{ab} \frac{d}{dt} i_b + L_{ac} \frac{d}{dt} i_c + L_{aA} \frac{d}{dt} i_A + L_{aB} \frac{d}{dt} i_B + L_{aC} \frac{d}{dt} i_C \quad (3.22)$$

$$v_{Mb} = L_{ba} \frac{d}{dt} i_a + L_{bc} \frac{d}{dt} i_c + L_{bA} \frac{d}{dt} i_A + L_{bB} \frac{d}{dt} i_B + L_{bC} \frac{d}{dt} i_C \quad (3.23)$$

$$v_{Mc} = L_{ca} \frac{d}{dt} i_a + L_{cb} \frac{d}{dt} i_b + L_{cA} \frac{d}{dt} i_A + L_{cB} \frac{d}{dt} i_B + L_{cC} \frac{d}{dt} i_C \quad (3.24)$$

$$v_{MA} = L_{Aa} \frac{d}{dt} i_a + L_{Ab} \frac{d}{dt} i_b + L_{Ac} \frac{d}{dt} i_c + L_{aB} \frac{d}{dt} i_B + L_{aC} \frac{d}{dt} i_C \quad (3.25)$$

$$v_{MB} = L_{Ba} \frac{d}{dt} i_a + L_{Bb} \frac{d}{dt} i_b + L_{Bc} \frac{d}{dt} i_c + L_{BA} \frac{d}{dt} i_A + L_{BC} \frac{d}{dt} i_C \quad (3.26)$$

$$v_{MC} = L_{Ca} \frac{d}{dt} i_a + L_{Cb} \frac{d}{dt} i_b + L_{Cc} \frac{d}{dt} i_c + L_{CA} \frac{d}{dt} i_A + L_{CB} \frac{d}{dt} i_B \quad (3.27)$$

The preceding equations were used to develop the dynamic model of the machine. The model shown in Fig. 3.20 has been developed and simulated in PSIM. Since it is a time domain circuit model, this was found to be a very suitable platform for such a machine.

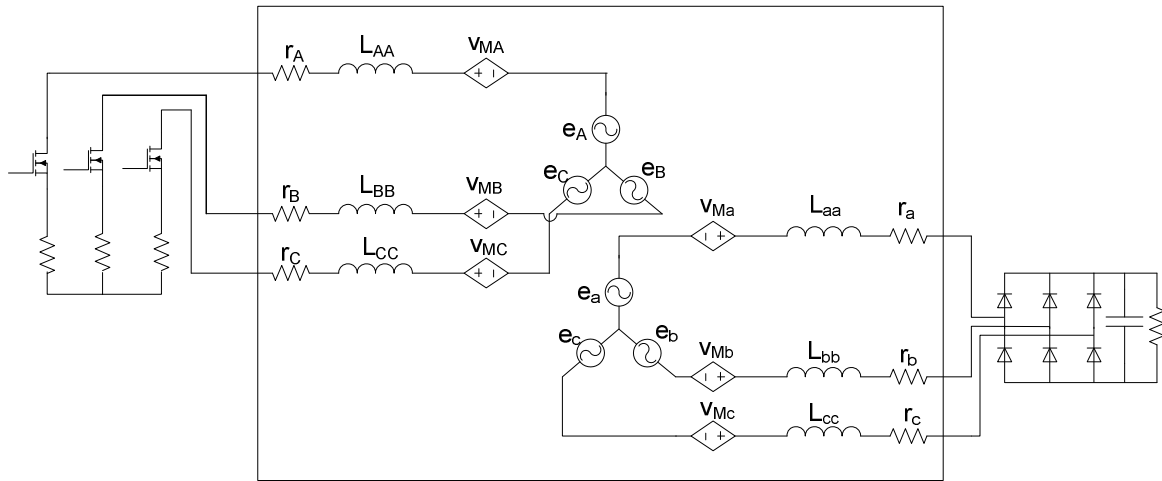


Fig. 3.20. Simulation model of a dual winding PM actuator.

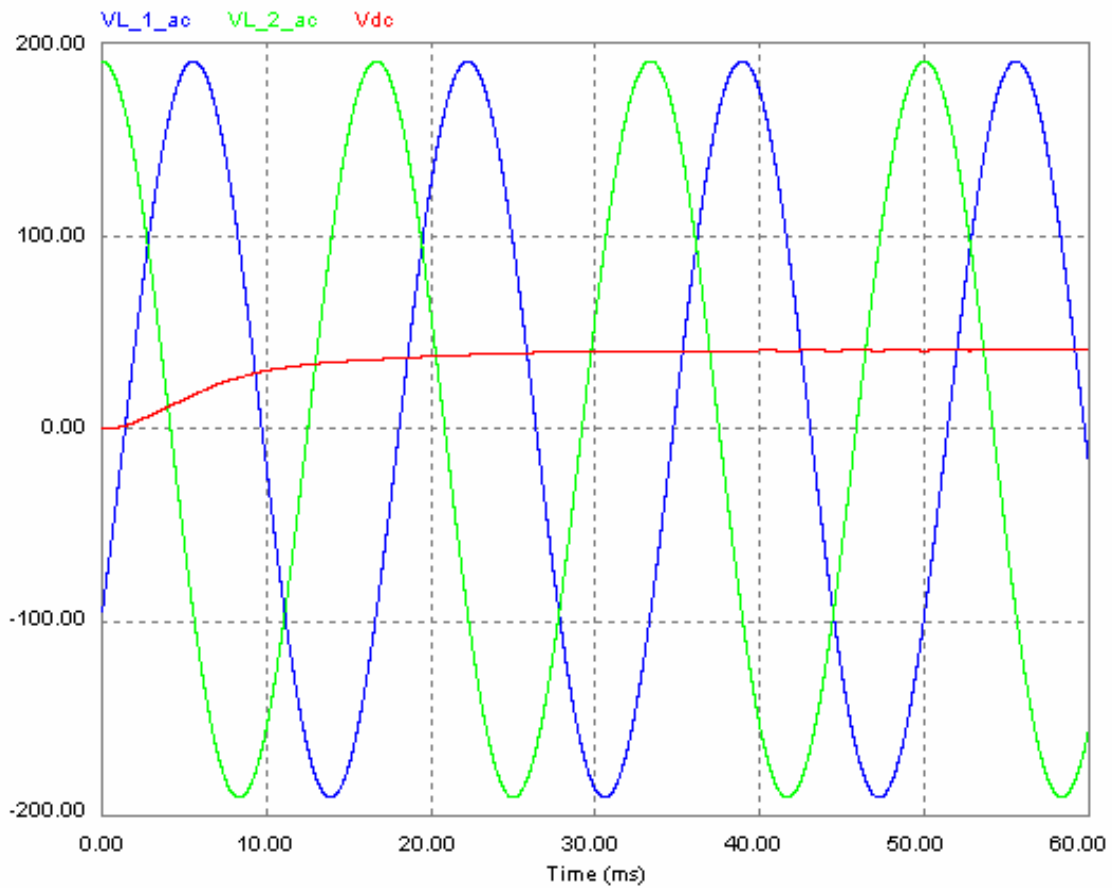


Fig. 3.21. Brake winding terminal voltages and generator winding rectified voltage (red) for 0 % braking.

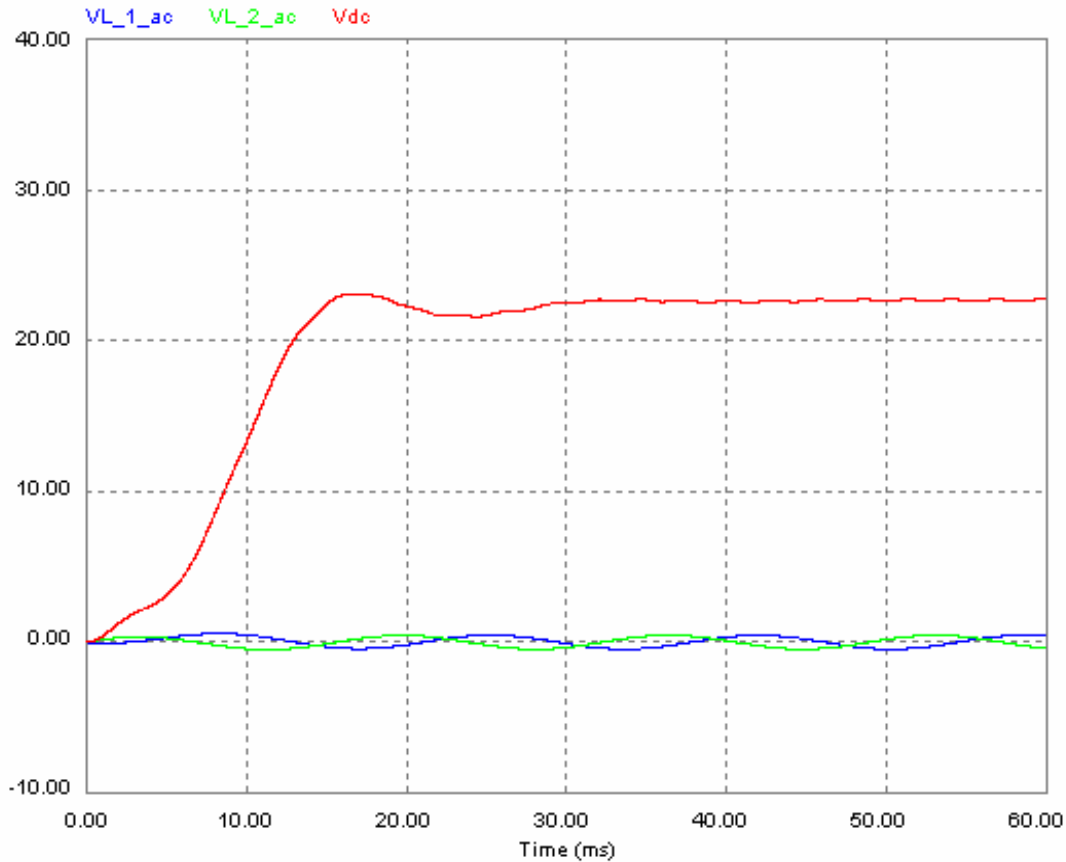


Fig. 3.22. Brake winding terminal voltage and generator winding rectified voltage (red) for 95 % braking.

The developed model was derived based on [13] and its effectiveness was verified by comparing the results of [13] to a separate model of the machine architecture discussed in that work. Two operating conditions of the dual winding permanent magnet actuator have been simulated. The effect of a lower braking torque on the terminal voltage of the brake winding and the dc output is shown in Fig. 3.21. Full braking torque is simulated in Fig. 3.22, and the corresponding effect on the brake winding and dc output is shown. It can be seen that at full braking torque, the value of the dc output is decreased due to the coupling between the two sets of windings. Thus, the utilization of the coupling between the two sets of windings, can produce the desired effect of reducing the output

dc voltage, or field weakening at higher speeds and loads. It is important to note that for the application at hand, higher speeds only occur in the presence of higher braking loads.

### 3.5.3 Rotor Reference Frame Equivalent Circuit Model

The previous section has addressed the machine model and the dynamics of the system at hand using an abc reference frame. Assumptions were made to simplify the model and help emphasize the main ideas. If a more detailed dynamic model and analysis is required, an abc frame model would prove to be difficult to analyze and time consuming to solve. When the appropriate rotating reference frame transformation is applied to the winding variables, the resulting equations are much easier to deal with [14]. For the dual winding, or six phase machine under consideration, this involves referring the winding variables (abc, ABC) to the common d-q reference frame of the permanent magnet rotor. The required transformation is of the form shown in (3.28). For the sake of simplicity, we will only consider balanced operation of the machine. Thus, (3.28) can be expanded into the terms shown in (3.29) – (3.31).

$$\bar{f}_r = \bar{K}(\theta_r) \bar{f} \quad (3.28)$$

$$\bar{f}_r = \begin{bmatrix} f^r_{q1} & f^r_{d1} & f^r_{q2} & f^r_{d2} \end{bmatrix}^t \quad (3.29)$$

$$\bar{K} = \text{block diag} [K(\theta_r) \quad K(\theta_r - \xi)] \quad (3.30)$$

$$K(\theta_r) = \frac{2}{3} \begin{bmatrix} \cos(\theta_r) & \cos(\theta_r - 2\pi/3) & \cos(\theta_r + 2\pi/3) \\ \sin(\theta_r) & \sin(\theta_r - 2\pi/3) & \sin(\theta_r + 2\pi/3) \\ \frac{1}{\sqrt{2}} & \frac{1}{\sqrt{2}} & \frac{1}{\sqrt{2}} \end{bmatrix} \quad (3.31)$$

The resultant rotor reference frame equations are similar to those for a pair of three phase permanent magnet synchronous machines with common magnetizing inductances except for some additional terms associated with the stator winding mutual leakage

inductances [14].

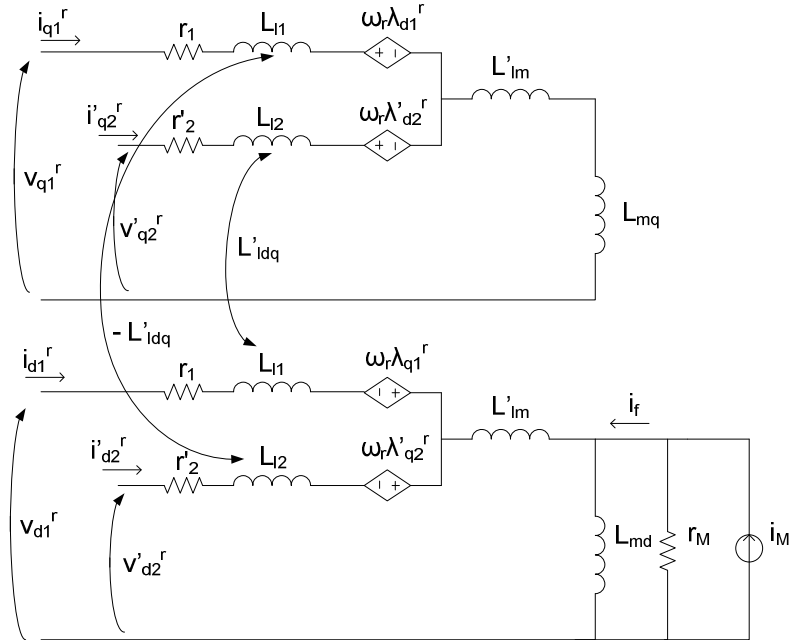


Fig. 3.23. d-q equivalent circuit model of the dual winding machine.

The system of equations used to develop the equivalent circuit of Fig. 3.23 is similar to that presented in [14] except that a permanent magnet rotor is used instead of the field windings. Thus, the system of equations will not be derived here in detail, but will be presented in the Appendix. The prime quantities are referred to the abc windings. The mutual leakage coupling between the stator windings is represented by  $\pm L_{dq}$ . Since the equations were reduced to those of two separate three phase machines with a common magnetizing inductance and mutual leakage inductances, it is reasonable to investigate the steady state phasor diagram of a single machine and extend the results to the dual winding machine.

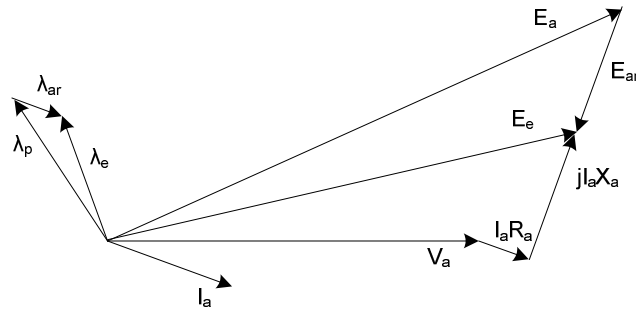


Fig. 3.24. Phasor diagram for normal operating conditions.

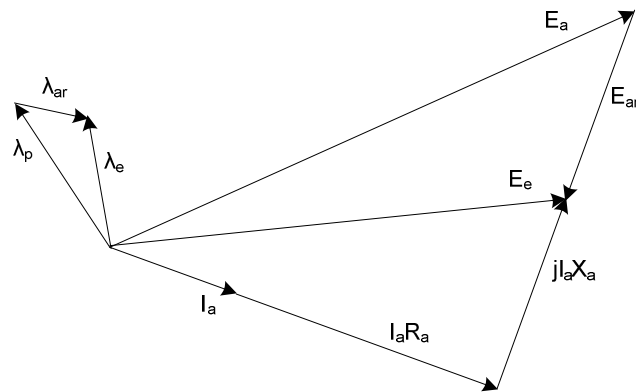


Fig. 3.25. Phasor diagram for operation with shorted terminals.

Under normal operation, Fig. 3.24, if  $\lambda_p$  is the flux per pole in the machine under no load, then the generated voltage  $E_a$  must lag  $\lambda_p$  by  $90^\circ$ . Since the power factor is lagging, the phase current  $I_a$  lags the terminal phase voltage  $V_a$ . As the phase current passes through the armature winding, its magnetomotive force (mmf) produces flux  $\lambda_{ar}$  which is in phase with  $I_a$ . The effective flux per pole  $\lambda_e$  in the machine is the algebraic sum of the two fluxes. Under the shorted terminal condition, similar logic can be used, but considering  $V_a = 0$ . This implies that the voltage drop across the machine's reactance

will balance the machines effective generated voltage. It should be noted here that with the higher values of current, the armature reaction has a more significant effect, which reduces or weakens the effective generated voltage as seen in Fig. 3.25 with respect to that in Fig. 3.24.

The rotor reference frame equations have been derived based on [14] and are similar to those for a pair of three phase permanent magnet synchronous machines with a common magnetizing inductance except for some additional terms associated with the stator winding mutual leakage inductances.

The voltage equations of the dual winding actuator, or six phase PM machine in the rotor reference frame for a balanced set of windings are:

$$v_{q1}^r = r_1 i_{q1}^r + \omega_r \lambda_{d1}^r + p \lambda_{q1}^r \quad (3.32)$$

$$v_{d1}^r = r_1 i_{d1}^r - \omega_r \lambda_{q1}^r + p \lambda_{d1}^r \quad (3.33)$$

$$v_{q2}^r = r_2 i_{q2}^r + \omega_r \lambda_{d2}^r + p \lambda_{q2}^r \quad (3.34)$$

$$v_{d2}^r = r_2 i_{d2}^r - \omega_r \lambda_{q2}^r + p \lambda_{d2}^r \quad (3.35)$$

where

$$\begin{aligned} \lambda_{q1}^r &= L_{l1} i_{q1}^r + L_{lm} (i_{q1}^r + i_{q2}^r) - L_{ldq} i_{d2}^r \\ &+ L_{mq} (i_{q1}^r + i_{q2}^r) \end{aligned} \quad (3.36)$$

$$\begin{aligned} \lambda_{d1}^r &= L_{l1} i_{d1}^r + L_{lm} (i_{d1}^r + i_{d2}^r) + L_{ldq} i_{q2}^r \\ &+ L_{md} (i_{d1}^r + i_{d2}^r + i_f^r) \end{aligned} \quad (3.37)$$

$$\lambda_{q2}^r = L_{l2} i_{q2}^r + L_{lm} (i_{q1}^r + i_{q2}^r) + L_{ldq} i_{d1}^r$$

$$+ L_{mq}(i'_{q1} + i'_{q2}) \quad (3.38)$$

$$\begin{aligned} \lambda'_{d2} &= L_{l2}i'_{d2} + \dot{L}_{lm}(i'_{d1} + i'_{d2}) - \dot{L}_{ldq}i'_{q1} \\ &+ L_{md}(i'_{d1} + i'_{d2} + i'_{f}) \end{aligned} \quad (3.39)$$

and

$$\begin{aligned} L_{lm} &= L_{aA} \cos(\xi) + L_{aB} \cos(\xi + 2\pi/3) \\ &+ L_{aC} \cos(\xi - 2\pi/3) \end{aligned} \quad (3.40)$$

$$\begin{aligned} L_{ldq} &= L_{aA} \sin(\xi) + L_{aB} \sin(\xi + 2\pi/3) \\ &+ L_{aC} \sin(\xi - 2\pi/3) \end{aligned} \quad (3.41)$$

$$L_{l1} = L_{ls1} - \dot{L}_{lm} \quad (3.42)$$

$$L_{l2} = \dot{L}_{ls2} - \dot{L}_{lm} \quad (3.43)$$

$$\dot{L}_{lm} = \frac{N_1}{N_2} L_{lm} \quad (3.44)$$

$$\dot{L}_{ldq} = \frac{N_1}{N_2} L_{ldq} \quad (3.45)$$

The effective number of turns of the abc and ABC windings are  $N_1$  and  $N_2$  respectively.

The prime quantities are referred to the abc windings.

### 3.5.4 Experimental Results

The prototype machine constructed to demonstrate the presented theory is shown in Fig. 3.26. The new machine, however, achieved another purpose. The combination of the two windings into one stack enabled the elimination of two end windings shown in Fig. 3.2. The extra volume was utilized in increasing the length of the new machine,

thus, improving the braking capability of the tool while maintaining the same actuator volume. This was seen as another significant advantage in the use of the dual winding machine over the existing solution. Experimental results on the new machine are shown in Figs. 3.27 and 3.28. The effect of the coupling between the two sets of windings on the dc output in the presence of various levels of braking is shown in Fig. 3.29. It can be seen that the lower braking duty cycles do not adversely affect the output dc voltage, thus maintaining a high terminal voltage at lower speeds which widens the operating range of the tool. At higher speeds and loads, higher braking torque is applied and a significant reduction in output dc voltage is observed. It is also seen that even at higher braking loads in the lower speed range, the tool operation is not adversely affected, since the bottom threshold of power supply operation was exceeded. This may allow for new operating techniques of the tool.



Fig. 3.26. Prototype dual winding stator.

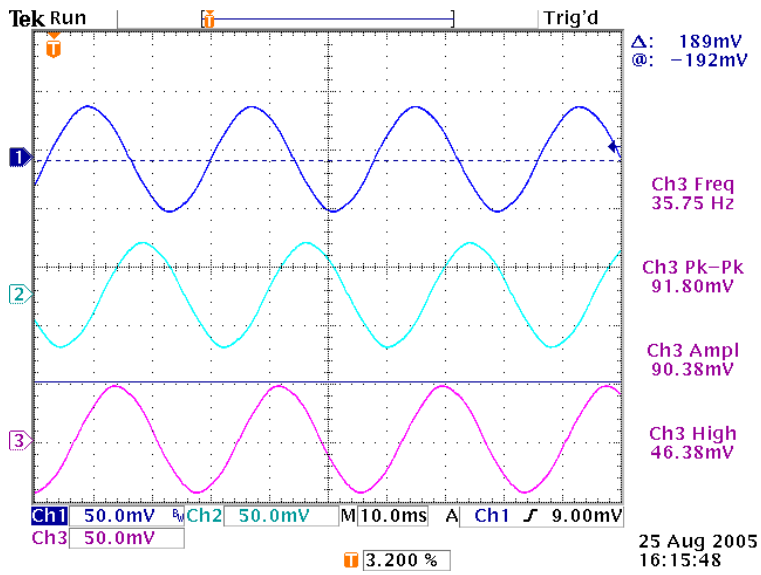


Fig. 3.27. Brake winding current (10 A/div).

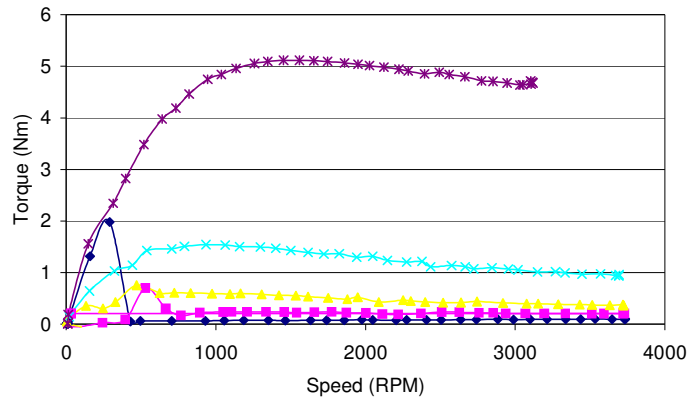


Fig. 3.28. Braking winding torque at various braking duty cycles.

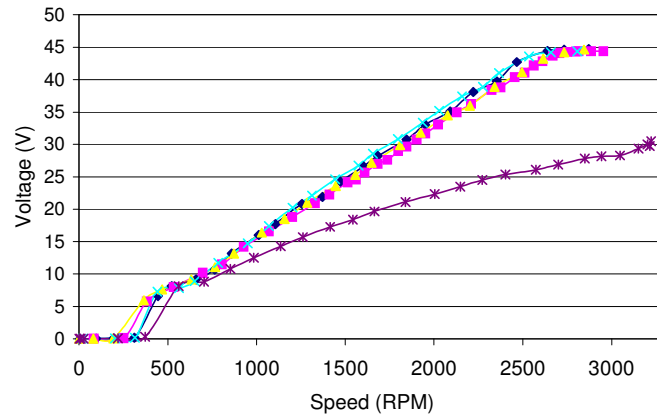


Fig. 3.29. Dc output voltage at various brake winding duty cycles over the speed range.

### **3.6 Conclusion**

This work has demonstrated the effective utilization of application considerations and the nature of the connected load in the design and application of electrical machines for demanding applications. It is apparent that the application at hand is unique in its utilization of PM machines. The work at hand utilized the available volume and produced a significantly improved actuator. The different phases of the actuator improvement were discussed. This was concluded with the design of a dual winding or six phase PM actuator. The coupling between the two sets of windings was used in favor of the application. A dynamic model of the dual winding exterior rotor PM actuator was developed along with a d-q steady state one. The advantage of utilizing the coupling between the sets of windings for the application at hand was demonstrated using the dynamic model. Experimental results corroborating the presented theory and simulations demonstrated the effectiveness of the presented theory. The utilization of a dual winding machine for the application at hand also produced significant improvements in the braking torque capability of the brake winding. This was mainly due to the ability to eliminate two sets of end windings and effectively utilize the original actuator volume.

## CHAPTER IV

### APPLICATION CONSIDERATIONS IN HARSH ENVIRONMENT POWER ELECTRONIC ENERGY CONVERSION SYSTEMS

#### 4.1 Introduction

Thermal constraints on the power electronic subsystems have placed a severe limitation on the development of next generation power electronic systems for use in compact harsh environments. The need for remote actuators, point-of-use power supplies, and distributed high power control systems in the automotive, aerospace, well logging, and industrial control environments is on the rise due to the advantages gained on the reliability, serviceability, power distribution trends etc. The ability to operate power electronic systems without the need for active cooling is seen as a critical technology, and is the subject of the work at hand. The current work will start by assessing the basic device choices and their applicability for operation at elevated temperatures. Experimental results will then be conducted to verify the conclusions made. The interaction of the selected devices under different operating conditions is also assessed. Comprehensive power loss studies are conducted using simulation and experimental verification. A simple novel solution to one of the failure modes noticed from the device interaction is presented. To enable the operation at higher power, a custom power module is designed based on extensive thermal and thermo-mechanical considerations. Simulation results corroborated by experimental results on the developed power module conclude the work at hand. It is found that some silicon devices, passive components, packaging techniques and materials typically used at room temperature can be used up to 200°C.

## 4.2 Power Device Selection and Testing

The type of switching device to use is one question that needed an answer in the early stages of this work. The choice was really between the use of an IGBT or a Mosfet for the application at hand, knowing that the power electronic subsystem was required to operate with no active cooling at an ambient temperature of 200°C. Currents upto 12 Arms needed to be switched, and voltage levels upto 1000 V were the target. Although the main selections were between silicon devices, the advent of silicon carbide devices prompted the extension of the study at hand to include this device technology.

Studies [15][16] have demonstrated the successful use of Mosfets at elevated temperatures. The evolution of Mosfet parameters with temperature support this fact. The most significant change is the increase of the drain-source on resistance with increasing temperatures. Moreover, a decrease in gate-source threshold voltage, and an increase in leakage current can also be seen as effects of elevated temperature. One favorable effect is actually the increase in breakdown voltage in a Mosfet with the temperature increase [15]. For the IGBT, a noticeable increase in reverse recovery, leakage current, and stored charge are the main phenomena appearing as the temperature increases. Perhaps the most significant phenomenon is the increase in stored charge which in turn increases the switching time of the IGBT. This increase in switching time causes excessive losses in the IGBT, and eventual failure of the device. Thus, the results of the current research [17][18] illustrated the promising use of Mosfets at elevated temperatures. However, the work at hand will verify this conclusion by conducting extensive testing on both device technologies. So, it can be concluded that based on results of current research, it is possible to use silicon for applications up to 200°C,

before there is a need to switch to wider bandgap semiconductor materials, such as GaAs, and SiC, or SOI. Because wide bandgap devices produces a smaller concentration of intrinsic carries than silicon at elevated temperatures [18], the device operating range can be extended. GaAs extends the operating range to about 300°C. Defect density and the development of metallization and interconnect schemes are holding back the commercial development of SiC devices. The isolating layer in silicon on insulator technology eliminates the ability to use the backside of the device for grounding, a critical design feature of many power transistors. From the preceding discussion it was seen that consideration of SiC would be a benefit to the study at hand. A need for power diodes is also seen as an important consideration in the device selection process. Unlike its switching counterpart, the SiC schottky diode has commercially demonstrated compelling system benefits in the last years. Its superior performance made this task a much simpler one than that of the switching device. However, silicon schottky devices were also tested to support the study. This is mainly due to the high forward voltage drop of SiC schottky diodes.

#### **4.2.1 Description of the Qualification Tests**

Various qualification tests need to be carried out on the switching devices before their acceptance for use in a harsh environment application. Among the tests to be carried out are :

- Static  $R_{\text{dson}}$  measured at known current and voltage;
- Dynamic or switched  $R_{\text{dson}}$  test at a known current, voltage, frequency, and duty cycle;
- Off state leakage current at a known voltage;

- Body diode static  $V_f$  measured at a set of input currents;
- $V_{ceon}$  over various  $V_{ge}$  voltages and temperatures for IGBTs.

These engineering tests will be used to determine the suitability of this device type for motor drive and other high power control circuits. Typically, a characterization sweep is performed prior to a steady state test temperature test. Another characterization sweep is performed following the steady state temperature test. The characterization sweep set points are: 150, 160, 170, 180, 185, 190, 195, 200, 205, 210, 215, 220, 225, 230, 225, 220, 215, 210, 205, 200, 195, 190, 185, 180, 170, 160, and 150°C with 2 hour dwells. The steady state temperature test will be conducted at 230°C for 200 hours. Chamber Air temperature is controlled in close proximity to the two heat sinks.

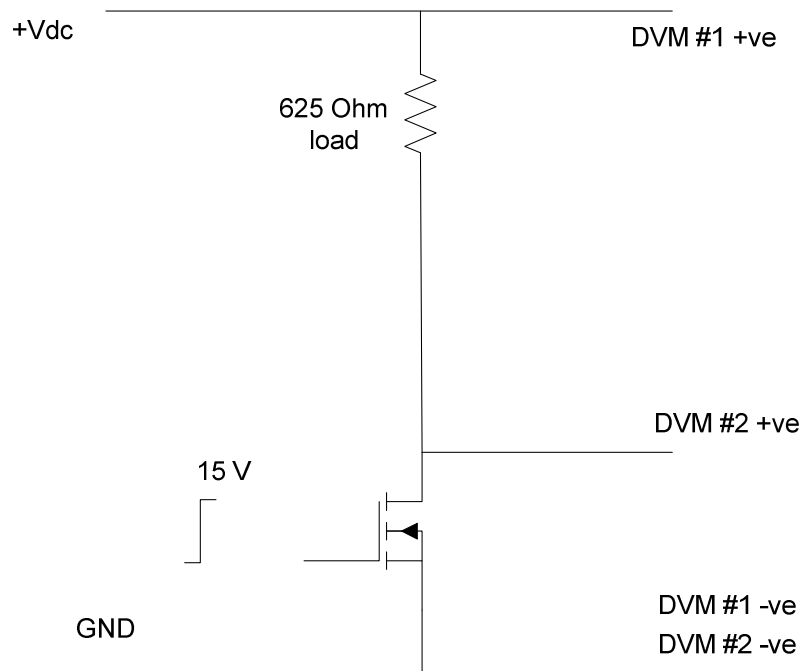


Fig. 4.1. Static  $R_{ds(on)}$  setup

The remaining portion of this section will be devoted to the description of the basic setups and measurements needed to perform the various tests. The experimental setup related to the static  $R_{dson}$  measurement is shown in Fig. 4.1, and the calculation of  $R_{dson}$  is as shown in (4.1). Fig. 4.2 details the setup and measurement needs for the dynamic  $R_{dson}$  measurement. In this case, one would need to measure the minimum amplitude over the measure zone after the switching loss has decayed to a minimum.

$$R_{dson} = V_{dson} / ((+V_{dc} - DVM \#2) / 650) \quad (4.1)$$

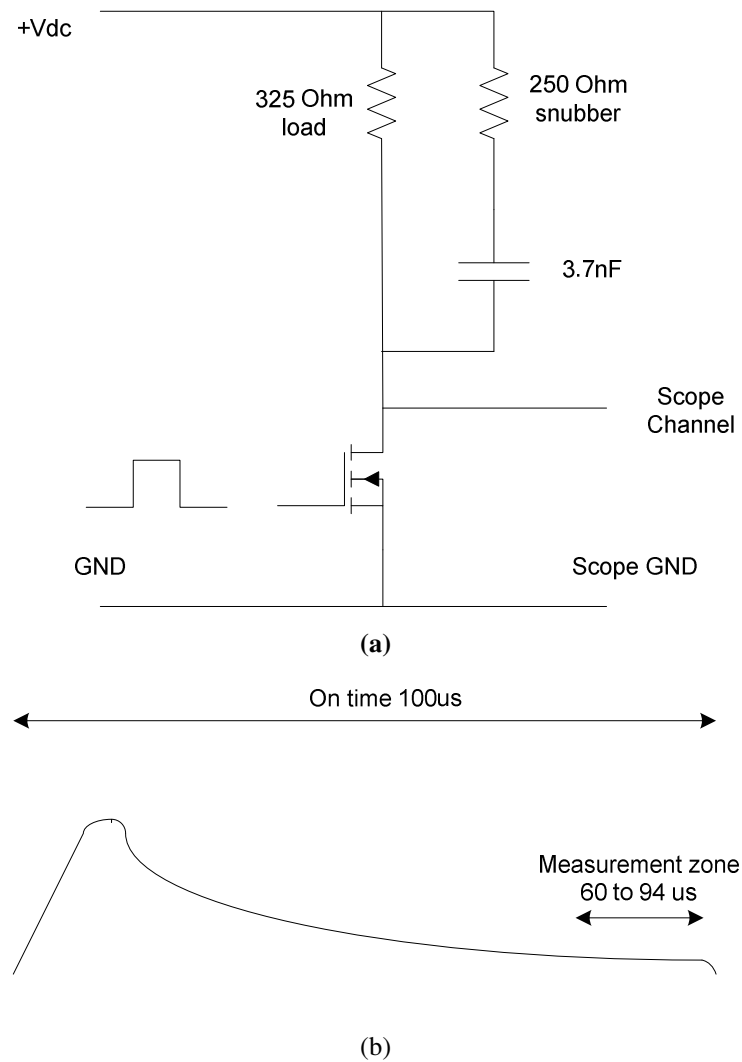


Fig. 4.2. Dynamic  $R_{dson}$  measurement setup (a) and principle (b)

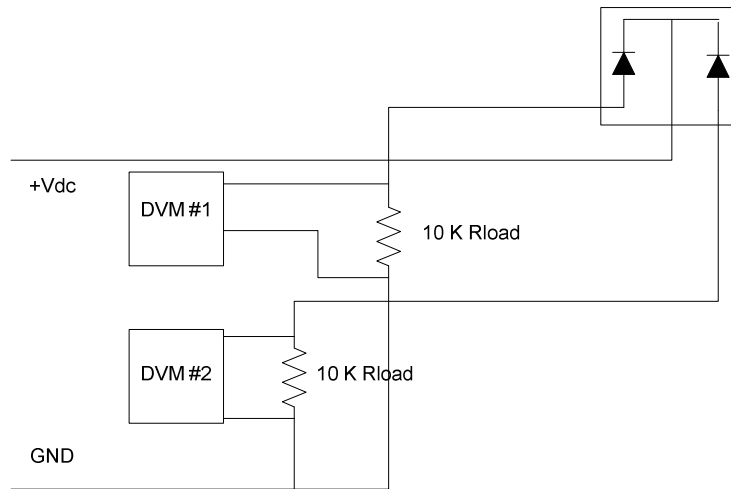


Fig. 4.3. Diode  $V_f$  drop experimental setup

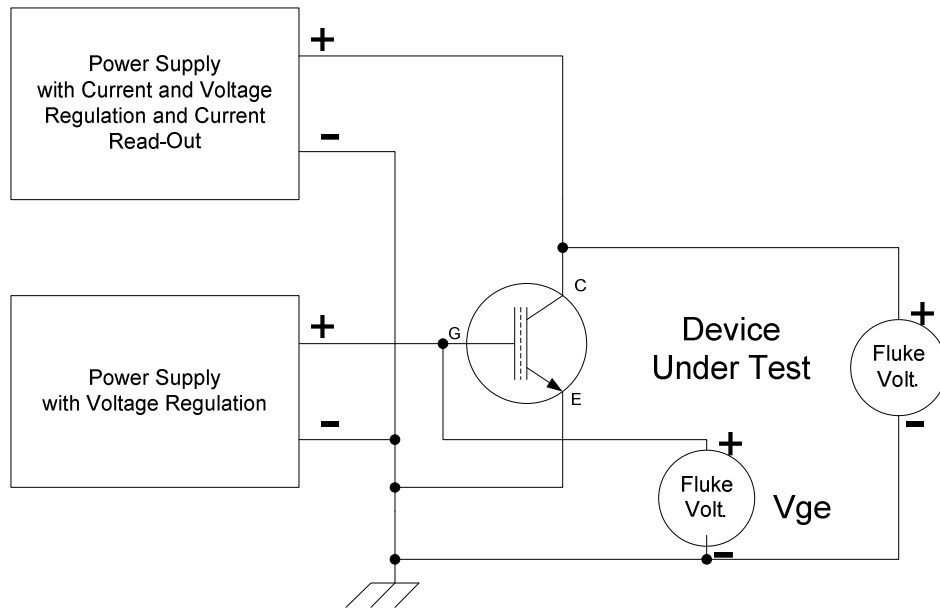


Fig. 4.4.  $V_{ce(on)}$  for different  $V_{ge}$  at various temperatures for the IGBT

Fig. 4.3 demonstrates the setup used to measure the forward voltage drop on the diode. The power supply current is controlled in order to measure the forward voltage drop corresponding to various load currents and different temperatures. Fig. 4.4 then

demonstrates the tests related to IGBT testing. A regulated power supply is used to either not supply the gate, and thus, leakage current measurements are taken.  $V_{ce}$  voltage measurements are then taken for various gate voltages controlled by the supply.

## **4.2.2 System Impact of Si vs SiC**

### **4.2.2.1 Silicon Carbide Technology and Impacts**

The emergence of silicon carbide SiC based power semiconductor switches with their many apparent application benefits compared to silicon based switches has resulted in substantial improvements in the performance of power electronic conversion systems. The promises that SiC brings are compactness, light weight, higher efficiency, higher voltages, higher temperature operation etc. The obvious push of the automotive market for the success of these devices is thus justified. Although the defect density problems the technology has been facing seem to be managed at the time of writing this dissertation, many packaging and topology issues are still not fully solved. This has hindered the widespread commercial use of such devices, although, it may be possible to purchase low quantities from some vendors at a premium price.

It is a common understanding that the temperature limit for most silicon devices is 150°C, therefore, keeping the junction temperature under this limit is important for the reliable operation of the devices. Even if such a precaution is followed, the variation of electrical characteristics with temperature may prove to be a major reliability concern. In many cases the need for effective thermal design will have to be tied to the electrical design. There are three standard options for cooling the devices in most applications, namely, natural air, forced air, or water-cooled heat sinks. Most cooling options however, are not feasible for oil well logging applications, the main driver for the work

at hand. The power rating of the converter determines the type and size of the heat sink. A heatsink typically occupies one-third of the total volume for a power converter and usually weighs more than the converter itself. This is of major concern in compact harsh environments. These considerations have prompted the consideration of SiC for the application at hand. Testing results for both silicon and SiC will be presented in the following subsections.

#### 4.2.2.2 Switching Device Test Results – SiC Case

In this and upcoming sections, the qualification tests described above will be carried out on different devices. It is important to note here that only the most significant tests results will be presented and described. Throughout the course of this work, approximately 40 power devices have been qualified. These devices range between, silicon Mosfets, silicon igbts, and SiC JFETS. It should be noted here that all testing was carried out approximately one year before this dissertation was written.

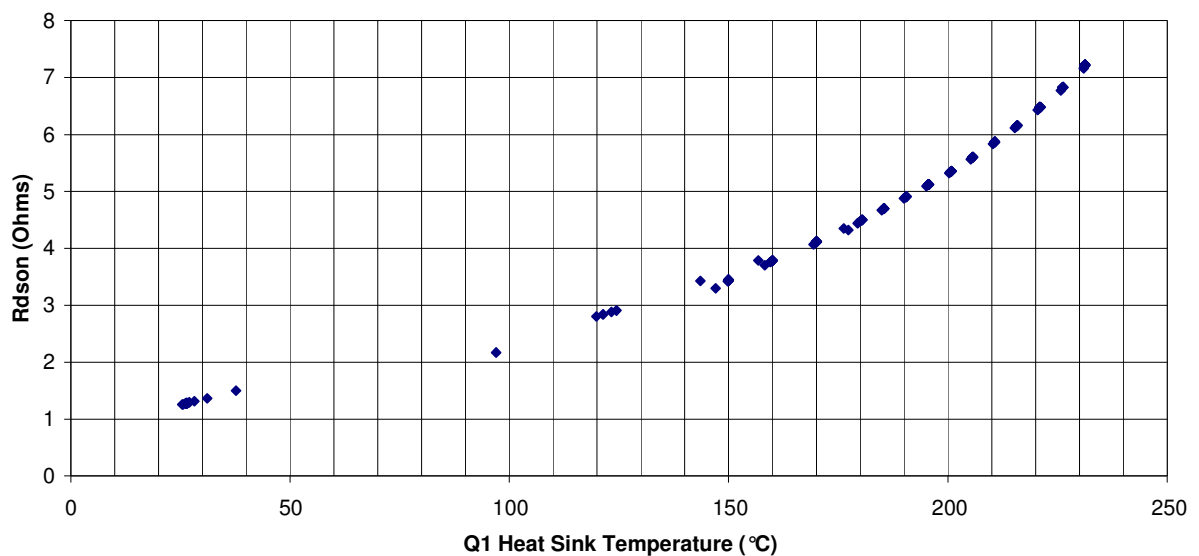


Fig. 4.5. SiC 1500 V Cascode Power Mosfet Static  $R_{ds(on)}$  at 650 V/ 1A versus temperature

This section presents the results performed on a SiC JFET. It is noted here that this was the only device available for purchase at the time of the study. Even though literature today may have a myriad of studies on applications of SiC technologies, it is still not possible to purchase from other vendors even at significantly high prices. The device at hand is rated for 1.5kV and 3A. It may be worth noting here that during the course of this study, a quote for a 1.5kV and 12 A device was approximately \$10,000 per device.

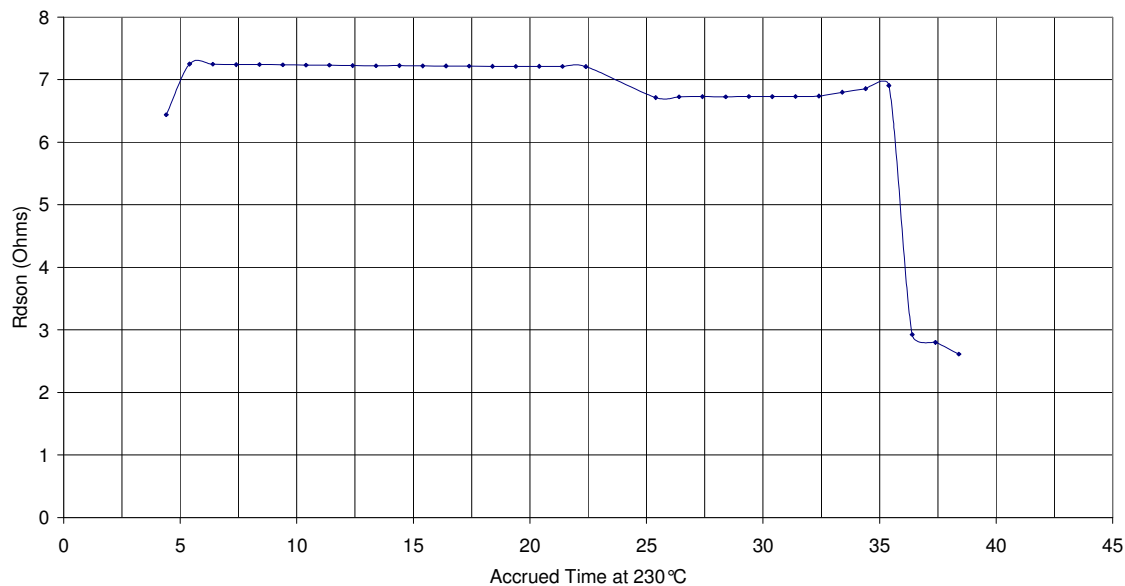


Fig. 4.6. SiC 1500 V Cascode Power Mosfet Static  $R_{dson}$  at 650 V/ 1A versus time

It was mentioned earlier that a sweep will be performed on the device at various temperatures then a steady state test will be carried out. The results from the  $R_{dson}$  sweep test is shown in Fig. 4.5. It can be seen that a 7 ohm on resistance can be seen using the device at hand. This will result in very significant power losses at such elevated temperatures. The steady state tests results of Fig. 4.6 demonstrate that this was infact a

major concern, and that the device failed qualification under the test conditions described in the figure's caption.

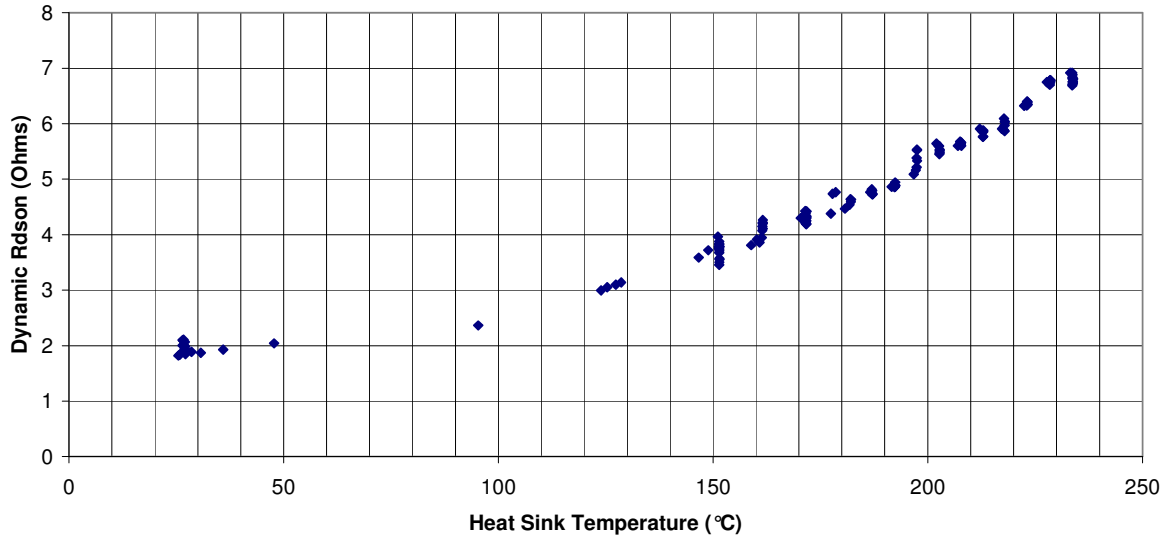


Fig. 4.7. SiC 1500 V Cascode Power Mosfet Dynamic R<sub>ds(on)</sub> 650 V/1A vs temperature

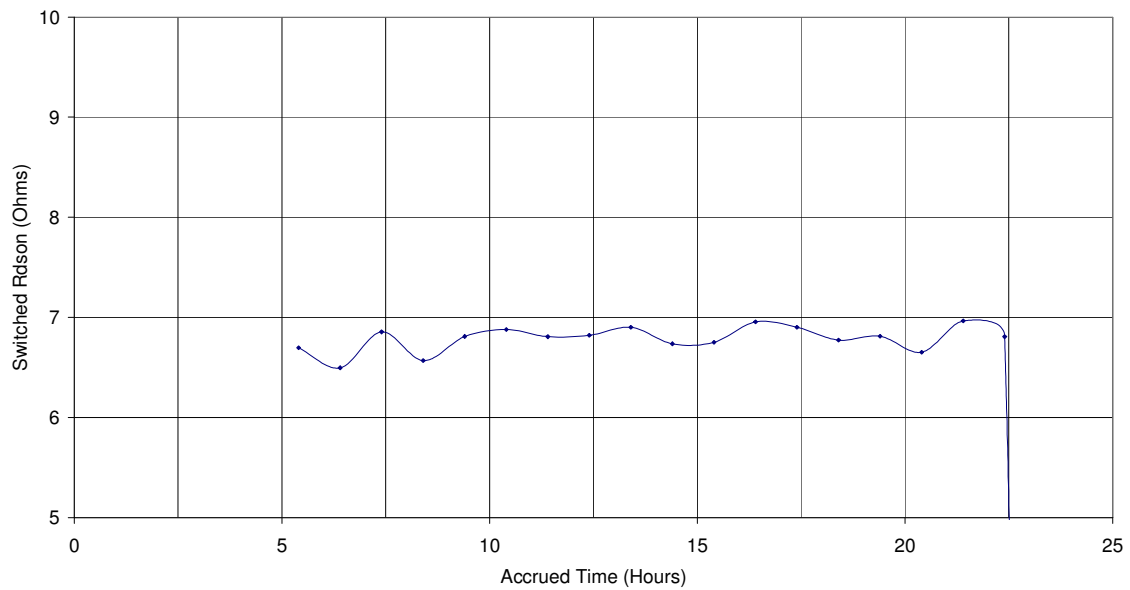


Fig. 4.8. SiC 1500 V Cascode Power Mosfet Dynamic R<sub>ds(on)</sub> 650 V/1A vs time

A similar set of tests, a sweep followed by a steady state test was conducted on another sample of the device. Fig. 4.7 verifies the results previously obtained for the on resistance, and Fig. 4.8 reiterates the conclusion reached by the previous static  $R_{\text{dson}}$  tests. The device failed and was not found to be a suitable candidate. Further testing was carried out to help reach a conclusive decision. Fig. 4.9 presents the test results for the internal body diode. It will be seen in an upcoming section of the work at hand that very similar results were exhibited by the SiC schottky diode. The performance of the diode was very favorable, even though the device testing was not so far.

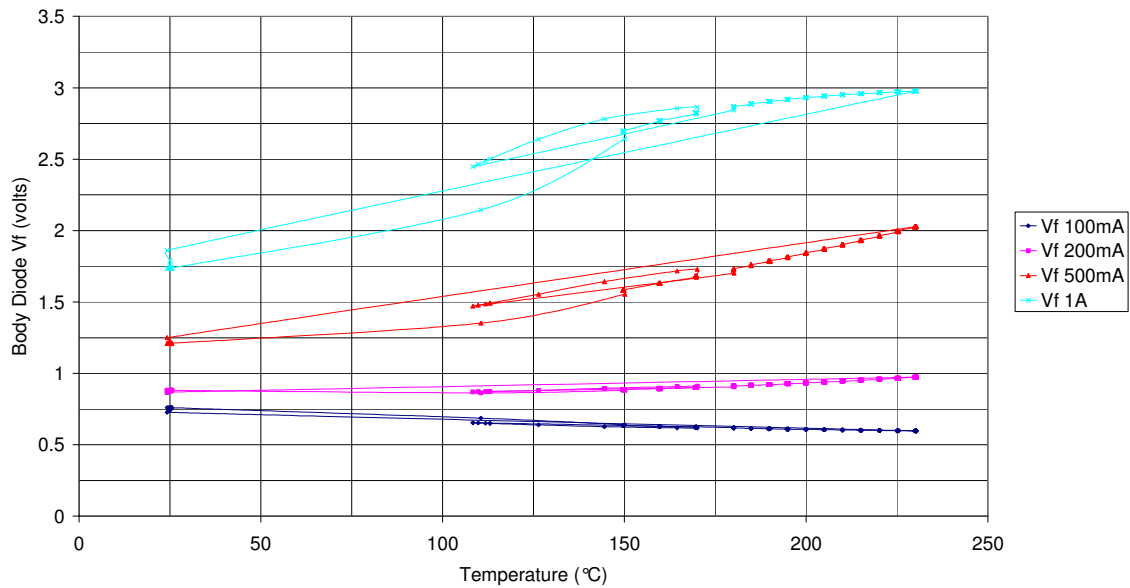


Fig. 4.9. SiC 1500 V Cascode Power Mosfet Body Diode  $V_f$  vs temperature

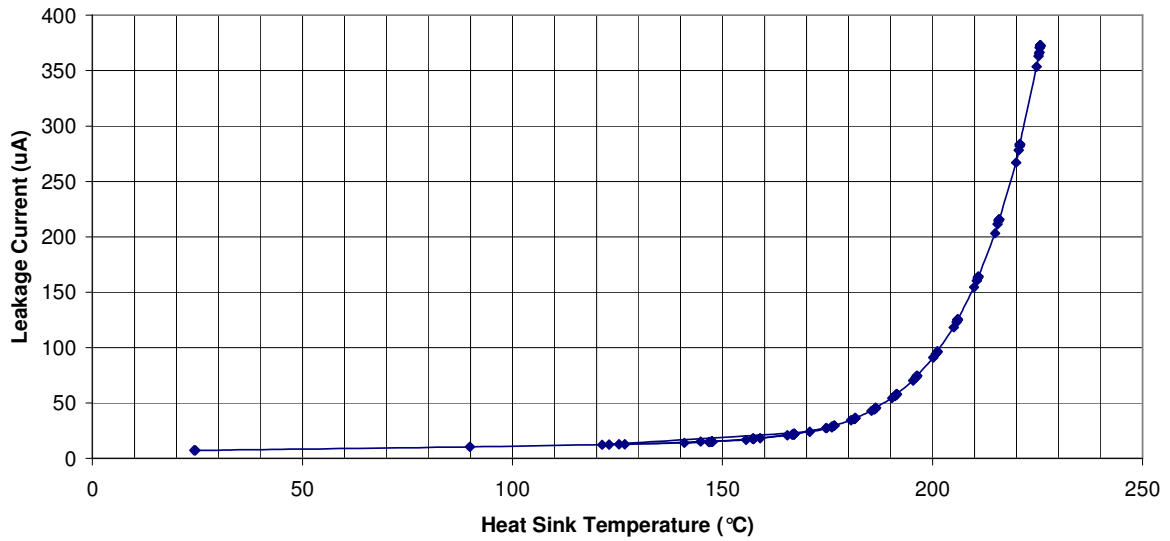


Fig. 4.10. SiC 1500 V Cascode Power Mosfet Leakage Current vs. temperature at 650 V

Static leakage tests were also conducted on the device. Compared with many of the tested devices, the device leakage is quite stable, and at first would indicate the superior behavior of the device. This test is then followed by a steady state test whose results are presented in 4.11, and similar to the previous case, the device failure was exhibited.

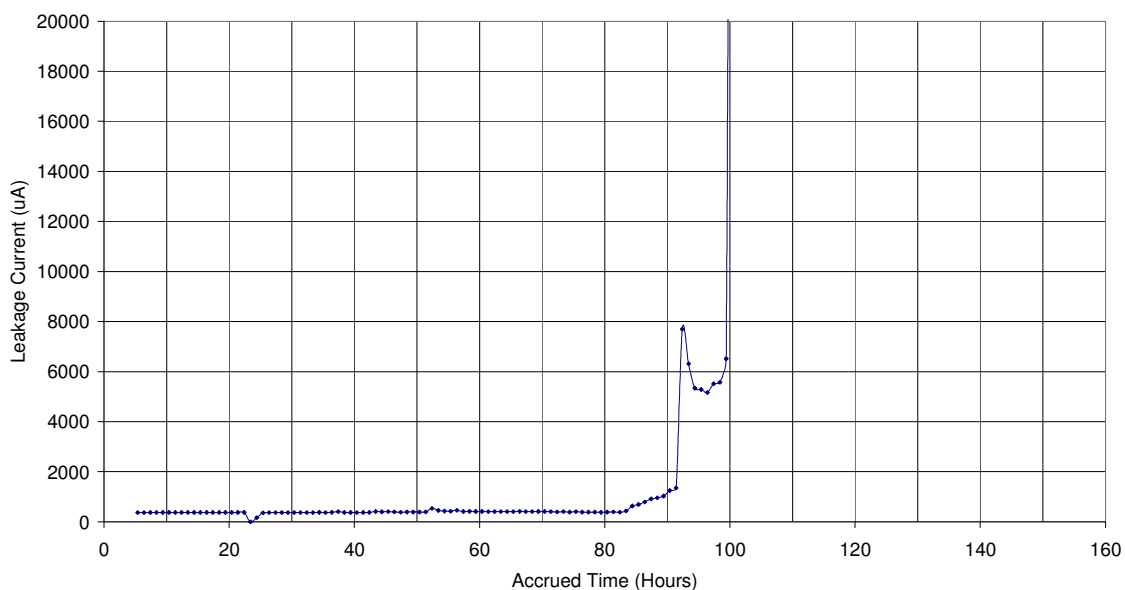


Fig. 4.11. SiC 1500 V Cascode Power Mosfet Leakage Current vs. time at 230°C

The previous results were communicated to the device manufacturer and since then, the manufacturer had been working on the improvement of the devices, and has reported favorable results. However, this was not investigated further, as the technology seemed too young for adoption and it was very difficult to get parts from other manufacturers. Very similar results were seen in other literature [19] for SiC device batches tested in the same time frame.

#### 4.2.2.3 Switching Device Test Results – Si Case

Both silicon IGBTs and Mosfets were tested for this part of the study. Although our previous discussion and literature [15][16] did indicate the favorable performance of the FETS over the IGBT devices, the presence of significant freewheeling current in a motor drive application and the absence of Mosfets with fast freewheeling diodes prompted the need to carry out the qualifications. Approximately 12 IGBT devices were tested in a

similar fashion to that described for the SiC device in the previous section. Even though devices were rated for 1000 V, most didn't survive the leakage test at elevated temperatures with full voltage impressed on them.

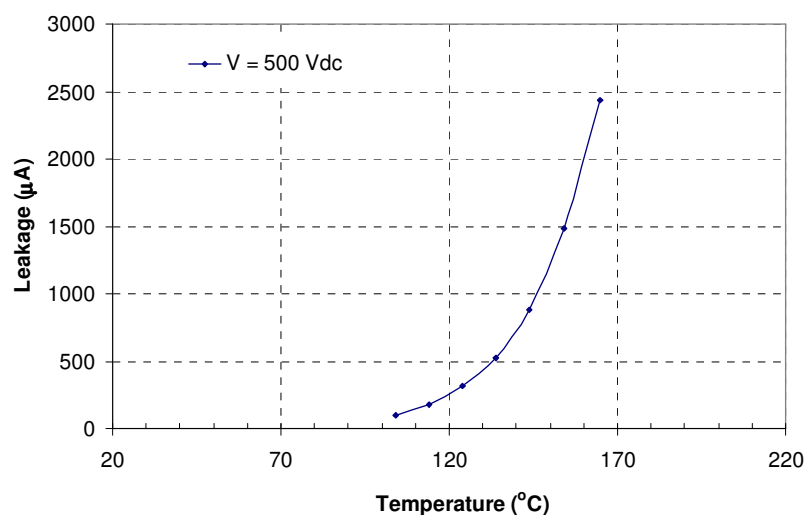


Fig. 4.12. Static leakage current test on the best performing IGBT versus temperature

Fig. 4.12 shows the leakage tests results for the best performing IGBT. A comparison with leakage tests results obtained for the SiC device shows orders of magnitude difference in performance. In fact for the same test conditions faced by the SiC device, all the tested IGBTs failed.

A similar approach to that of the IGBT results presentation will be taken for the presentation of the Mosfet test results. The testing of approximately 25 devices was carried out. The chronological order of the tests was reversed after the experience gained for the testing of the IGBT devices. Static leakage test results on the best performing device are shown in Fig. 4.13. A comparison of these test results with those

of the SiC device did provide significant anticipation and excitement about the upcoming test results.

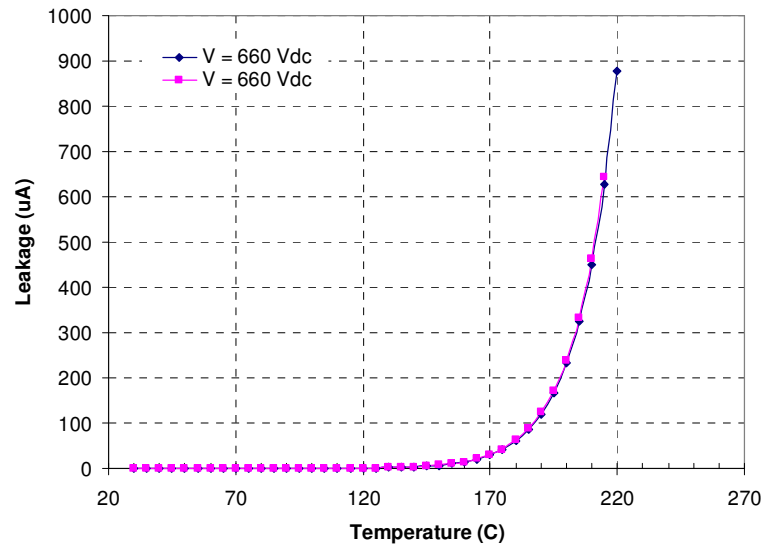


Fig. 4.13. Static leakage current test on the best performing Mosfet versus temperature

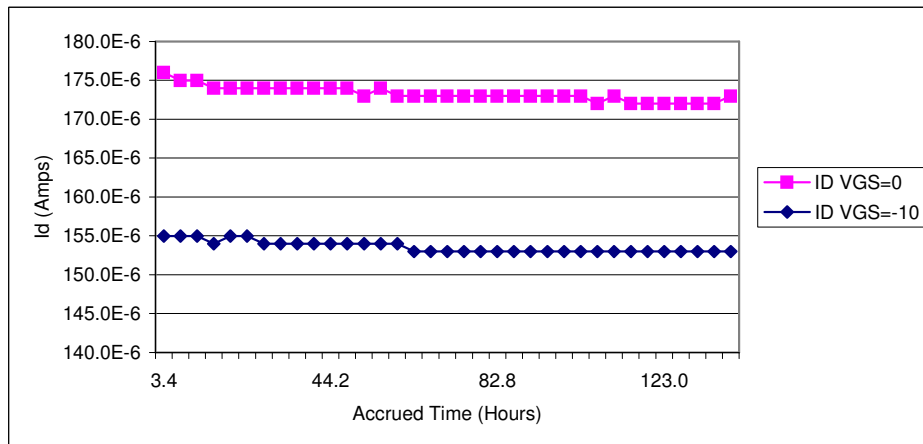


Fig. 4.14. Static leakage vs accrued time at 210°C for different  $V_{gs}$

A steady state test was then performed after the first temperature sweep as shown in Fig. 4.14. The test was conducted for different values of  $V_{gs}$ . The apparent significance of this parameter at elevated temperatures is seen. Thus, this is a gate drive design consideration that will aid in the successful operation of the device.

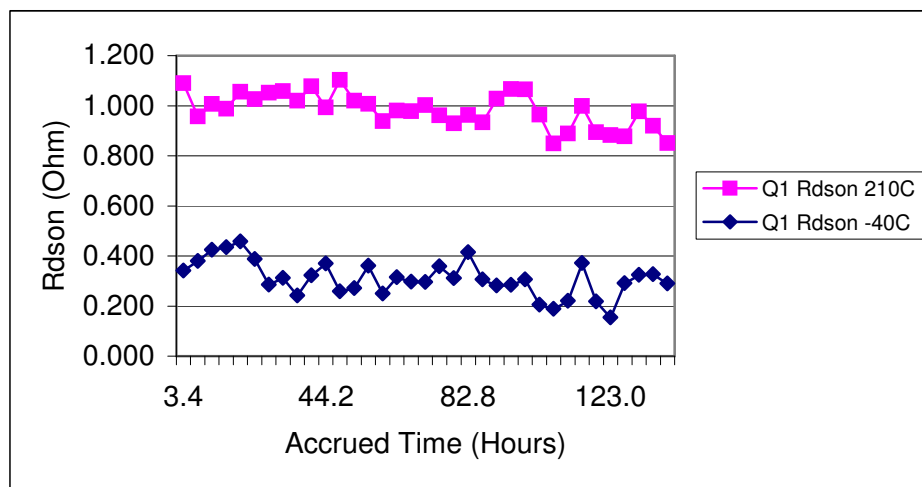


Fig. 4.15. Static  $R_{ds(on)}$  vs accrued time at different temperatures

Compared with the 7 ohm on resistance exhibited by the SiC device at temperature, Fig. 4.15 demonstrates the superior performance of the device at hand. This was seen to be a major area of concern for high current applications that are targeted by this study. After the validation of the test results performed on the current Mosfet using several samples of the device. It was concluded that this would be the most suitable device for the application at hand. This confirms what literature and our previous discussion has concluded about the possible use of silicon power devices at elevated temperatures. The next task was the selection of a suitable power diode.

#### 4.2.2.4 Diode Test Results

Although the choice of a power diode may have sounded trivial from the discussions in the previous sections, however, it will become apparent why the testing of some low voltage schottky diodes was conducted. A similar approach to that used for the previous devices is taken here. The best performing schottky diode experimental results are presented in Fig. 4.16. The results for different bias voltages are provided. It can be concluded that the leakage behavior of all the silicon schottky devices tested was not acceptable.

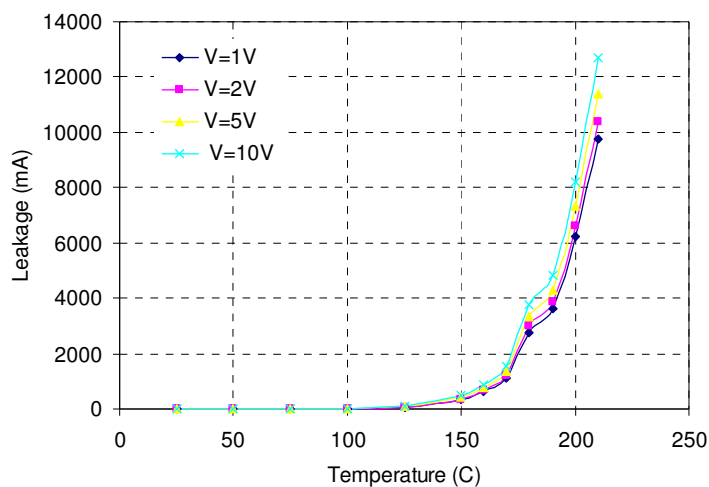


Fig. 4.16. Leakage current experimental results of the best performing schottky device

The next diode technology tested as the SiC high voltage schottky diode. The lowest voltage rated device in this family of devices is 300 V, however, for our testing, the 1200 V rated device was used for testing. Leakage current testing at full voltage on the diode revealed its superior performance across the temperature range as shown in Fig. 4.17.

The diode's forward characteristics were also tested and the results presented in Fig. 4.18 provide a smooth extension to the information available in the device datasheet. No surprising parameter changes were seen when the datasheet information was extended. It is worthy to note however, the inflection point seen in Fig. 4.18.

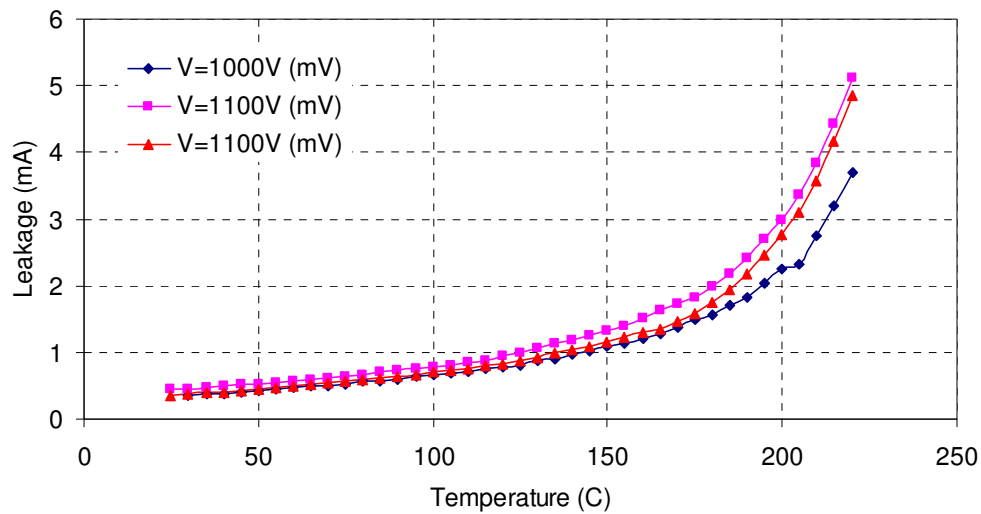


Fig. 4.17. Leakage current of the SiC diode at full voltage versus temperature

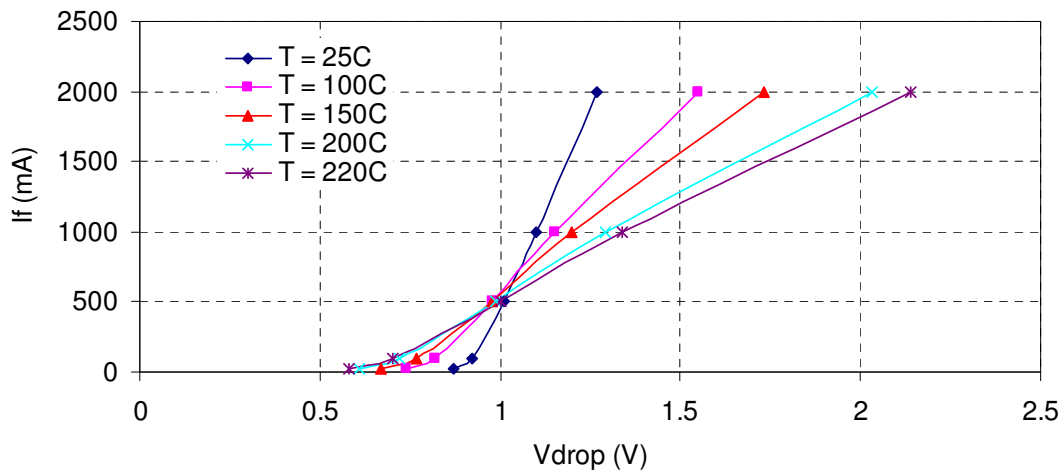


Fig. 4.18. SiC diode forward characteristics

This inflection point is perhaps even better demonstrated using Fig. 4.19. It can be seen from Fig. 4.19 that under certain values of current, the SiC diode has a negative temperature coefficient. Above that point, a positive temperature coefficient is seen. This characteristic is crucial when the devices are paralleled. The ease of paralleling Mosfets is due to their inherent positive temperature coefficient. Thus, in order to effectively utilize this characteristic, one would have to take this into consideration. Paralleling the diodes should allow each diode to carry this threshold value of current at the higher load points to prevent thermal failure of the module.

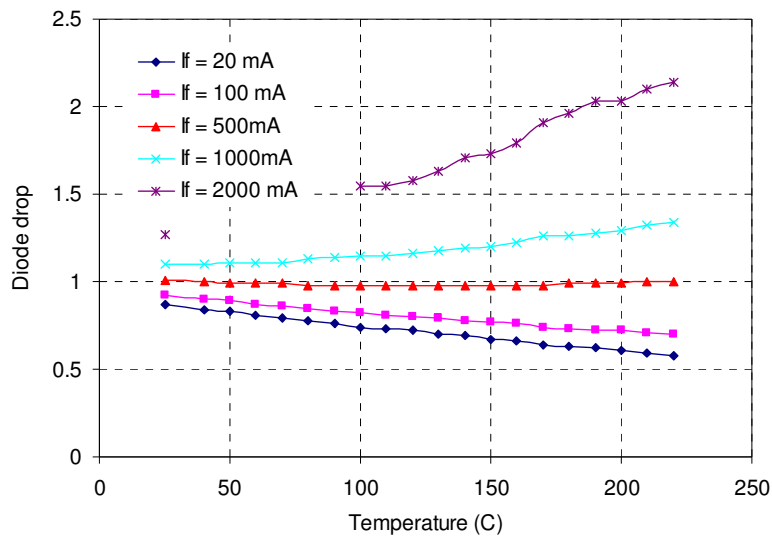


Fig. 4.19. Experimental results demonstrating the SiC diode paralleling considerations

### 4.2.3 Basic Switching Unit

The successful testing of the silicon Mosfet and the SiC diode presented in the previous sections will now have to be taken to the next step in the process of developing

compact harsh environment power electronic subsystems. These subsystems will be the enabling technology behind many motor drives and power supplies. Although several dc-dc power supplies have been designed and tested throughout this work, the discussion at hand will concentrate mainly on the motor drive application. Because of the presence of significant amount of freewheeling current in any motor drive application, the effect of the selected Mosfet's body diode was examined. This will be detailed in the next subsection. However, it was found that the chosen Mosfet has a very snappy body diode. The performance of the body diode is very poor and unacceptable in any hard switching motor drive application. Thus, the basic switching unit chosen was one common in many literature where Mosfet applications in hard switching motor drives are addressed [20]. An anti-parallel blocking is placed in series with the Mosfet channel, whereas a parallel freewheeling diode is placed across the combination. This can be seen in Fig. 4.20, where the Mosfet and its parasitic body diode are shown in a dotted box.

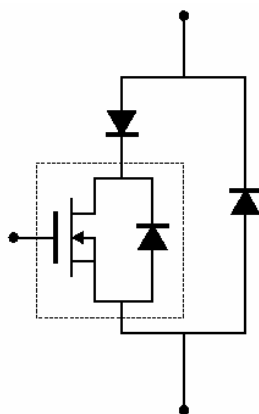


Fig. 4.20. Basic Mosfet and diode switching unit for the motor drive application

### 4.2.3.1 The Mosfet's Performance in the Basic Switching Unit

Although comprehensive testing has been carried out on the devices selected, the tests done thus far would not help quantify the system's switching losses, nor would they help in understanding what would happen when the devices are grouped together in the basic switching unit. It is the objective of this section to carry out this analysis before a complete motor drive system based on the selected devices can be design and tested successfully.

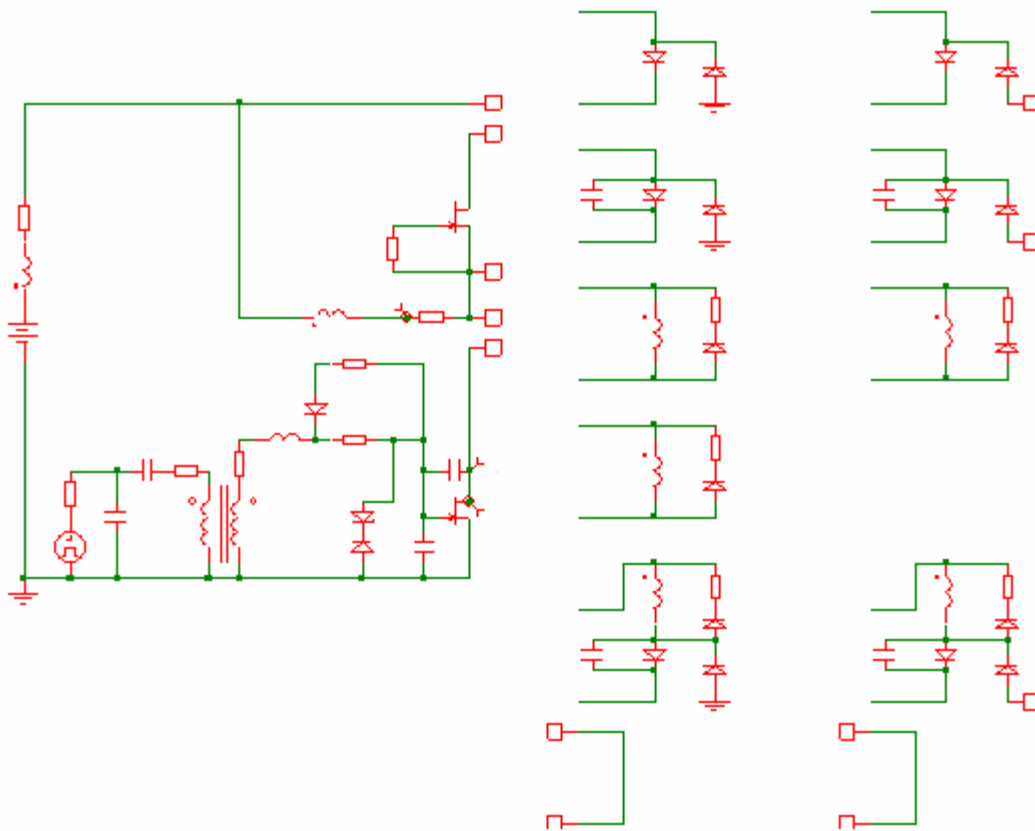


Fig. 4.21. Schematic of the experimental and simulation setups used in the Mosfet loss analysis

The schematic diagram shown in Fig. 4.21 was used to carry out a comprehensive analysis of the effect of using the selected devices in various dc-dc and dc-ac topologies.

The circuit in Fig. 4.21 was both simulated and built. Simulations with actual device parameters were used to ensure that the simulations are as close to reality as possible. Terminals A, B, C, D and E of the circuit could be connected to any of the subcircuits shown on the right in Fig. 4.21. The logic behind each of the subcircuits shown will become clear in the next section and this section will only be presenting the results and verifying the simulation results with those from the experimental setup. To prevent duplicating the labels of the waveforms, the same colors were used throughout the presented loss analysis. Table 4.1 shows the legend that can be used with all the simulation and experimental results.

Table 4.1. Waveforms legend for all figures of this section

Simulation	Scope	Signal Description	
Red	Red	$V_{ds}$ of bottom FET	
Blue	Blue	$I_{FET}$ of bottom FET	
X	Green	X	$I_{LOAD}$
Brown	Light Green	Power in bottom FET	

The testing and simulation conditions were made identical in all the following cases in order to help verify the simulation environment. As previously mentioned, the choice of subcircuit to add to the experimental and simulation setup was based on information that will be presented in the next section. Thus, in this section the testing conditions and the main observations from the simulation and experimental results will be provided. In the next section, the choice of some of the subcircuits will be explained and possible reference to the results of this section will be needed.

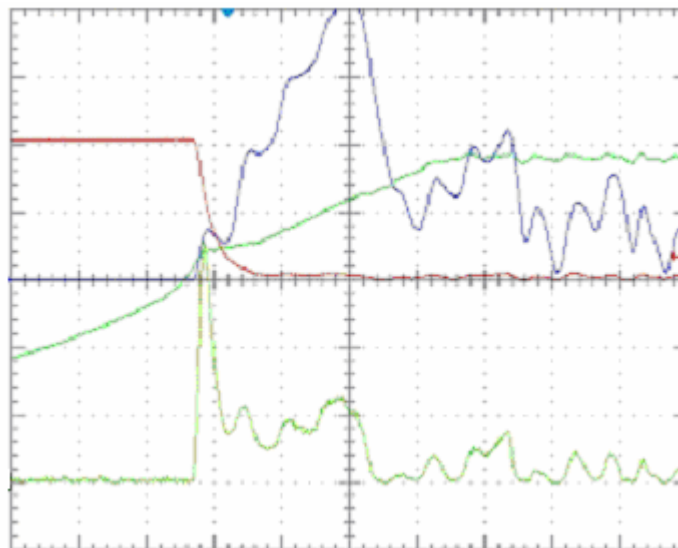


Fig. 4.22. Experimental results with FETs alone

The experimental results of Fig. 4.22, and the simulation results of Fig. 4.23 depict the performance of the FETs alone. No external subcircuits were connected in this case, short circuits were placed instead. The input dc link voltage in this case was 40 V. The experimental results and the simulations both show a current spike of approximately 4 A after the fall of  $V_{ds}$ . Some ripple is also apparent after the initial current spike. A peak power loss of about 20 W is seen. The power plateaus at the peak current then some ripple in power is observed. It can be seen from the results that the performance of the devices at hand in this circuit topology is very unacceptable. This verifies that the hardswitching operation of the devices at hand is not a good design alternative.

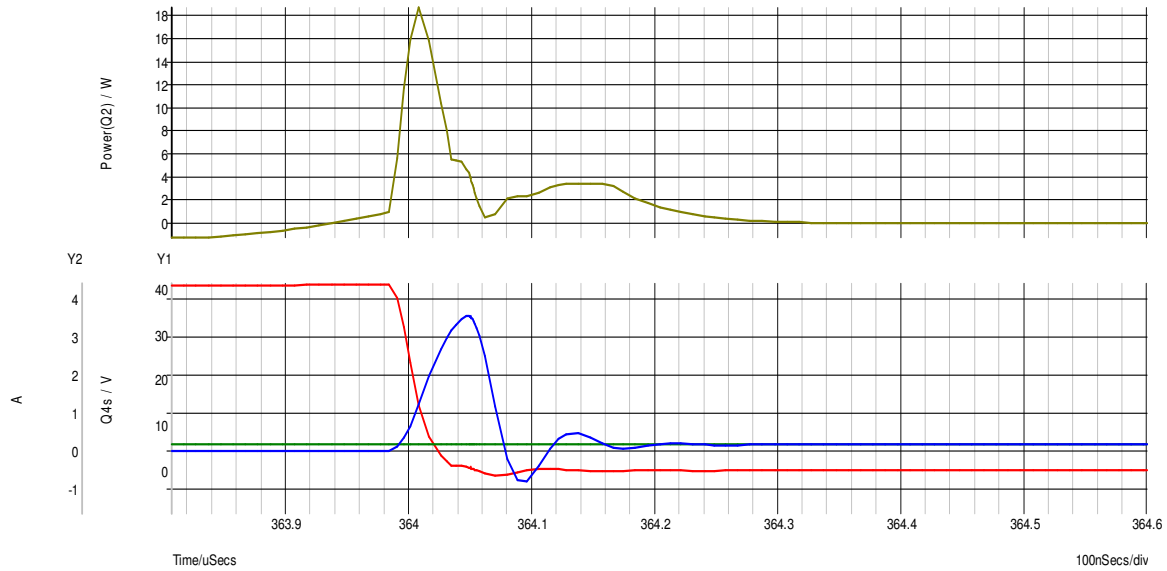


Fig. 4.23. Simulation results with FETs alone

It should be noted here that the reader needs to refer to the current, voltage and power scales on the left hand side of the simulation results. A comparison of the values with those from the experimental will show very close agreement. This is noted here the maximum values of the y-axis do change between the figures to adapt themselves to the values of the simulation.

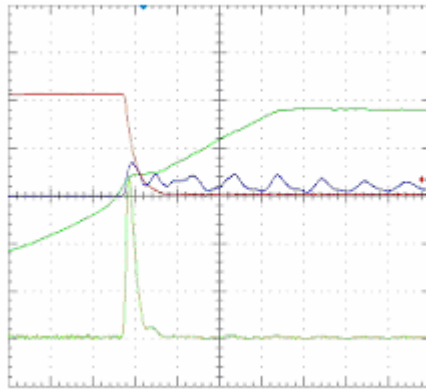


Fig. 4.24. Experimental results with the blocking and parallel diodes

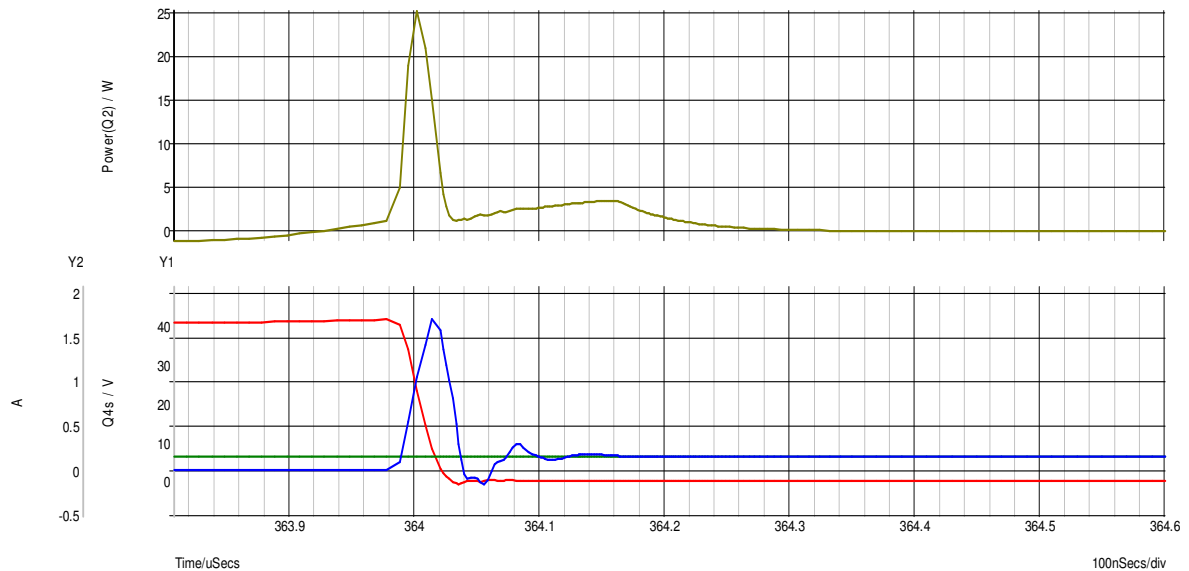


Fig. 4.25. Simulation results with the blocking and parallel diodes

The experimental and simulation results of Figs. 4.24 and 4.25 are for the case when the two diodes of the basic switching unit are used. A smaller current spike at turn-on of 0.8-1.5 A is seen. Less current ripple than the FET alone case is seen, although parasitics add some in the experimental results. A peak power of about 20 W is seen

which is like the FET only case. Significantly less power loss occurs after the peak current and bus voltage is also 40 V.

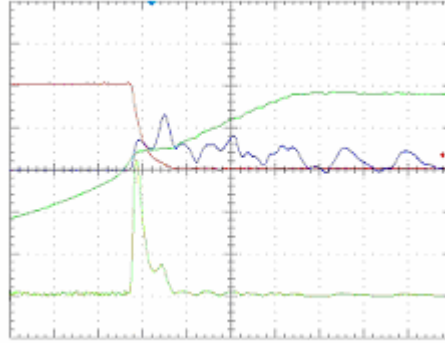


Fig. 4.26. Experimental results with the blocking diode across a capacitor and the parallel diode

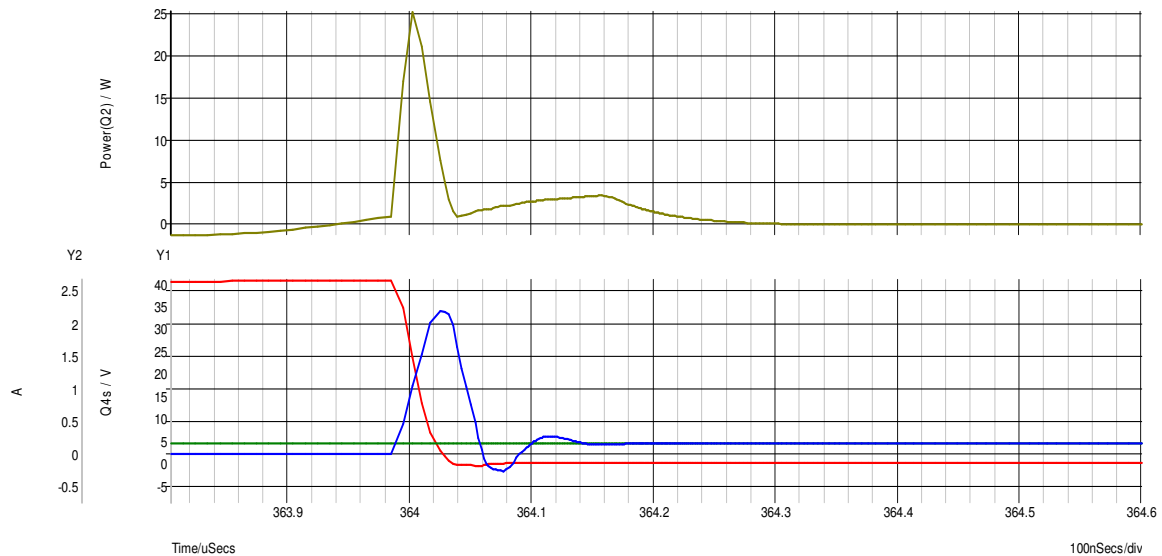


Fig. 4.27. Simulation results with the blocking diode across a capacitor and the parallel diode

The experimental and simulation results of Figs. 4.26 and 4.27 are for the case when an extra capacitor is placed across the antiparallel blocking diode. The results are almost identical to those with the diodes only. A peak power of 20 W is seen. Extra ripple

current is however seen in the experimental results which does affect the power loss.

The bus voltage is also 40 V in this case.

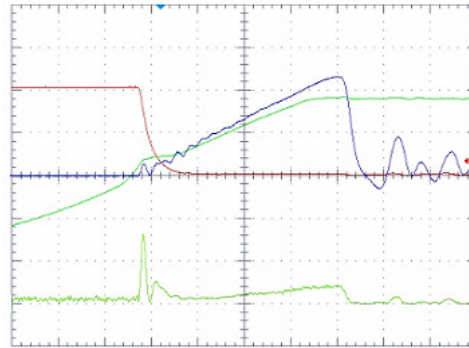


Fig. 4.28. Experimental results with an inductive turn on snubber

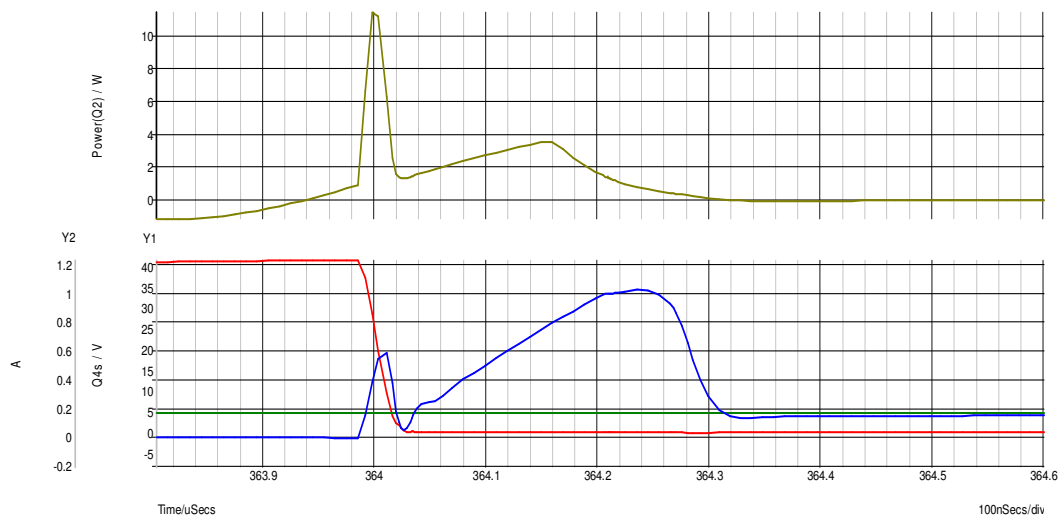


Fig. 4.29. Simulation results with an inductive turn on snubber

The experimental and simulation results of Figs. 4.28 and 4.29 are for the case when an inductive turn on snubber is added to the circuit. A 0.5 A current spike is observed when  $V_{ds}$  drops. A large delayed current spike well after  $V_{ds}$  is seen. Peak power is down to 10 W instead of 20 W. The power loss peaks, drops, then rises slightly with the

delayed current spike. A 3.4 $\mu$ H snubber inductance was used here, and the bus voltage was also kept at 40 V.

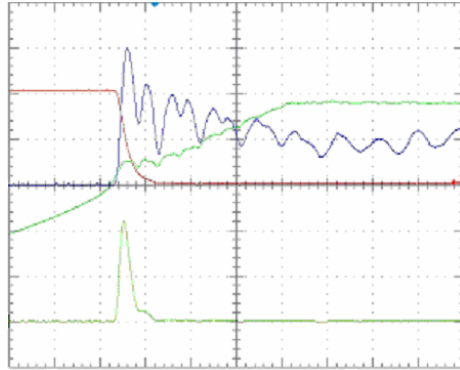


Fig. 4.30. Experimental results with diodes but at a higher voltage

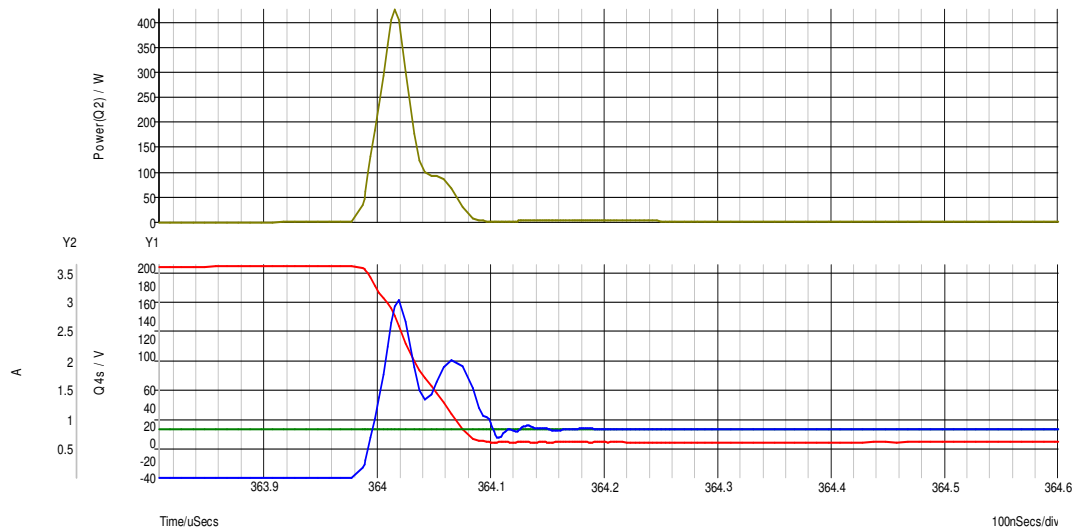


Fig. 4.31. Simulation results with diodes but at a higher voltage

The experimental and simulation results of Figs. 4.30 and 4.31 are for the case when only the two diodes of the basic switching unit are present. In this case, however, a bus voltage of 200 V was used to test the possibility of using the configuration at higher

voltages. Here a peak power loss of 300 - 400 W is observed. The power plateaus after the initial current spike until  $V_{ds}$  drops.

#### **4.2.3.2 Addressing the Challenges and Failure Mode**

After the comprehensive testing carried out on the individual switching devices, and then on the basic switching unit, a complete three phase permanent magnet synchronous machine motor drive was built. However, it was clearly obvious that there is a failure mode of significant importance that was not revealed by the loss analysis of the devices in the previous sections. This became apparent when the high voltage SiC diodes used in the anti parallel blocking mode in the basic switching unit started failing. Theoretically, these devices should have a very low voltage drop across them. When the Mosfet is on, the voltage across the devices should correspond to the forward drop seen by the current flowing in the device, which is a few volts. When the switch is off, the input bus voltage should be seen across the Mosfet terminals. This is what can be understood from the topology and what would be seen using most simulations of such a topology using ideal components.

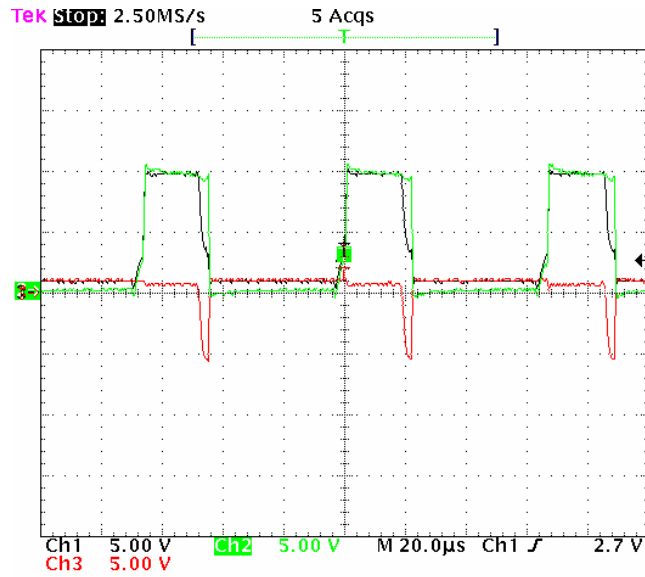


Fig. 4.32. Experimental results of switch  $V_{gs}$  (black) and blocking diode voltage (red)

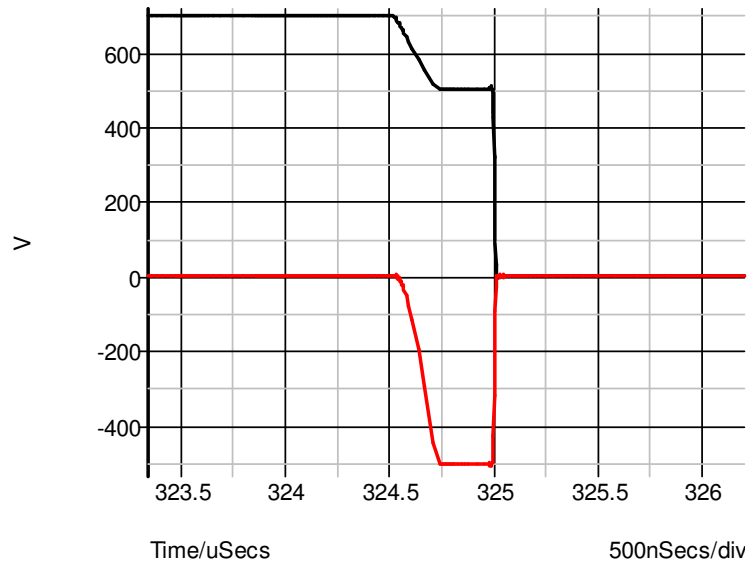


Fig. 4.33. Simulation results of switch  $V_{gs}$  (black) and blocking diode voltage (red)

Figs. 4.32 and 4.33 however, reveal a different behavior. This behavior was responsible for the many failures exhibited by the converter when running in a dc-ac

configuration. Experimental results at a reduced voltage are shown in Fig. 4.32 and simulation results at a higher voltage are shown in Fig. 4.33. The red traces in both figures are the voltage across the blocking diode and the black trace is the voltage across the accompanying switching device. Thus it became clear that the voltage across the anti parallel blocking diode is no longer a low voltage. Other diodes were tested in place of the SiC schottky and the behavior was different. This prompted an investigation into an understanding of this phenomenon. Because we have verified the validity our simulation engine and models using the previous loss analysis and the presence of the blocking diode overvoltage in this section, simulations will be used to examine this phenomenon further. Fig. 4.33 shows that this phenomenon occurs during the deadtime placed between the switches in a phase leg in one half cycle of the current. Fig. 4.34 shows the current flow in the components of the basic switching unit. This will help explain the flow of current and demonstrate why it was mentioned that this phenomenon occurs during the deadtime. The experimental setup used is a phase leg of a six switch motor drive or dc-ac inverter. The current at the anode of the bottom switch unit is the green trace, the blue trace is the current at the anode of the anti parallel diode of the top switching unit, and the red trace is the current into the parallel diode of the top switching unit. Load current flows through the bottom switch (green) when it is on. At turn off, free wheeling current needs to flow in the circuit, and although the parallel diode is placed in the circuit for that purpose, the nature of the components is seen to have a significant effect on this. The negative value of the blue trace indicates that the parasitic body diode in the Mosfet is actually conducting for a significant portion of the deadtime. It should be noted here that a significant amount of voltage is present across the blocking

diode. The reason for the presence of this voltage will be presented in an upcoming discussion.

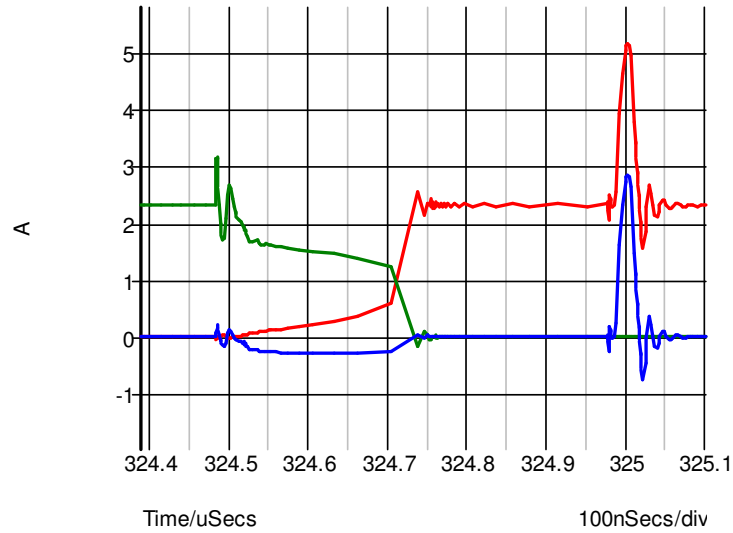


Fig. 4.34. Current flow in bottom fet (green) top fet (blue) top parallel diode (red)

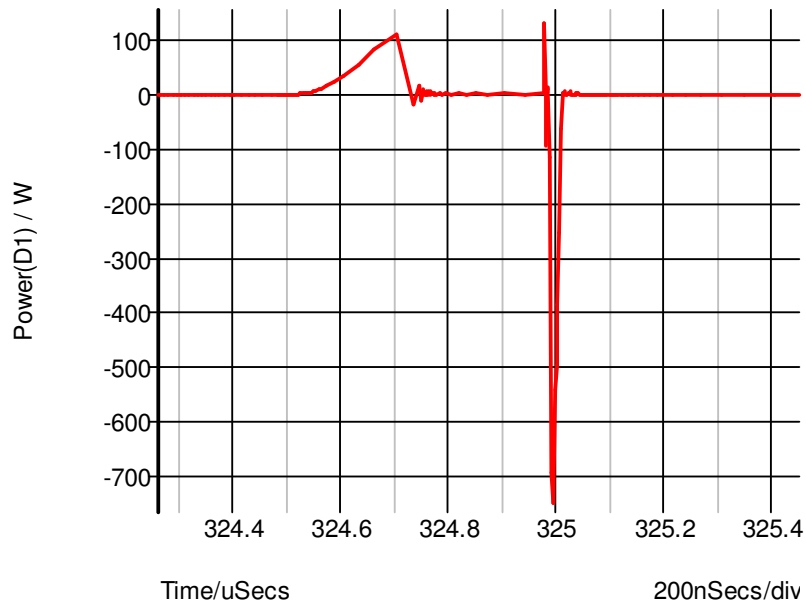


Fig. 4.35. Power loss in antiparallel blocking diode

Thus, with a significant amount of voltage present across the blocking diode, and the current seen flowing in the parasitic body diode during the deadtime until the diode's junction is charged and ready for blocking the voltage, a significant amount of power loss can be expected in this diode. The instantaneous power loss of the anti parallel blocking diode is seen from the simulation results of Fig. 4.35. This phenomenon was a significant drawback at this time, and solution was needed to enable the proper operation of the converters.

#### 4.2.3.2.1 Failure Mode Equivalent Circuits

Many attempts to understand the phenomenon and hand were not successful. Partial success was seen by a significant increase in gate resistances. However, the increase of this parameter caused a significant increase in the Mosfet loss, which was very undesirable. In addition it put a limit on the switching frequency that was not acceptable. For the half bridge dc-ac inverter case, it was seen that this failure mode occurs during the deadtime of the negative half cycle for the top switching element and the opposite half cycle for the bottom switch.

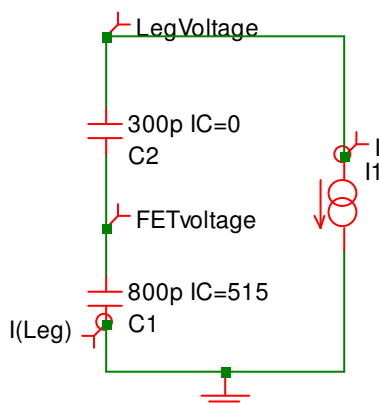


Fig. 4.36. Simplified equivalent circuit of failure mode

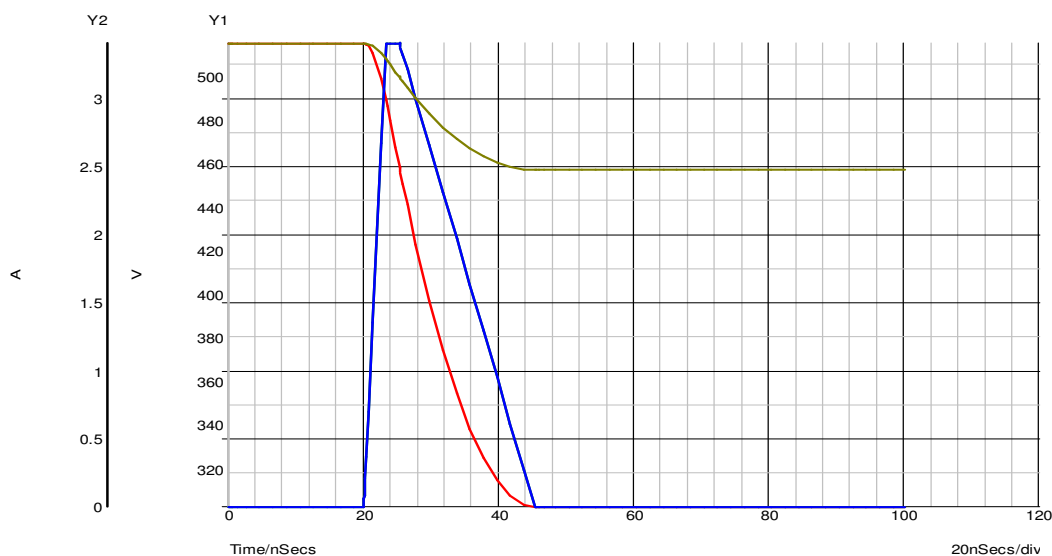


Fig. 4.37.  $I_{leg}$  (blue) and leg voltage with low (brown) and high values (red) for the diode capacitance

A simplified equivalent circuit based on one understanding of the failure mode at hand is shown in Fig. 4.36. The corresponding simulation results are then shown in Fig. 4.37. The equivalent circuit was derived from an understanding of the equivalent circuits of a mosfet and diode. The equivalent circuits of both devices suggest that each of the devices has an output capacitance. These output capacitances when combined in the circuit topology of the basic switching unit and under the specific current flow conditions seen by the switching unit will act as a capacitive divider for the input current. The value of these output capacitances for the selected devices is orders of magnitude different. From (4.2) it can be seen that current flow into this capacitive divider will cause a much faster build up of voltage across the small capacitance. The ratio of the output capacitances is approximately 50 : 1 for the selected devices. Thus, this would explain the unexpected voltage across the blocking diode during the deadtime of one half cycle. The red and brown traces in Fig. 4.37 show what happens to the

voltage across the blocking diode as the capacitor ratios are changed from 50:1 to 3:1. The blue trace resembles the current in the body diode of the Mosfet.

$$V_c = \frac{1}{C} \int i_c dt \quad (4.2)$$

Although the simple equivalent circuit of Fig. 4.36 sets the base for the understanding of the failure mode. A more detailed equivalent circuit was derived as shown in Fig. 4.38. The corresponding simulation results are seen in Fig. 4.39. This equivalent circuit demonstrates the pickup of the current by the parallel diode after the blocking diode's output capacitance is charged. The green trace resembles the Mosfet's body diode current, and the blue trace resembles the parallel diode current. The red and light blue traces are the voltages across the top switch at two different ratios of the capacitive divider. The similarity between these results and those previously presented confirm the current understanding of the failure mode at hand. The next section will present a simple attempt to mitigate the problem at hand, and will demonstrate the effectiveness of the technique.

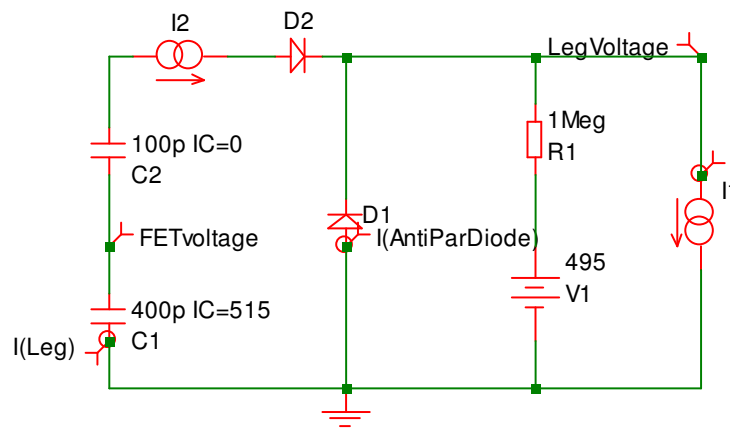


Fig. 4.38. More realistic equivalent circuit of failure mode

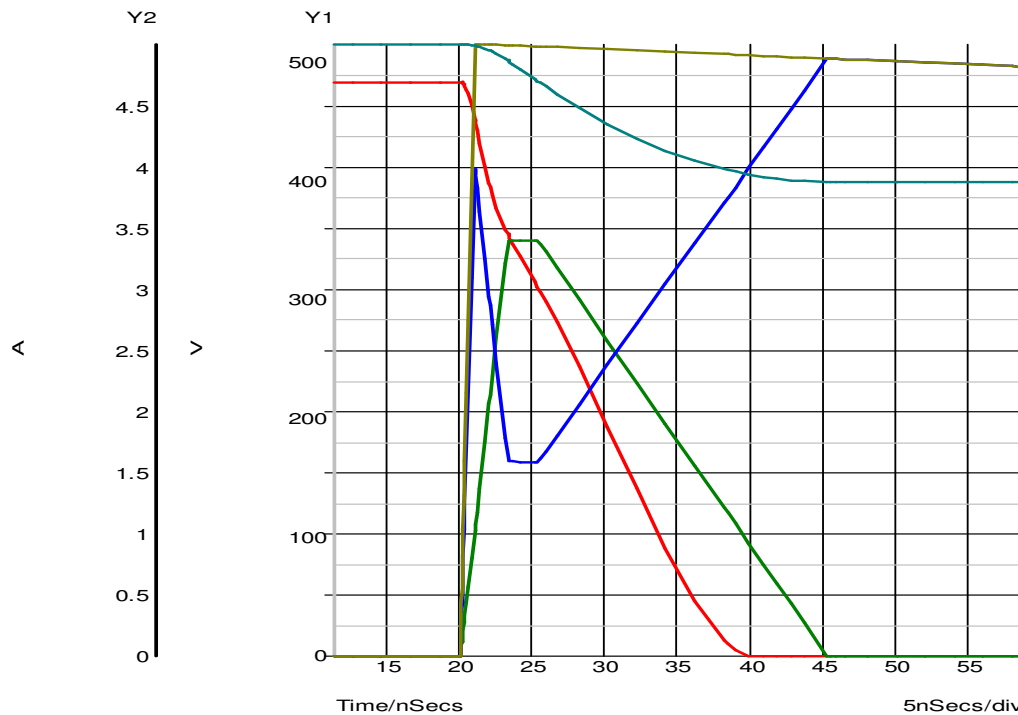


Fig. 4.39. I(leg) (green), I (diode) (blue), FET Voltage (light blue – small cap, red – big cap), leg voltage (light brown)

#### 4.2.3.2.2 Passive Mitigation of the Failure Mode

The previous sections have presented the symptoms of the failure mode and companion equivalent circuits to explain them. In this section, a simple passive technique to mitigate the failure mode will be presented. The successful use of the technique has proved invaluable for the development at hand. The success of the development was hinged upon finding a solution to this failure mode.

It was shown that the capacitive divider seen by the current coming into the basic switching unit was the reason for the unexpected voltage across the blocking diode. A simple solution to this problem is placing a small capacitor in parallel with the blocking diode to prevent this from occurring. This capacitor will alter the capacitive divider

when needed most. The voltage across the switching device and the corresponding blocking diode are shown in Fig. 4.40. Comparing this with the results shown in Fig. 4.33 shows the significant reduction in voltage across the blocking diode.

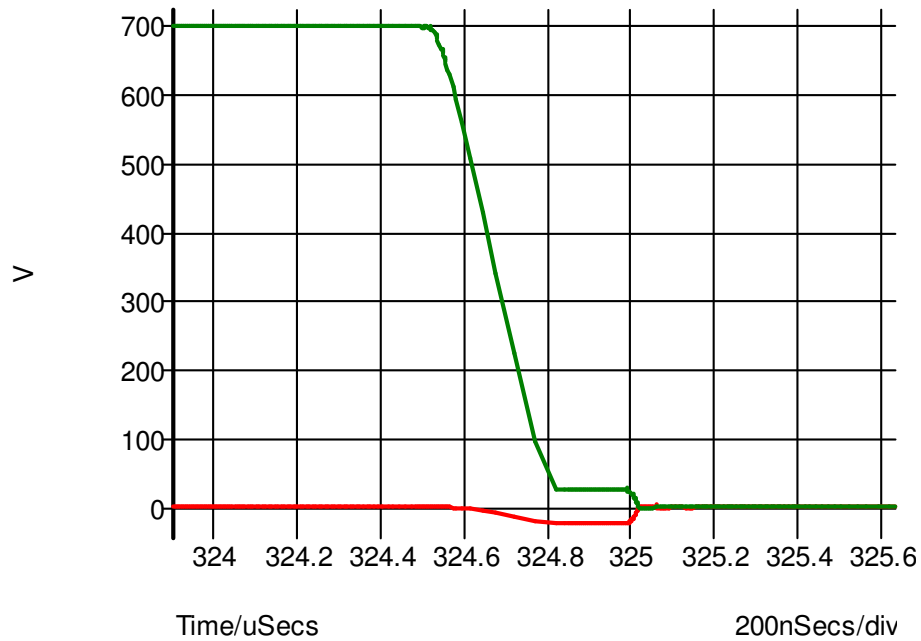


Fig. 4.40. Simulation results of switch  $V_{gs}$  (green) and blocking diode voltage (red) with external capacitor

The corresponding current waveforms are shown in Fig. 4.41. A comparison with Fig. 4.34 shows that the Mosfet's parasitic body diode does not conduct any noticeable current in this case. This will have a direct effect on the blocking diode's power loss as seen by the green trace of Fig. 4.42. The power loss in the device in the case with of no external capacitance is also shown in Fig. 4.42 for comparison.

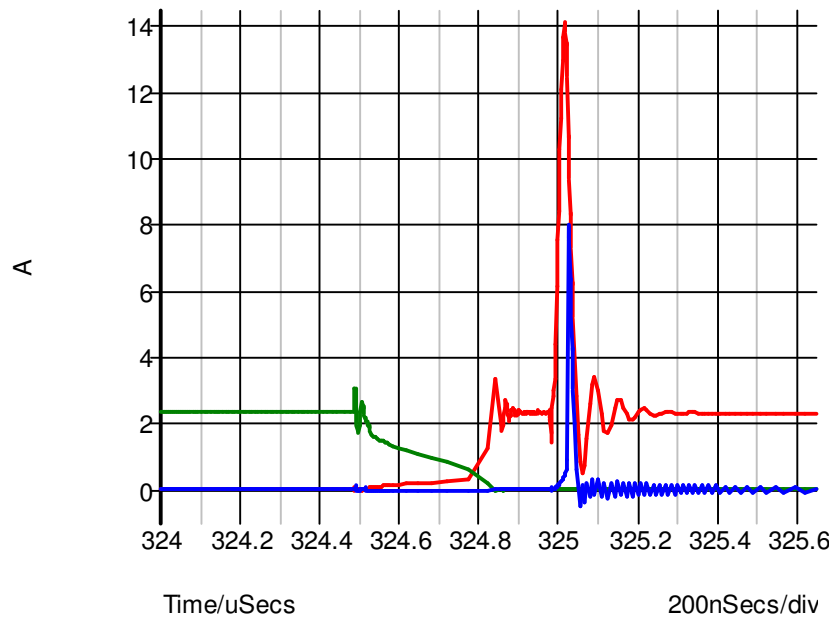


Fig. 4.41. Current flow in bottom fet (green) top fet (blue) top parallel diode (red)

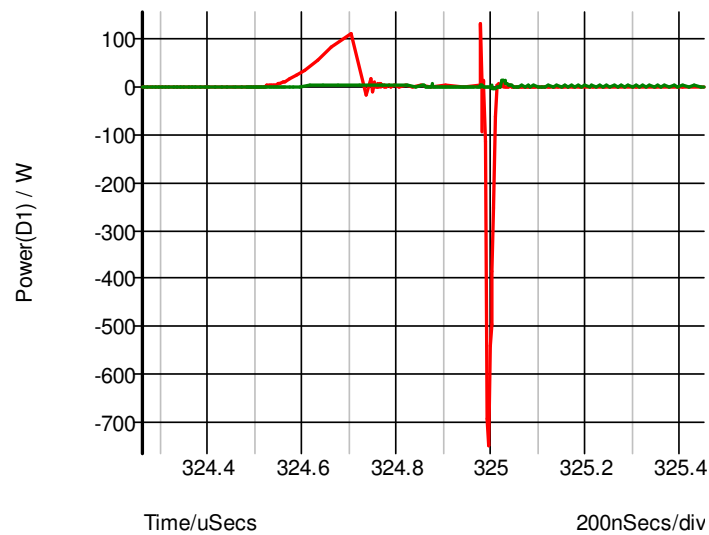


Fig. 4.42. Power loss in the blocking diode without the parallel capacitor (red) with it (green)

It is probably clear now why the specific subcircuit blocks used for simulation and experimented with during the calculation of the Mosfet losses were chosen. It was seen

from the analysis of the results in Figs. 4.24 and 4.26 that the addition of the capacitor does not add any significant amount of loss to the Mosfet. The simple passive mitigation used enabled the successful operation of the selected devices and wasn't seen to add any significant drawback. This was illustrated using comprehensive experimental and simulation results.

### 4.3 Design and Testing of a Custom High Temperature Power Module

The device selection and quantification of the device losses through experiments and simulation was presented in the previous sections. It was also seen through the analysis of the losses that derated operation of the devices would be needed to maintain the thermal integrity of the device. The actual motor drive application which is the target of this study, will however, require a significantly higher current and power value than what a single device can offer. Thus, in this section a discussion of the approach used to design and test a custom power module will be presented.

Table 4.2. Main range of materials used in the module construction with some thermal properties

Materials	Density Kg/m <sup>3</sup>	Specific Heat J/Kg-K	Thermal Conductivity W/m-K
Silicon	2381	700	150
Silicon Carbide	3250	750	250
Aluminium Nitride	3260	740	170
AlSiC	3000	850	180
Thermal Grease	2100	1675	0.8
Kovar	8300	439	17.3
Beryllium Copper	8250	419	106.3
Alumina	3726	880	25
Polyimide	1420	1090	0.2
Bakelite	1650	1235	0.15
Aluminium	2719	870	202.4
Steel	8030	502.48	16.27
Air	1.255	1006.43	0.0242
Pb50Sn50 Solder	8890	213	46

The design of the power module to be discussed in this section will use the tested components and the results of the previous sections to guarantee a successful implementation. Many of the techniques used in the design of the power module were derived from [21]. In [21] a comprehensive study of the design of integrated power modules for elevated temperature has been presented. The main materials used throughout the design are shown in Table 4.2 along with some of the significant thermal properties. The details of the construction and the materials used and the techniques implemented in the work at hand will not be detailed in this dissertation as many proprietary techniques were involved. However, the approach used in the design and the tests carried out will be presented.

#### **4.3.1 Simulation Results**

It was shown in [21] that the successful design of a power module will rely on extensive thermal simulations which are then to be verified experimentally. This was the approach used in the work at hand. Fluent was also used as was the case for the previous study on viscous losses. Although analytical calculations were a possibility, the effect of proximity of the devices and their different arrangement would have been very difficult to estimate analytically. The input to the thermal simulation was the die size and the expected electrical losses in each die, and the material properties to be used in the module. The arrangement of devices was guided by many packaging constraints, but was flexible to a certain degree that recommendations from the thermal design were taken into consideration.

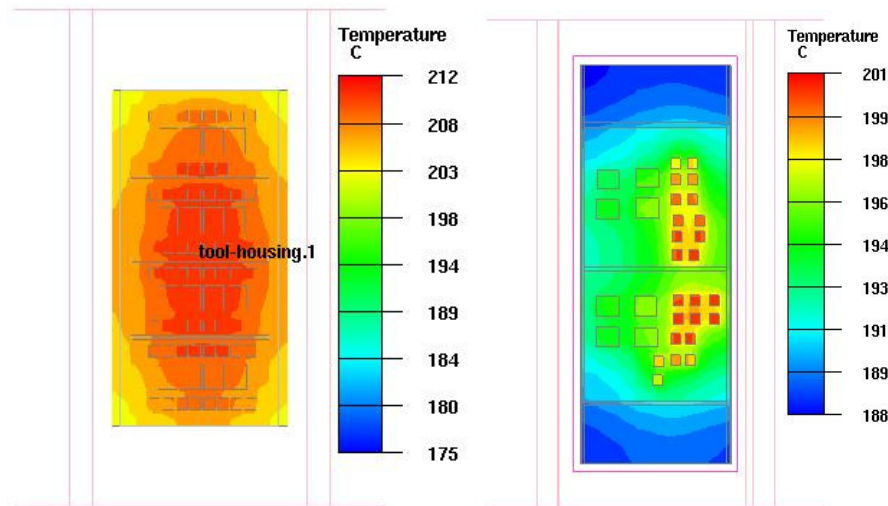


Fig. 4.43. Thermal simulation results for full multilevel inverter phase leg in one leg (left) and half (right)

The analysis of losses presented in the previous sections and past experience have shown that a  $25^{\circ}\text{C}$  temperature rise would be the acceptable limit of temperature rise at full power delivered from the module. The topology and the rated power dictate the number of die in the module. It will be seen in the next chapter that the objective is to build a multilevel inverter. Thus, four basic switching units are needed per phase leg. This can be done using all the devices of a phase leg in one module, or each phase leg can be composed of two or even four modules if necessary. The case of four modules would mean that each basic switching unit is placed in one module. With two power modules, two switching units are placed in each module. This decision was taken based on the simulation results of Fig. 4.43. It can be seen that with the full multilevel inverter phase leg in the module, temperature rise in excess of  $25^{\circ}\text{C}$  above and ambient of  $175^{\circ}\text{C}$  is seen. This was seen as an unacceptable risk, and the two switching units per module solution was seen as the way forward. The thermal simulation results in this case are also shown in Fig. 4.43 with a  $26^{\circ}\text{C}$  temperature rise above ambient. It is clear from Fig.

4.43 that the significant forward voltage of the SiC diodes at elevated temperature along with the small die size contribute to its higher temperature compared with the Mosfet die. It was also important that the losses of one device not affect the temperature rise of a neighboring one. Thus, placement of the devices was an iterative process, however it was still guided by the packaging needs of the application.

### 4.3.2 Experimental Results

Comprehensive analytical, electrical, thermal and mechanical experiments were carried out on the developed module to ensure its reliable operation. A half bridge dc-ac converter was designed to test the module's electrical performance. Thermal imaging was used to verify that the design criteria have been met. Mechanical integrity was also tested using MIL STD 883 E shock tests on the module.

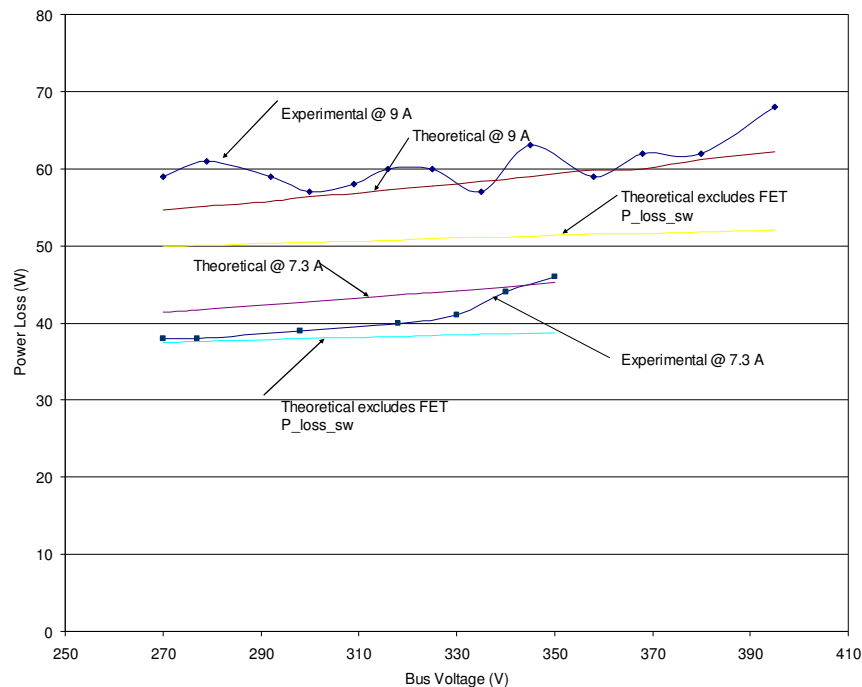


Fig. 4.44. Theoretical and experimental module losses at various values of current

Device loss models based on [22][23] were developed to estimate the efficiency of the module under full load operation. This was then compared with experimental results for different values of load current and bus voltage. It can be seen that the models provide a good estimate of the module losses under different operating conditions.

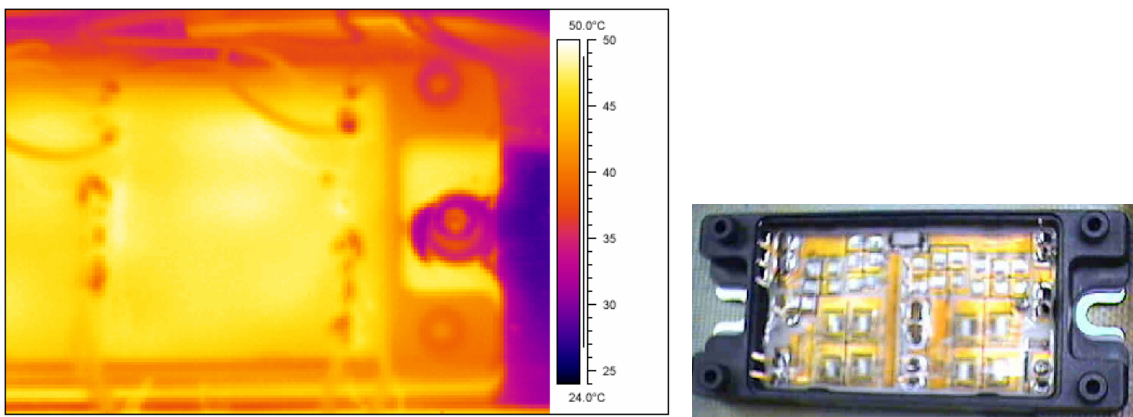


Fig. 4.45. Thermal image and the corresponding module used for the test

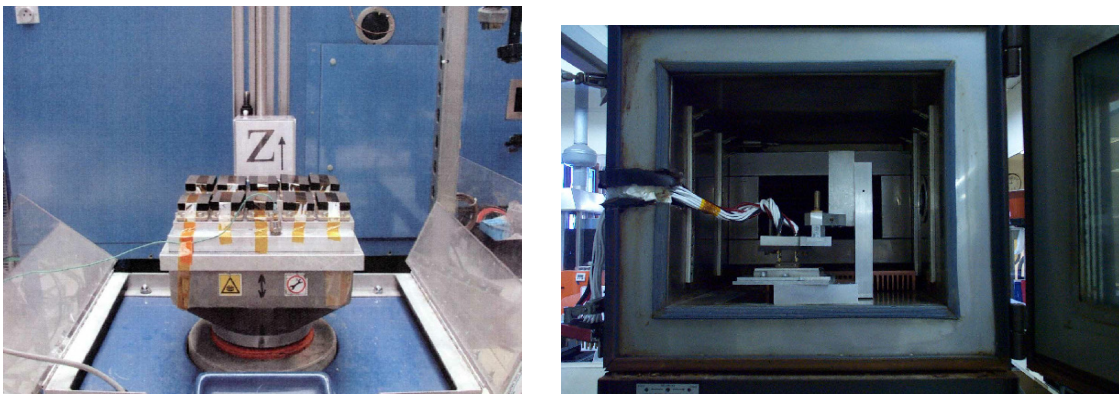


Fig. 4.46. Experimental setup used for mechanical (left) and burn in tests (right)

Thermal imaging was carried out on the module during full load operation. This was part of the experimental setup used to measure the system losses shown in Fig. 4.44. The results of the thermal imaging shown in Fig. 4.45 demonstrate that a temperature rise of 25 °C is experienced by the hottest point in the module at full load operation when the ambient temperature is 25°C. Burn in tests and mechanical integrity tests were then performed on the module. The systems used are shown in Fig. 4.46. Shock tests were conducted on all three axes. This was important to ensure the integrity of the wire bonds, and other mechanical components in the power module. The developed module successfully passed the tests and was then tested in a three phase motor drive at 230°C ambient and proved to be a success in this test as well.

#### **4.4 Conclusion**

The stringent needs of the oil well logging industry on the power electronic conversion systems used was the main driver for the work at hand. Because of the compact nature of such systems, the ability to operate without the need for active cooling is seen as a critical technology. This can only be achieved using a combination of good device selection, topology design, and material selection. The current work started by assessment of the basic device choices and their application at elevated temperature. The interaction of the selected devices in the basic switching unit is then studied and a mitigation technique for the experienced failure mode was presented. This was justified with experimental and simulation results.

To enable the operation at higher power, a custom power module is designed based on extensive thermal simulations. Simulation results corroborated by experimental results on the developed module conclude the chapter. It was shown that some silicon

devices accompanied by proper design and packaging can withstand operation at temperature upto 200°C.

**CHAPTER V**

**MULTILEVEL POWER CONVERTERS – AN ENABLING TECHNOLOGY**

**FOR HARSH ENVIRONMENT POWER CONVERSION**

**5.1 Introduction**

Long resistive cables used in the operation of remote instrumentation impose fundamental limits on the amount of power delivered and create difficulties in voltage regulation at the remote-end (voltage at the end of the cable). This type of power delivery is used in many engineering systems such as in the operation of underwater remotely-operated vehicles, in oil well logging and drilling, in mining, and in highly distributed power systems (air craft, submarines etc.). Previous research [24][25][26] has dealt with such phenomena in detail, but the objective of this section is to illustrate what impact this has on the remote end, and it can be dealt with.

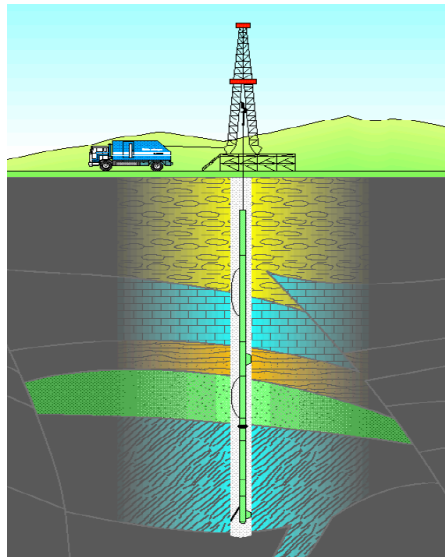


Fig. 5.1. Typical setup of a well logging application

An illustration of a typical oil well logging application is shown in Fig. 5.1. Power delivered to the downhole tools is sent from the truck, then up the rig, and down the hole. The depth of today's wells can reach 36,000 feet.

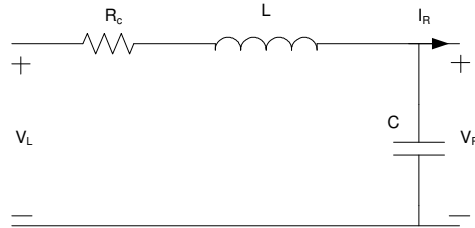


Fig. 5.2. Simplified distribution system model.

Consider the simplified model of a distributed power system shown in Fig. 5.2, with the cable used for power delivery to the remote-end represented by a lumped model with resistance  $R_c$ , inductance  $L$  and capacitance  $C$ . The power transmitted to the remote-end at steady state is given by (5.1) where  $V_L$  and  $I_L$  represent the values of the local-end voltage and current, and  $V_R$  and  $I_R$  represent the remote-end voltage and current respectively.

$$\begin{aligned}
 P_{remote} &= V_R I_R = V_L I_R - I_R^2 R_C = V_L \left( \frac{V_L - V_R}{R_C} \right) - \left( \frac{V_L - V_R}{R_C} \right)^2 R_C \\
 &= \frac{V_L^2}{4R_C} - \left( \frac{\frac{V_L}{2} - V_R}{R_C} \right)^2
 \end{aligned} \tag{5.1}$$

As can be seen from this expression, the power delivered to the remote-end is maximized when the remote end voltage is half the local-end voltage maximum. Thus,  $V_R = V_{L_{max}}/2$ , which is equivalent to a resistive load having the load-end resistance

matching the cable resistance. With this substitution, the maximum power delivered to the remote end is as shown in (5.2).

$$P_{remote\_max} = \frac{V_{L,max}^2}{4R_c} \quad (5.2)$$

Thus, it can be seen that as more power is required at the remote end, a corresponding increase in voltage is needed to enable maximum power delivery. The increased power requirements of downhole tools such as tractors and some drilling tools has thus prompted an investigation into means of accomplishing this. Based on the results from the previous chapter, there does not exist a switching device that can be produced commercially today that can withstand voltages greater than 800 V at elevated temperatures. Thus, the objective of this chapter is to demonstrate the effectiveness of the multilevel converter topologies in next generation harsh environment power conversion systems at the remote end of a dc transmission line where voltage levels beyond 1000 V are needed.

## **5.2 Multilevel Power Conversion Solutions for Compact Harsh Environments**

A need for both dc-dc and dc-ac power conversion systems exists for compact harsh environment applications. During the progress of the work at hand, both applications have been addressed and tested at elevated temperatures to determine the feasibility of their use. The neutral point clamped multilevel dc-dc converter shown in Fig. 5.3 was used for the dc-dc converter study. Fig. 5.4 shows the experimental and simulation results obtained during the progress of this development. The converter was tested with a 1 KW load at 185°C for 130 hours. Test results were very successful, and will be detailed in an upcoming work by the author. The devices tested in a previous chapter

were utilized and the efficiency of the multilevel dc-dc converter phase leg was in the 96% efficiency range (only include the phase leg not the transformer what comes after it).

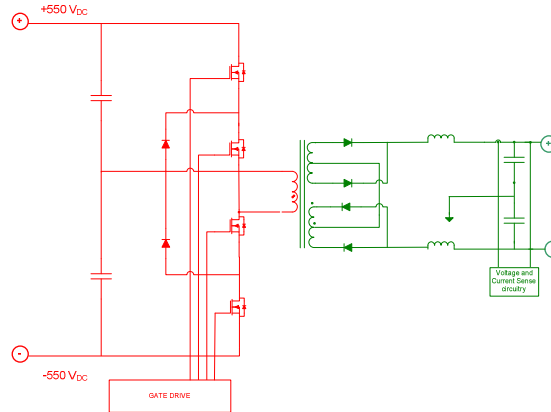


Fig. 5.3. Simplified schematic of the prototype multilevel dc-dc converter.

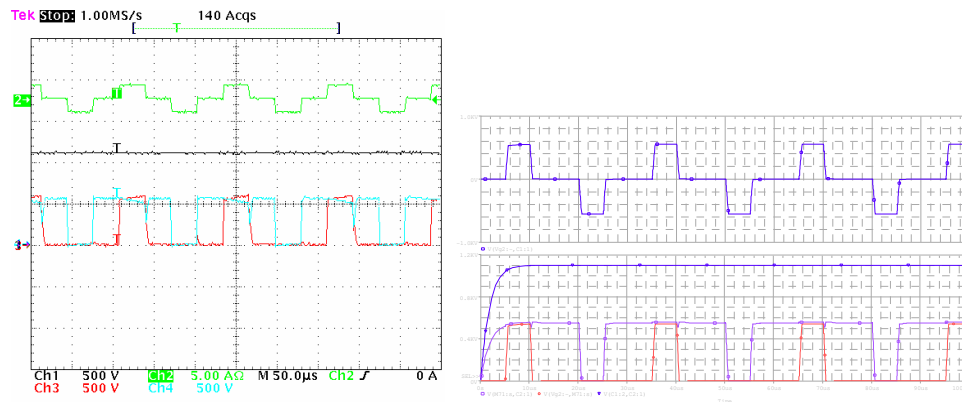
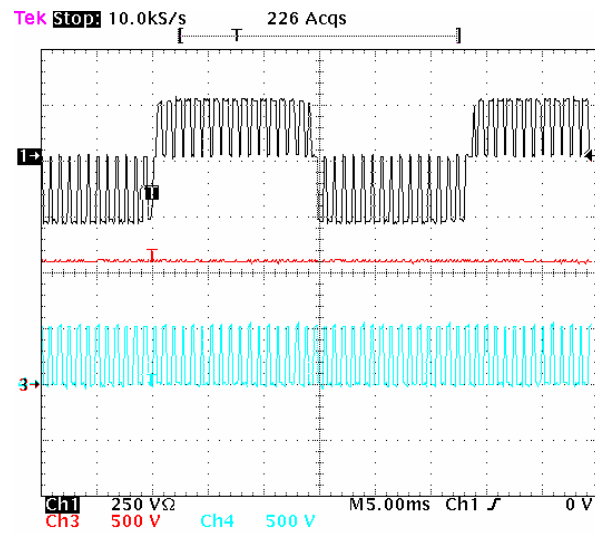


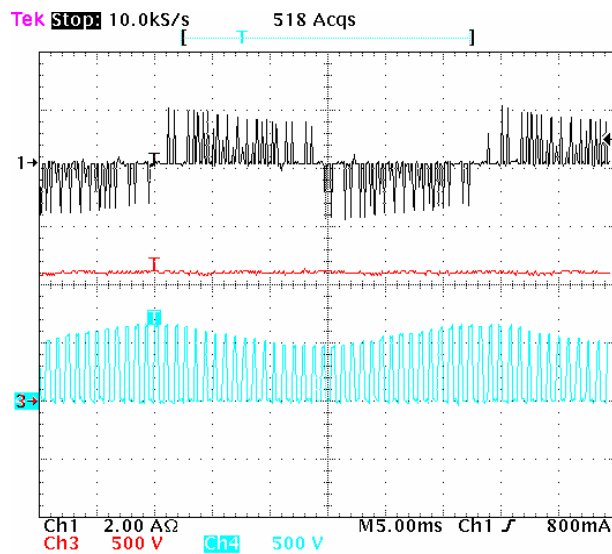
Fig. 5.4. Experimental and simulation results of a prototype NPC multilevel dc-dc converter.

Similar testing was conducted on a single phase half bridge multilevel dc-ac inverter. The final target application was a three phase PMSM motor drive. Experimental results

of Fig. 5.5 show the apparent need for active middle point balancing. The details of the successful implementation of the motor drive is presented in the next sections.



(a) Experimental results at no load.



(b) Experimental results at 50% load.

Fig. 5.5. Experimental results at no load (a) and load (b) showing the effect of not using middle point voltage balancing.

### 5.2.1 Topology Selection for a Compact Harsh Environment PMSM Drive

An understanding of the multilevel inverter topologies, the results of the device qualification of previous chapters, packaging considerations, and an understanding of the power delivery system are used in this section to make an informed choice on the most suitable multilevel inverter topology for the motor drive at hand. The available power delivery system provides a floating voltage on two power terminals, and a ground connection. Due to packaging constraints, the use of the isolated H-bridge multilevel inverter was ruled out. This topology would have required excessive real estate in this case, and the nature of the application would immediately eliminate this. A study of the switching states of the NPC inverter and the flying capacitor inverter also revealed another consideration. It is common practice to utilize the converter zero states to control the middle point voltage. It was seen that the extra redundancy available with the flying capacitor inverter shown in Fig. 5.6 would prove beneficial from a thermal point of view. The presence of redundant states would help in the thermal performance of the converter. One of the possible recommendations in literature regarding this issue is given in [27], where a parallel device was placed in parallel with the each of the two inner switches and alternate use of the devices was shown to be beneficial from a thermal point of view.

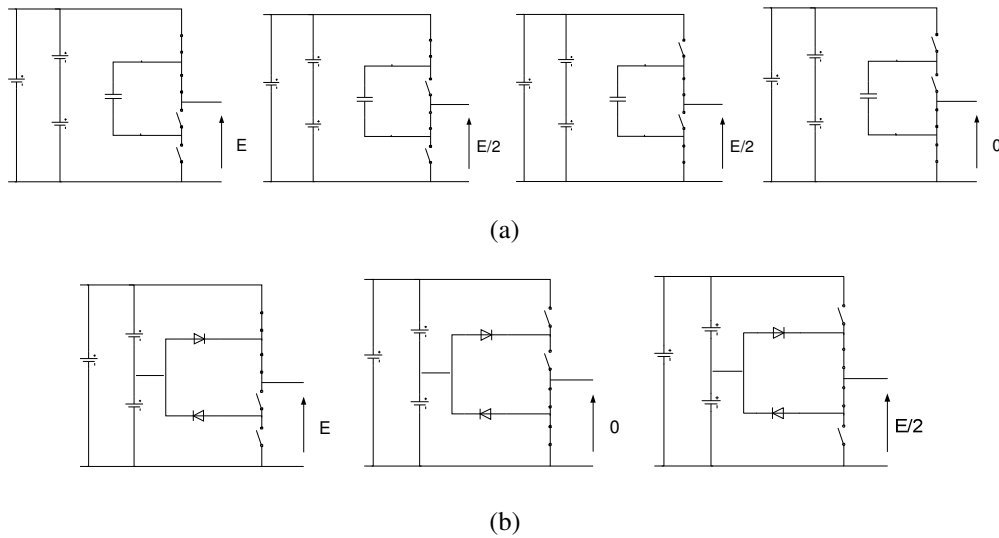


Fig. 5.6. Switching patterns for different voltage levels for the flying capacitor inverter (a) and NPC (b).

Moreover, the need for more active devices for the NPC case would mean these devices may need to be placed in the developed power module. The available real estate of the power module did not make that a possible solution. Moreover, the addition of the clamping diodes outside the power module placed severe restrictions on the packaging, heat sinking, leakage inductances of the associated wiring. Thus, a decision to utilize the flying capacitor multilevel inverter was made. A simplified schematic of the developed converter is shown in Fig. 5.7. It can be seen that less wiring connections are required between each of the phase legs than the NPC case. Space restrictions and the advantage of eliminating as many inter-phase connections as possible also favored the flying capacitor inverter.

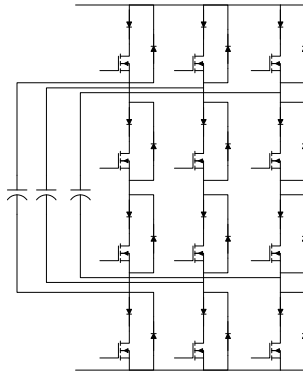


Fig. 5.7. Simplified schematic of the three phase flying capacitor multilevel inverter prototype.

### 5.2.2 Algebraic SVPWM

The objective of this section will not be the presentation of new modulation algorithm. This was not seen to be within the scope of the current work. However, an assessment of many of the modulation algorithms published in literature has been made [28][29][30][31][32]. The algebraic space vector pwm method presented in [28] was used as the means of control for the converter at hand. One advantage is the simple implementation that requires no trigonometric calculations and a very minor number of calculations. This provides an advantage in an elevated temperature application where computational capability is inversely proportional to how high the ambient temperature is. The algebraic SVPWM method lends itself well to implementation on an FPGA or even using discrete logic. However, in the prototype at hand, a DSP implementation will be used to illustrate the concept and test the power electronic related aspects.

Considering that each phase has four different switching states, the three level inverter of Fig. 5.7 has 64 ( $4^3$ ) possible switching states. The switching states can be classified into four groups. The Z group corresponds to the ten configurations

generating zero voltage vectors. The S group corresponds to vectors producing an amplitude of  $E/3$ . The M group corresponds to vectors producing an amplitude of  $\sqrt{3}E/3$ , and the L group vectors have a magnitude of  $2E/3$ . To assure a low harmonic distortion of the output voltages, only the three inverter voltage vectors closer to the reference voltage are used in a switching period. With this in mind, the hexagon shown in Fig. 5.8 is divided into twenty-four triangles.

Capacitor or middle point voltage control was seen as a necessity from the initial test results. The load is directly connected to the DC bus in the P and N states and no capacitor voltage control takes place. The capacitor is however charged in the A state and discharged in the B state of Fig. 5.9. Thus, proper choice of these states would enable control of the flying capacitor voltage.

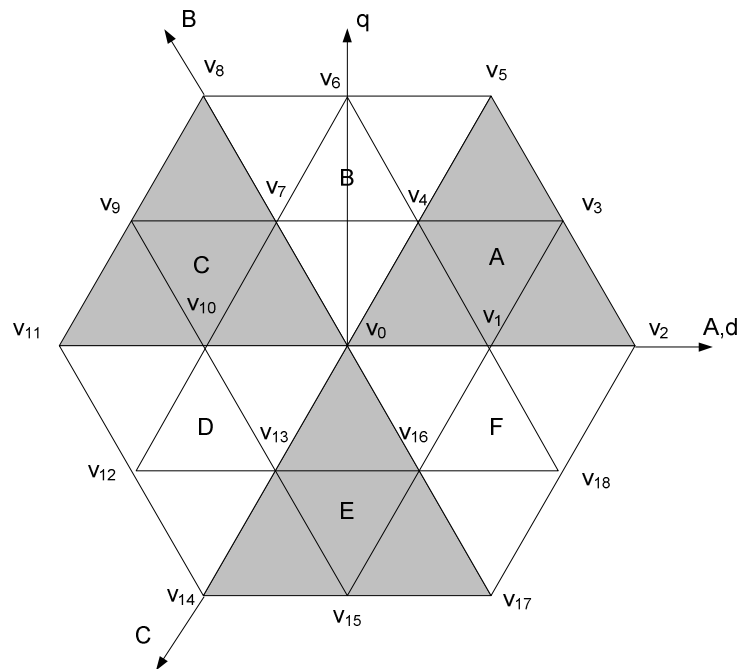


Fig. 5.8. Voltage space vectors of a three level inverter.

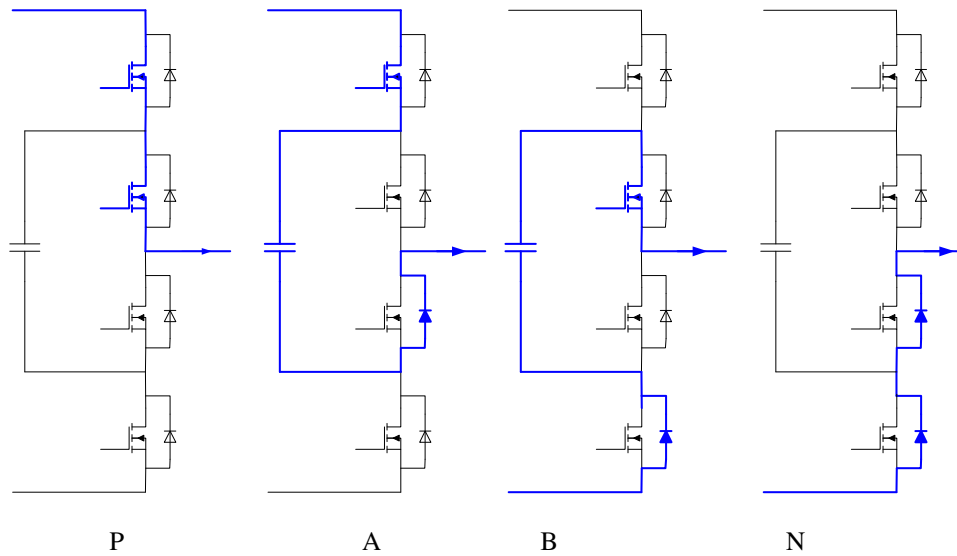


Fig. 5.9. Inverter switching states (P, A, B, N) and the relevant capacitor current control paths.

The details of the derivation of the algorithm are detailed in [28] so a reiteration of the derivation will not be necessary, however, the results and how they fit in an algorithm will be presented in the remainder of this section. The algorithm inputs are  $\bar{v}_{an}^*(k)$ ,  $\bar{v}_{bn}^*(k)$ , and  $\bar{v}_{cn}^*(k)$ . The following steps illustrate to space vector PWM algorithm within a given sector.

1. The reference voltages are ordered with  $\bar{v}_{1n}^*(k) > \bar{v}_{2n}^*(k) > \bar{v}_{3n}^*(k)$  based on (5.3).

$$\left\{ \begin{array}{l} A \quad \bar{v}_{an}^*(k) > \bar{v}_{an}^*(k) \geq \bar{v}_{an}^*(k) \\ B \quad \bar{v}_{bn}^*(k) \geq \bar{v}_{an}^*(k) > \bar{v}_{cn}^*(k) \\ C \quad \bar{v}_{bn}^*(k) > \bar{v}_{cn}^*(k) \geq \bar{v}_{an}^*(k) \\ D \quad \bar{v}_{cn}^*(k) \geq \bar{v}_{bn}^*(k) > \bar{v}_{an}^*(k) \\ E \quad \bar{v}_{cn}^*(k) > \bar{v}_{an}^*(k) \geq \bar{v}_{bn}^*(k) \\ F \quad \bar{v}_{an}^*(k) \geq \bar{v}_{cn}^*(k) > \bar{v}_{bn}^*(k) \end{array} \right. \quad (5.3)$$

2. If  $\left( \left( \bar{v}_{1n}^*(k) - \bar{v}_{3n}^*(k) \right) \geq E \right)$  then the voltage vector is in the overmodulation region and (5.4) and (5.5) apply.

$$K_1 = \frac{E}{\bar{v}_{1n}^*(k) - \bar{v}_{3n}^*(k)} \quad (5.4)$$

$$\left\{ \begin{array}{l} \bar{v}_{1n}^*(k) = K_1 \bar{v}_{1n}^*(k) \\ \bar{v}_{2n}^*(k) = K_1 \bar{v}_{2n}^*(k) \\ \bar{v}_{3n}^*(k) = K_1 \bar{v}_{3n}^*(k) \end{array} \right. \quad (5.5)$$

3. If  $\left( \left( \bar{v}_{1n}^*(k) - \bar{v}_{3n}^*(k) \right) \leq \frac{E}{2} \right)$  then vector in region 1 and (5.6) applies.

$$\left\{ \begin{array}{l} \tau_{pa}(k) = \frac{T}{4} + \frac{T}{2E} \left( \bar{v}_{an}^*(k) - \bar{v}_{cn}^*(k) \right) \\ \tau_{na}(k) = \frac{T}{4} - \frac{T}{2E} \left( \bar{v}_{an}^*(k) - \bar{v}_{cn}^*(k) \right) \\ \tau_{pb}(k) = \frac{T}{4} + \frac{T}{2E} \bar{v}_{bn}^*(k) \\ \tau_{nb}(k) = \frac{T}{4} - \frac{T}{2E} \bar{v}_{bn}^*(k) \\ \tau_{pc}(k) = \tau_{na}(k) \\ \tau_{nc}(k) = \tau_{pa}(k) \end{array} \right. \quad (5.6)$$

4. If  $\left( \left( \bar{v}_{1n}^*(k) - \bar{v}_{2n}^*(k) \right) > \frac{E}{2} \right)$  then vector in region 2 and (5.7) applies.

$$\begin{cases} \tau_{pa}(k) = \tau_{nc}(k) = \frac{T}{E} \left( \bar{v}_{an}^*(k) - \bar{v}_{cn}^*(k) \right) \\ \tau_{na}(k) = \tau_{pb}(k) = \tau_{pc}(k) = 0 \\ \tau_{nb}(k) = -\frac{3T}{E} \bar{v}_{bn}^*(k) \end{cases} \quad (5.7)$$

5. If  $\left( \left( \bar{v}_{2n}^*(k) - \bar{v}_{3n}^*(k) \right) > \frac{E}{2} \right)$  then vector in region 4 and (5.8) applies.

$$\begin{cases} \tau_{pa}(k) = \tau_{nc}(k) = \frac{T}{E} \left( \bar{v}_{an}^*(k) - \bar{v}_{cn}^*(k) \right) \\ \tau_{na}(k) = \tau_{nb}(k) = \tau_{pc}(k) = 0 \\ \tau_{pb}(k) = -\frac{3T}{E} \bar{v}_{bn}^*(k) \end{cases} \quad (5.8)$$

6. Else region vector in region 3 and (5.9) applies.

$$\begin{cases} \tau_{pa}(k) = \tau_{nc}(k) = \frac{T}{E} \left( \bar{v}_{an}^*(k) - \bar{v}_{cn}^*(k) \right) \\ \tau_{na}(k) = \tau_{pc}(k) = 0 \\ \tau_{pb}(k) = \frac{T}{2} + \frac{T}{E} \left( \bar{v}_{bn}^*(k) - \bar{v}_{an}^*(k) \right) \\ \tau_{nb}(k) = \frac{T}{2} + \frac{T}{E} \left( \bar{v}_{cn}^*(k) - \bar{v}_{bn}^*(k) \right) \end{cases} \quad (5.9)$$

The algebraic SVPWM algorithm has been outlined in this section based on the research carried out in [28]. The fast execution times and simple instructions required, made it an ideal candidate for the implementation at hand. Simulations were carried out

to verify the implementation. The condition simulated in Fig. 5.10 was for a reference line voltage of 220 V/60 Hz with an R-L load of 11 ohm and 22 mH, a bus voltage of 1kV, 15 uF capacitor, and a PWM frequency of 10 KHz. It is clear that the capacitor voltage is properly balanced.

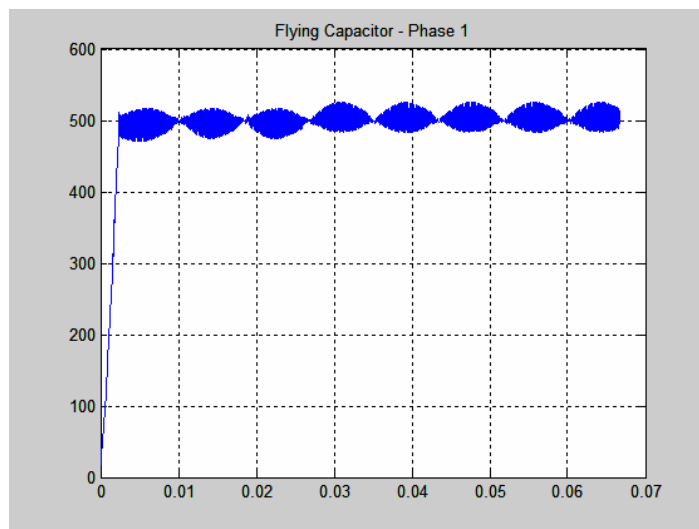


Fig. 5.10. Simulation results of the SVPWM showing phase A flying capacitor voltage  $V_{dc} = 1\text{kV}$ .

### 5.3 Limitations of a Compact Harsh Environment Implementation

The same devices that have been qualified in a previous chapter were to be used in the current prototype. It was mentioned earlier that no device does exist commercially to operate above 800 V in a motor drive application with ambient temperatures above 175°C. Thus, the use of multilevel converters was seen as the enabling technology that will permit delivery of higher powers to down hole tools. An experimental prototype

was used to verify that this can in fact be achieved. To main limitations surfaced as the work progressed.

The main limitation is that of the basic switching unit and the harmful overvoltages experienced by the series blocking diodes shown in Fig. 5.11. This is the same phenomenon described earlier, however, for the multilevel inverter case, the diode overvoltages were reaching the bus voltage and many failures occurred during the testing. During the operation with a two level inverter in a previous chapter, the over voltages would reach the bus voltage but since the bus voltage was lower than the diode rating, failures weren't common, but abnormal converter behavior was the issue. In the multilevel inverter case, the overvoltage was hindering the progress and burning the converter.

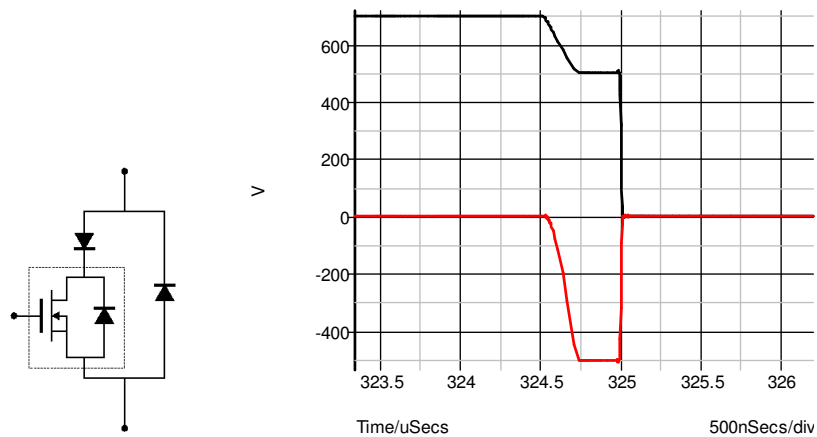


Fig. 5.11. Basic switching unit (left) simulation results of the blocking diode overvoltage problem (right).

The overvoltage failure mode of the series blocking diode was solved in a similar fashion to what was presented in a previous chapter. A modification of the capacitive

divider using an external capacitor in parallel with the blocking diode, enabled the successful operation of the converter.

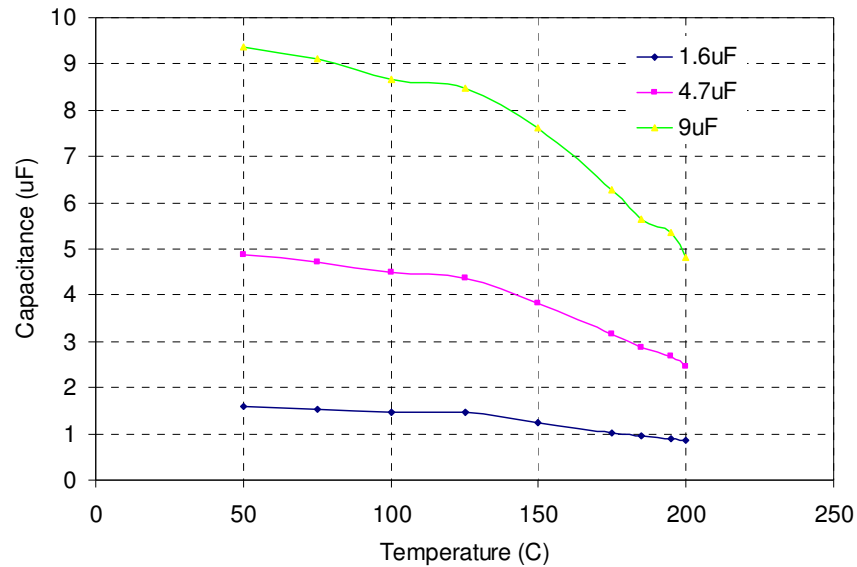


Fig. 5.12. Experimental results showing the effect of temperature on high voltage ceramic capacitors

The effect of temperature on capacitor values was the second main challenge. The only high voltage capacitor technology that will survive extreme temperature and is available at a commercial scale is the multilayer ceramic capacitor. Fig. 5.12 show illustrates how half the capacitance value is lost at the needed temperature range. This was very conflicting with the stringent packaging requirements. However, because of our use of Mosfets, the increase in switching frequency was possible and enabled the operation at the required power levels and a feasible packaging solution.

## 5.4 Experimental Results

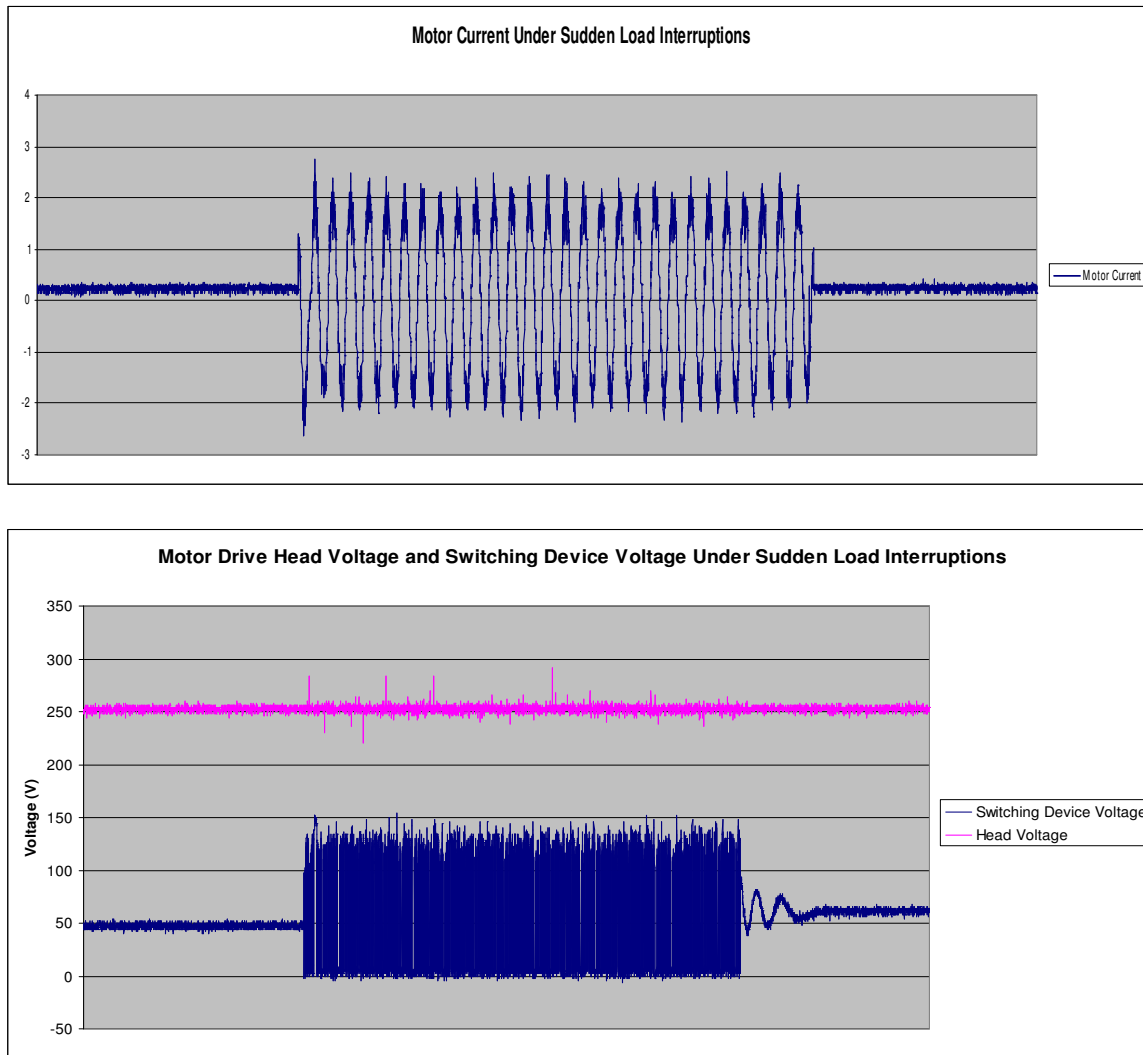


Fig. 5.13. Performance of the prototype inverter under sudden load changes, load current (top) and device and bus voltage (bottom).

Experimental results conducted on the prototype motor drive are shown in Figs. 5.13 and 5.14. Resistive dividers were connected to the flying capacitors in all the phases to allow the initial charging of the capacitors to a suitable value. The motor drive would

only start if the capacitors are charged. In Fig. 5.13, the effect of a sudden load on the inverter is shown. It is clear that switch voltages do not exceed their rated voltage even under such severe operating conditions. The complete motor drive was then temperature tested to assess the feasibility of its elevated temperature operation. This is shown by the results of Fig. 5.14. Further testing is currently being conducted to optimize the drive performance.

After the successful implementation and testing of the converter, it is perhaps important to demonstrate why the compact harsh environment designs are a challenge. This is clear by looking at Fig. 5.15. The complete assembly of Fig. 5.15 fits inside a pressure housing with a  $3\frac{3}{8}$  OD, and an ID depending on pressure rating. This layout at hand packages two flying capacitor multilevel inverter motor drive along with all the associated passive components and control boards.

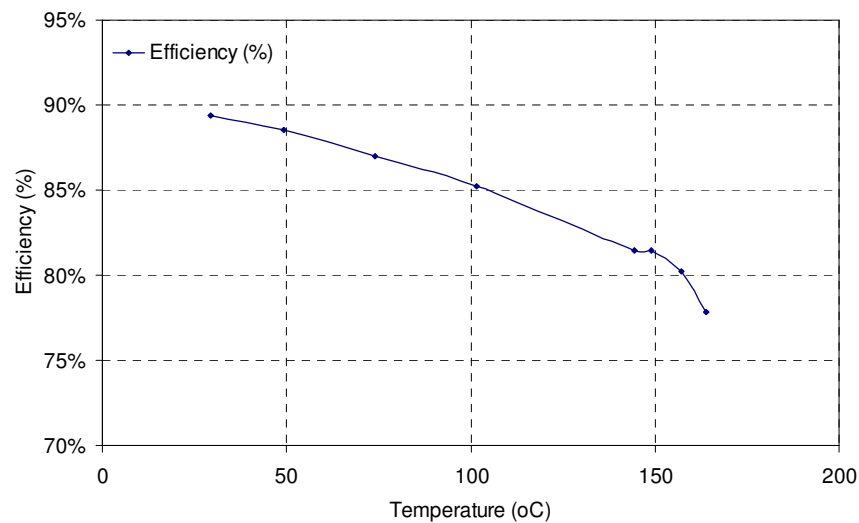


Fig. 5.14. Motor drive efficiency vs temperature



Fig. 5.15. Layout showing a tool with two multilevel inverters; each black heat sink is for one phase leg.

## 5.5 Conclusion

This chapter started by illustrating how long resistive cables used in the operation of remote instrumentation impose fundamental limits on the amount of power delivered. This type of power delivery is used in many engineering systems such as in the operation of underwater remotely-operated vehicles, in oil well logging and drilling, in mining, and in highly distributed power systems (air craft, submarines etc.). The specific application at hand is the oil well logging application. The chapter built on the knowledge and testing results of previous chapters, and illustrated the need for using multilevel power converters to deliver higher power to down hole tools. During the progress of the work, both dc-dc and dc-ac converters were developed and tested. The major discussion presented in the chapter is related to the development of a multilevel PMSM motor drive. A verified SVPWM algorithm from literature was used, and simulation and experimental results verified its potential. The series blocking diode overvoltage failure mode and the capacitor packaging constraints were seen as the main challenges to a high temperature compact application. The passive mitigation technique previously proposed also proved successful in the multilevel inverter case where voltage values across the diode reached full bus voltage during the deadtime and was the cause of significant failures. The use of Mosfet devices enabled the increase of the switching

frequency to a limit that enabled the successful packaging of the flying capacitors and the operation at the rated power levels even with the limited capacitance value seen at elevated temperature.

**CHAPTER VI**  
**EXTENDED TEMPERATURE HIGH RELIABILITY MOTOR DRIVE**  
**SYSTEMS FOR HARSH ENVIRONMENT APPLICATIONS**

**6.1 Introduction**

The previous chapters have addressed two main topics, namely, the electromechanical subsystem and the power electronic subsystem of a harsh environment energy conversion system. The previous work has built upon many of the conventional approaches providing some novel solutions to the hurdles faced during the development. In this chapter a different approach will be taken. A completely new look at the problem of designing a motor drive system for a harsh environment will be addressed. A novel method for brushless motor commutation and control will be presented in this chapter. This task is most commonly accomplished using an electronic motor drive. One of the main contributors to the development costs of an electromechanical project can be the development of the motor drive. This is especially true in downhole tool development where the harsh environmental conditions limit the application of commercially available electronics. Thus, it is the objective of this novel principle to reduce or eliminate the need for power conversion electronics used in brushless motor commutation and control for operation under elevated temperatures.

**6.2 Prior Art**

Electric motors are the main means by which electrical energy is changed into mechanical energy. In industrial applications, electric motors range in size and power rating. There are several different types of motors in industrial use today, however, they can be grouped into two main categories, namely, brush and brushless. Brushless

motors are in general made of a stator with a stator winding, and a rotor. The rotor can be made up of only laminations, as is the case with switched reluctance and synchronous reluctance motors. It can be made of a shaft with magnets mounted in different configurations as in brushless dc motors, or permanent magnet synchronous motors. The rotor can also be laminated and can have winding(s) as in induction motors and some synchronous motors. Or in the general case, the rotor can be a combination of all the above technologies. One thing all these technologies have in common is the need for an input voltage with variable magnitude and frequency to control them. Typically, a three phase inverter is used for this task, and electronic commutation of a dc voltage is used to provide the variable voltage and frequency. In an ideal case, the use of a brushed dc motor would have eliminated the need to use an inverter in many applications, especially ones that already have a provision for a variable dc voltage. In other cases, one would only need a variable dc voltage to control the motor, which would cut down the amount of electronics, and thus increase the efficiency and reduce the cost. The use of brushed dc motors, however, has many problems. The problems include “wear of the brush and rotor contact during use, arcing, resistance and heating at the brush-contact interface, and burning of the brush during temperature extremes.” Moreover, in downhole applications, the use of brushed dc motors is simply not possible because of the difficulty in placing the motor in air and applying a rotating seal that can withstand full differential pressure and motor torque. Placing the motor in oil will also not be possible because the brushes and the commutator segments on the rotor need to be in contact in order to conduct electric current. The presence of an oil film between these two contacts, prevents proper conduction of current, thus, inhibits torque production.

The following literature is what I have found that relates to the work at hand. This literature was all found during a literature search conducted upon finding this to be an idea that can be of value. McGaughey and Tanh M. Bui [33] present methods of mechanical commutation of brushless dc motors. Pengov [34] then presents a very similar solution applied to switched reluctance motors. Theoretically, the solutions are applicable to any brushless motor with varying degrees of suitability or performance limitations for each type of brushless motor.

McGaughey and Tanh M. Bui [35] have both tried to address the drawbacks of using brushes in their work. Pengov [34], however, has limited his work to the elimination of the complex electronics associated with driving a switched reluctance motor. The proposed solution, in its current form, will deal with some of the issues associated with the use of brushes especially as it relates to downhole applications. It will also aim at reducing or eliminating down hole power electronics in certain cases. However, it will be an objective to attempt to completely eliminate the problems with using brushes as this work progresses, and more experimental data is collected on this issue.

### **6.3 Summary of the Principle**

The proposed solution consists of an apparatus that can be mounted in the vicinity of a brushless motor in order to provide the necessary commutation signals to control the motor. The apparatus consists of a magnetic coupling between a motor shaft and a rotating ring. Mounted on that ring are two conducting segments placed 180° apart. Two conducting strips on either side of the ring are each connected to a certain conducting segment. Brushes pushing against this rotating ring are then used to provide

the required commutation, and deliver the required power to the motor. The brushes are connected to both the input power supply and to the motor. The rotating ring and brush assembly can be located in air and are coupled to the motor shaft through the magnetic coupling. In another implementation, the brushes and ring assembly can be located in a container placed in the vicinity of the motor. The container should be able to withstand full pressure and would have feed-throughs to connect the assembly with the power supply on one side and the motor on the other. Thus, the proposed solution can be seen as an improvement on what the prior art has presented that is especially suitable for operation in a downhole environment.

#### **6.4 Detailed Description of the Principle**

In order to appreciate the proposed solution, it would be essential to quickly go through the theory of operation of brushed dc motors. Fig. 6.1 shows a simplified drawing illustrating the operating principles of a dc motor and the main functions of its components. This simplified drawing shows two brushes  $b_1$  and  $b_2$  connected to a current source supplying current  $i_a$ . The brushes are placed against commutator segments  $s_1$  and  $s_2$ . The figure also shows a winding connected to  $s_1$  and  $s_2$  and placed in a magnetic field created by permanent magnets. In its current position, current will pass from the current source into  $b_1$  and  $s_1$  into side 1 of the coil and back through side 1' and  $s_2$  and  $b_2$ . Due to current passing in a conductor placed in a magnetic field, a force will develop on the conductor. Each side of the turn will then have a force developed that is opposing the other in direction. The presence of two forces on either side of the turn will then produce torque, which will in turn cause the rotor to rotate.

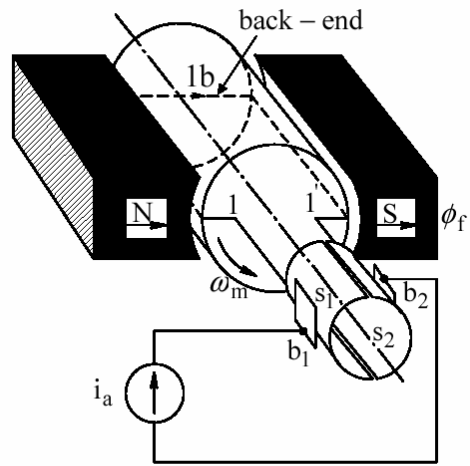


Figure 6.1. Simplistic view of a brushed dc motor.

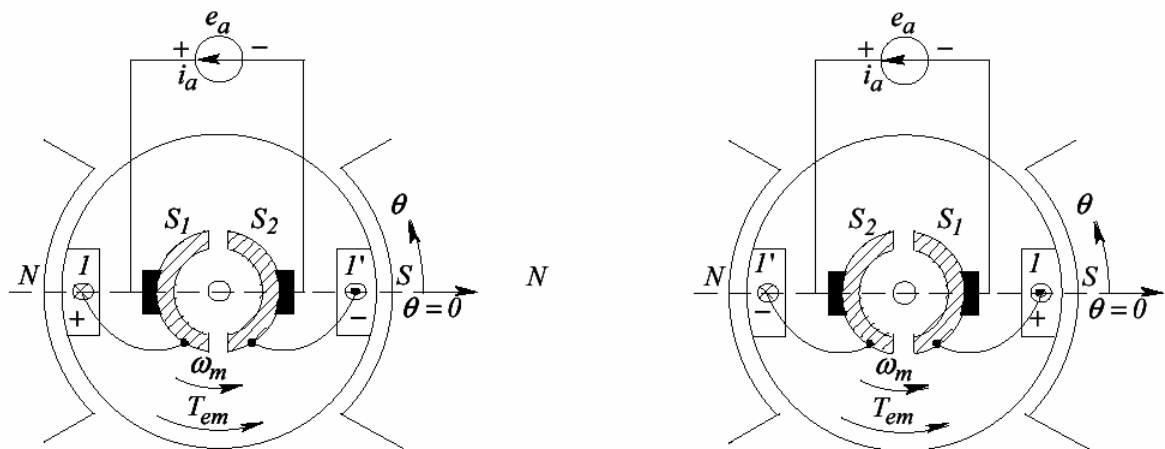


Figure 6.2. Principle of operation of brushed dc motors.

In Fig. 6.2, the rotation of the motor to a new state is illustrated, whereas, positive current flowing in side 1 on the left creates a torque that rotates the rotor, and thus, side

1' on the right is now carrying the positive current. Thus, the brushes act as a means to flip the current in the proper winding.

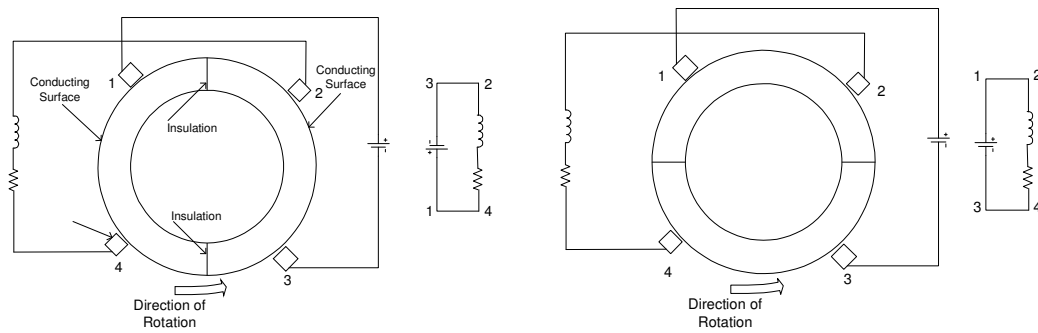


Figure 6.3. Production of alternating current in an R-L circuit.

Fig. 6.3 shows an example of the application of brushes to produce an alternating current in an R-L load. From Fig. 6.3 and a presentation of torque production of a brushless dc motor shown in Fig. 6.4, we will be able to come to a complete understanding of the proposed solution. Figure 6.3 shows two semicircular segments with a small insulating layer between them. The top of each of the segments is conducting, and brushes are placed in a certain pattern around the segments. The equivalent circuit of the system is then shown on the right where an R-L load and a power source are connected in a certain configuration due to the brushes and their contact with the segment conducting surfaces. If the semicircular segments were rotated as shown on the drawing, another equivalent circuit will be created. The means of rotation of the segments in this case is not significant to the explanation. Because this is a simple R-L load, the rotation will need to be applied using an external means.

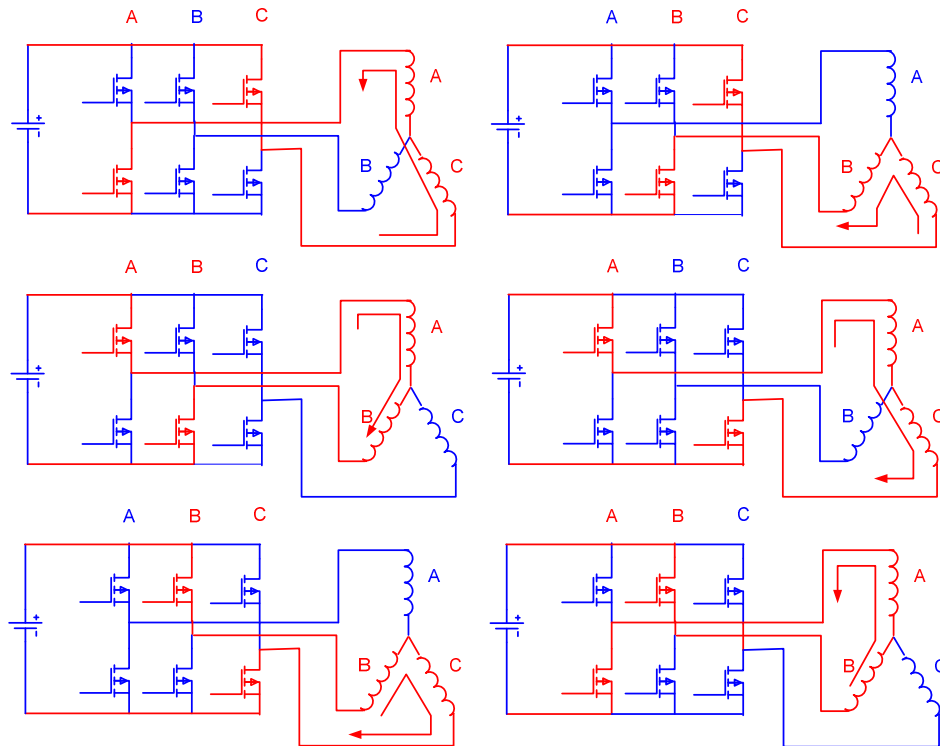


Figure 6.4 Current flow in a 3 phase brushless dc motor winding.

In figure 6.4, the current flow diagrams required for torque production in a brushless dc motor are presented. It can be seen that at each moment in time current will be flowing between two terminals or in two phases. If current were to flow in this pattern, torque would be produced in the motor and rotation would occur. This is conventionally accomplished using an electronic inverter as shown in Fig. 6.5 where hall sensors would indicate the beginning and end of each of the six sectors shown in Fig. 6.4 and a controller would send the proper signals to the IGBT driver to connect the appropriate phases to the DC rail, thus, forcing current into the phases.

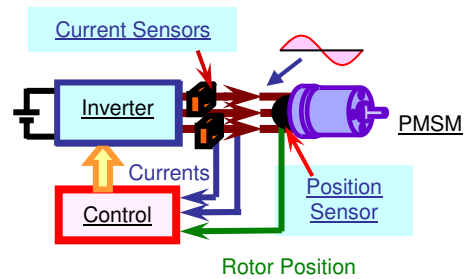


Fig. 6.5. Conventional electronic commutation using an inverter.

The proposed solution will aim at eliminating the need for the electronic three phase inverter. This is possible in applications requiring a constant speed, or where speed can be varied by merely changing the input dc voltage. The apparatus in one of its forms is shown in Fig. 6.6. The apparatus can be placed in a container that can withstand full downhole pressure and placed next to the motor on the accessory shaft side as shown in Fig. 6.7, or the apparatus can be designed to be part of the air section of the downhole tool. It consists of a magnet assembly that produces a magnetic coupling with magnets that may have been previously used for hall sensing. The magnet is mounted on shaft that is allowed to rotate using a bearing. On the shaft is a ring with various conducting patterns on it. Two conducting segments placed  $180^\circ$  apart are each connected to two conducting strips. Each of the strips is connected to a corresponding power supply input terminal through brushes. A number of other brushes depending on the number of phases and poles of the motor are arranged around the shaft, as shown in Fig. 6.6. At any instant in time, two brushes are connected to the two conducting segments, thus, connecting the power supply terminals to the motor. Current flow in the motor produces torque which rotates the motor shaft, which in turn rotates the commutation assembly

which is magnetically coupled to the motor shaft. Very little power will be lost in this process as the lossy components would be the bearing losses, torque produced by brushes rubbing against the conducting segments, and the electrical losses in the brushes.

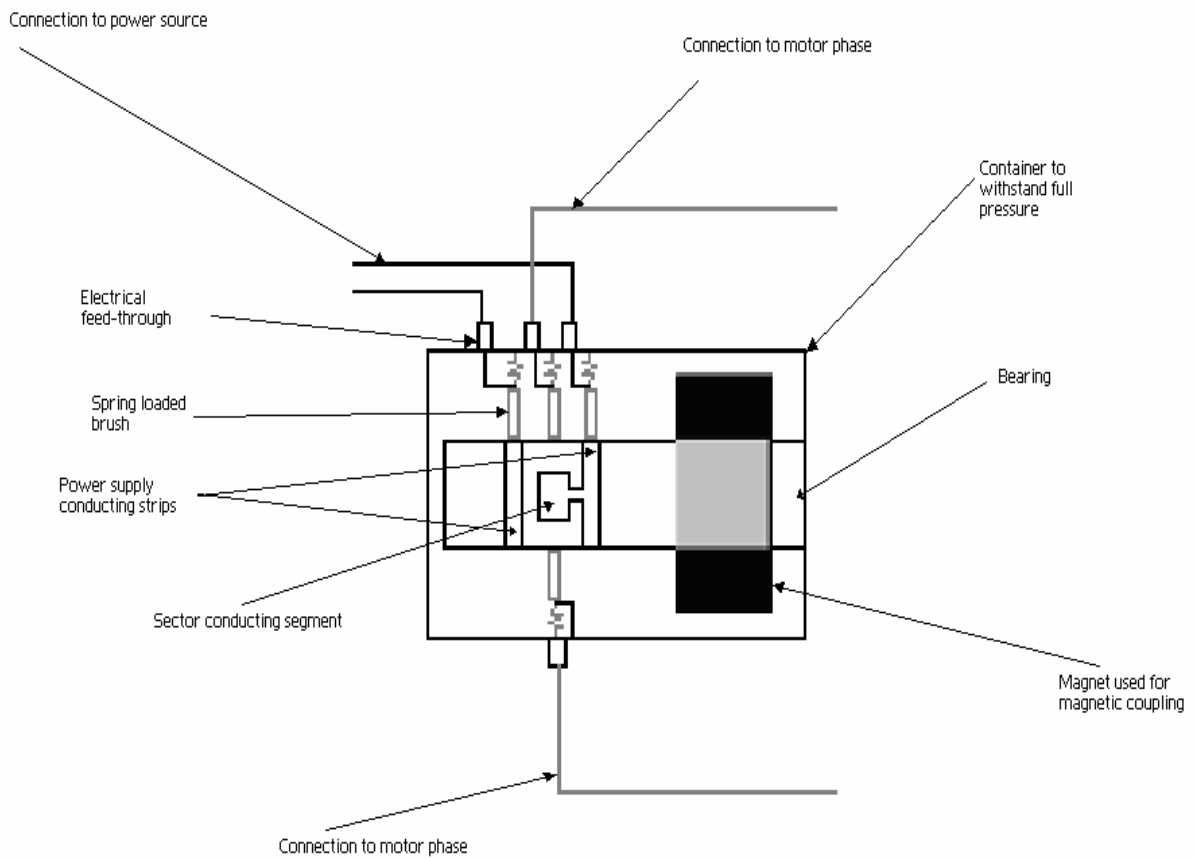


Figure 6.6. Apparatus used for motor commutation

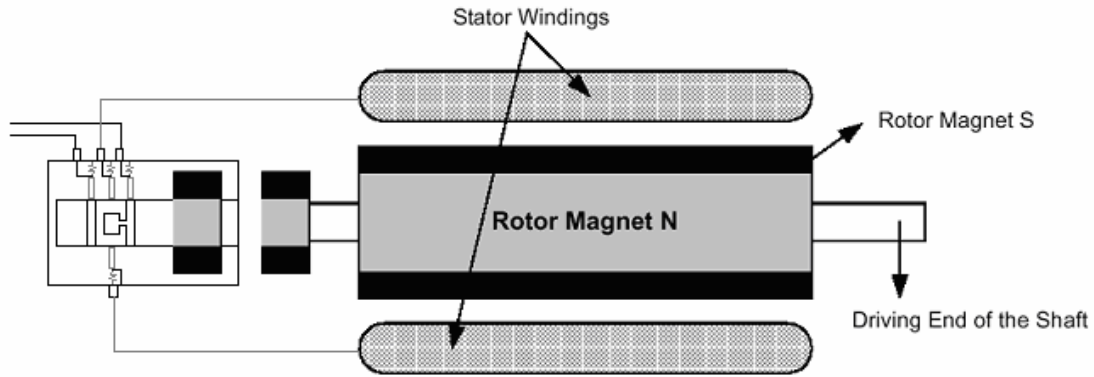


Figure 6.7. Final assembly including commutation apparatus.

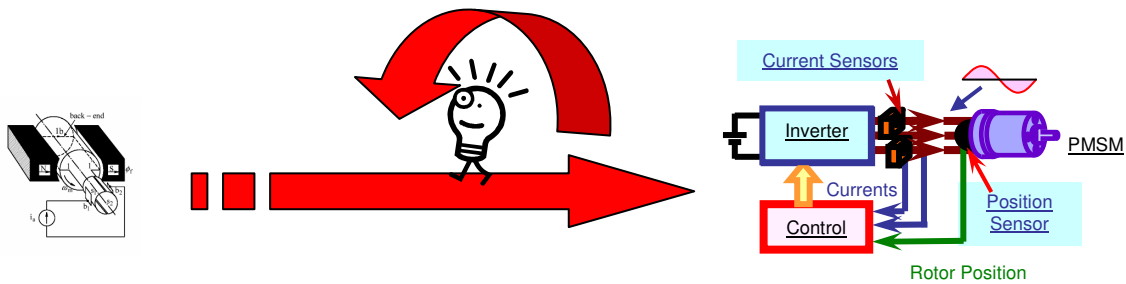


Figure 6.8. Thought process used.

Thus, from the information presented thus far one can relate the thought process to Fig. 6.8. Technology trends have helped migrate many application away from the use of the conventional brushed dc motor. Power electronics and DSP technologies have made motor drive systems based on these technologies very feasible. For a very unique application such as a harsh down hole environment, a different though process proved beneficial. A combination of current and older technologies along with a unique combination method have proved to be very beneficial for the application at hand. The next sections will deal with the progress of the prototypes developed to prove the

concept. Some testing results, and some limitations of the current approach will be provided along with some recommendations for future developments that can help mitigate some of the hurdles faced.

### 6.5 Commutator Design Considerations

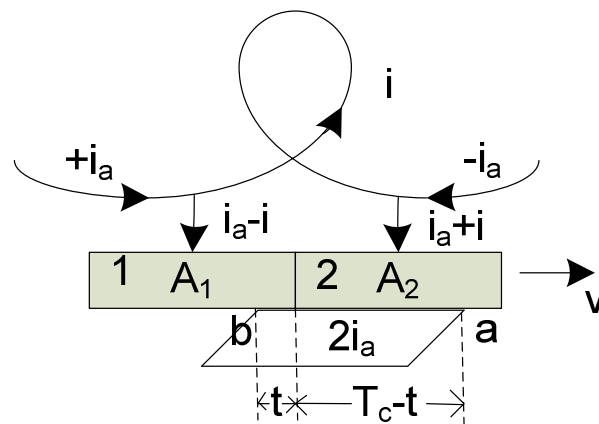


Fig. 6.9. Short-circuited winding element in dc machine commutation.

It is important to provide a quick review of commutation in a conventional dc machine before commutation in the proposed solution is discussed. Rotating in the magnetic field, the winding element of the dc machine changes from one armature path to another thus changing its current from  $+i_a$  to  $-i_a$  (or vice versa). During the time reversal the conductors of the winding element lie in the neutral zone and the winding element is short circuited. This explains the presence of alternating current in the motor windings as was previous discussed. Fig. 6.9 shows schematically a winding element of a lap winding with its connections to the commutator bars. It is assumed that the width

of the brush is equal to the width of the commutator bar. In this case, the brush can short-circuit only one winding element. In Fig. 6.9 the short circuit of the winding element begins when brush edge *a* leaves bar 2. *b* is the leading brush edge, and *a* is the trailing brush edge.

At the beginning of the short circuit period  $T_c$  ( $t = 0$ ), the current in the winding element is  $+i_a$ ; the brush is then on bar 2 only. At the end of the time  $T_c$  ( $t = T_c$ ), the current in the winding element is  $-i_a$ ; the brush is then on bar 1 only. At intermediate times, the brush lies on both bar 1 and bar 2.

If there are no further influences on the short-circuited winding element, the change-over of the current from  $+i_a$  to  $-i_a$  is determined by the magnitude of the contact areas of the brush with the commutator bars 1 and 2 (areas  $A_1$  and  $A_2$  in Fig. 6.9), ie., the current in the short circuited winding element is at any time given by (6.1). This equation corresponds to a straight line and is called the linear commutation case. This does not happen in practice due to effects like the self induced emf, and the emf due to the armature flux. [36]. Accelerated and delayed commutation are the two other ends of the spectrum. These are illustrated in Fig. 6.10. The current flowing through the contact area  $A_2$  at the end of the commutation period must be as small as possible for an acceptable commutation performance.

$$i = i_a \left( 1 - \frac{A_1}{(A_1 + A_2)/2} \right) \quad (6.1)$$

The instant of time shortly before the commutation period is finished,  $t = T_c - \Delta t$  will thus need to be considered. For this instant of time,  $A_2$  becomes equal to  $\Delta A_2$ . Since the times and the areas of Fig. 6.9 are proportional, (6.2) can be derived from (6.1)

after a substitution of  $t = T_c - \Delta t$ . The current which flows through  $\Delta A_2$  at  $t = T_c - \Delta t$  is  $\Delta i_a$ . If  $\Delta i_a$  can be made equal to zero at  $t = T_c - \Delta t$ , then no current flows through the contact area  $A_2$  at this time, the current density at the trailing edge of the brush is zero at the end of the commutation period. Thus, if the current in the short circuited winding element reaches its end value  $-i_a$  shortly before the commutation period is over, then this condition is satisfied. This corresponds to the accelerated commutation case in Fig. 6.10.

$$i = -i_a \left( 1 - \frac{\Delta t}{T_c/2} \right) \quad (6.2)$$

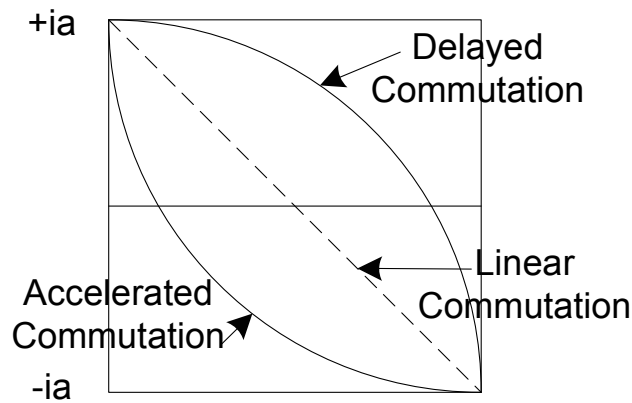


Fig. 6.10. Illustration of the different types of commutation.

Other factors that affect commutation are the brush material, the commutator material, the finish on the commutator material, brush pressure, coefficient of friction between the brush and commutator, etc. These were all factors that need to be thoroughly investigated before good commutation can occur. Consideration of these

factor is the reason more than one prototype commutator was built for the proposed solution as shown in Fig. 6.11..

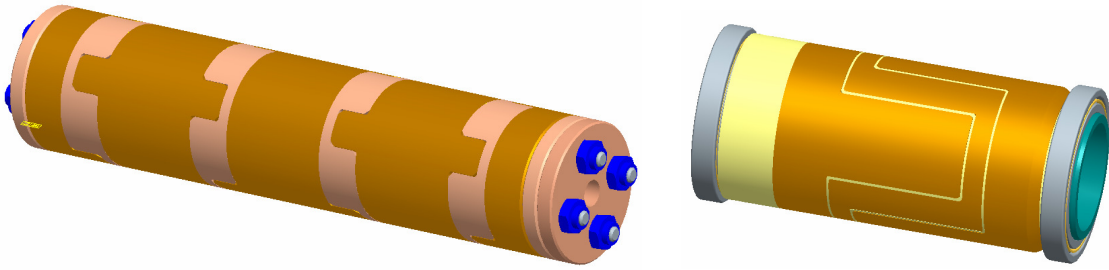


Fig. 6.11. First commutator prototype (left) latest prototype (right).

Although very similar in nature to the commutation in brushed dc motor. Current doesn't actually change directions in the proposed mechanical commutator, however, full load current is interrupted by the commutator action. Considerations such as coefficient of friction have also been of significant effect on the prototype built during the progress of this work. The brushes were seeing a significant change in coefficient of friction with the first prototype due to them sliding on copper then plastic sections. This was improved drastically in the second prototype that was built and tested to 2000 rpm. Although many of the secondary issues that affect commutation were taken into consideration, the commutation its self did cause some arcing. This was however, mitigated using a freewheeling diode as showing in Fig. 6.12. It is apparent, however that this solution will limit the direction of rotation to only one direction, because in the reverse direction the diodes will short circuit the power supply. This was seen acceptable for our current implementation. However, at higher voltages, arcing was still

present. This will be a topic of further research, and the next section will suggest a possible solution.

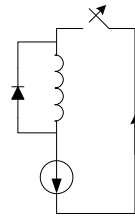


Fig. 6.12. Mitigation of the arcing using a freewheeling diode.

## 6.6 Soft Commutation

As illustrated in the previous section, the commutation in the proposed apparatus is similar in nature to that of a dc machine. The disconnection of load current from the winding is illustrated in Fig. 6.13 as it occurs in the proposed solution. Here phase C current will be disconnected in this mode of rotation, and thus, sparking will occur. This was mitigated to a large degree by the addition of a freewheeling diode in Fig. 6.12.

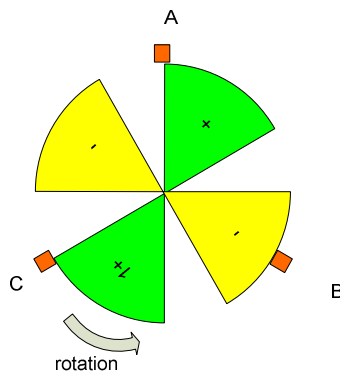


Fig. 6.13. Current commutation in the proposed system.

In this section, an introduction to a different solution that may enable extended brush life operation and suppression of arcing at higher operating voltages and currents. A similar approach was presented in [37] for the conventional brushed dc machine. Although our apparatus is different, a similar solution can be applied. The principle of soft commutation in PWM converters has been known and studied by many researchers. The application of this principle to the system at hand may however, prove beneficial. This will be a topic of future work but will be touched upon in this section. No experimental results will be provided here since further research and a good review of the different soft switching techniques in PWM converters needs to be carried out first.

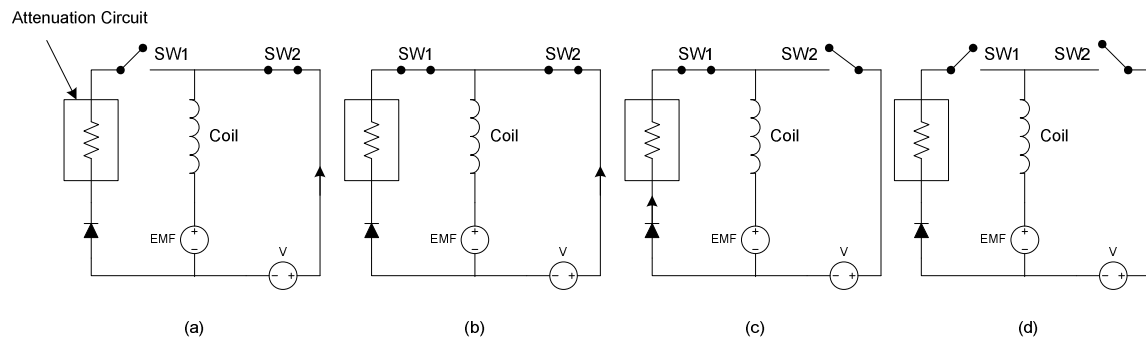


Fig. 6.14. Basic principle of soft commutation.

The basic principle of soft commutation as it is envisioned to apply to the apparatus at hand is illustrated in Fig. 6.14. The attenuation circuit shown in the figures may incorporate a feature of feeding the coil's magnetically stored energy back to the dc supply. It may also be designed to simply drain the energy. The complexity will dictate

the functionality received from the circuit. A diode connected in series as part of the attenuation circuit branch prevents unwanted current flow. Fig. 6.14(a) shows the normal operating condition. When the coil is about to be commutated, Fig. 6.14(b) SW1 is on. Because of the diode, there is no current flowing in this branch of the circuit. When SW2 is opened Fig. 6.14(c), the residual current in the coil does not need to force through the gap of SW2 by means of a spark. It seeks the path through the attenuation circuit whose functionality is best described as a variable impedance. The initial impedance after SW2's opening should be low to reduce the potential difference across SW2. The impedance value changes after the attenuation of the initial current. Finally, when the current is drained, Fig. 6.14(d), SW1 is opened with a small potential difference across it [37]. The best implementation for such a principle in the application at hand is still under investigation and will be a topic of further study. The objective will however, be to reduce the amount of active components used in such a circuit.

## **6.7 Brush Assembly**

The first prototype was made from automotive parts bought commercially. Brush material, pressure, width, etc were not variables that were controlled for the work at hand. The first prototype of the brush assembly is shown in Fig. 6.15. The concept was proved and a more suitable implementation was needed. In the next prototype, electrographite brushes were used. These brushes are made of carbon that has been converted into graphite by baking at temperatures above 2500°C (4532°F). This temperature volatilizes impurities and produces a material of homogeneous structure, low in friction and non-abrasive. Their operating temperature range is not as wide as the graphite grades, but is fairly wide and they will withstand heavier electrical loads

without burning; they thus have a high overload capacity. These brushes are typically used from 24 V upwards [38]. Typical brush pressures on the commutator in an aerospace application have been recorded in literature as between 4 and 8 PSI [38]. This was used in the application at hand.

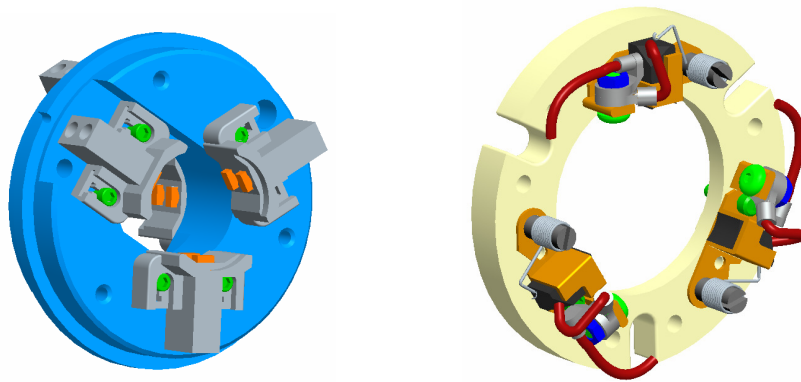


Fig. 6.15 First brush holder prototype (left) latest prototype (right).

## 6.8 Magnetic Coupling

Another component of the system is the magnetic coupling. The first vision, was to create a magnetic coupling that can withstand full torque and thus be able to place the motor in the air section of the tool. A magnetic coupling suitable for such an application was designed based on [39] and the experimental results are shown in Fig. 6.16. Two different yoke materials were used with different flux densities and testing results show that it is possible to build such a device. However, it was quickly realized that if such a device were used to couple the air and the oil sections of the tool, no space would be remaining for the needed wiring connections. Thus, this principle was abandoned, and

the proposed solution, which is the topic of the work at hand, is shown in the simplified diagram of Fig. 6.17. It is clear from this figure that the apparatus can be placed in the vicinity of the motor while the motor is kept in the oil section of the tool. Wires can still be routed to the air section of the tool with no effect on the spacing available in a negative fashion. Infact, with the apparatus at hand, the number of wires needed to run a motor that is placed in oil is reduced to just the two dc lines. This is a significant contribution of the work at hand. Running a similar motor using the conventional methods would require three high voltage wires, one chassis wire, and nine resolver wires. With wiring and harness problems being the main contributor to the failures of many systems extending to the space shuttles, this contribution was seen as a significant one.

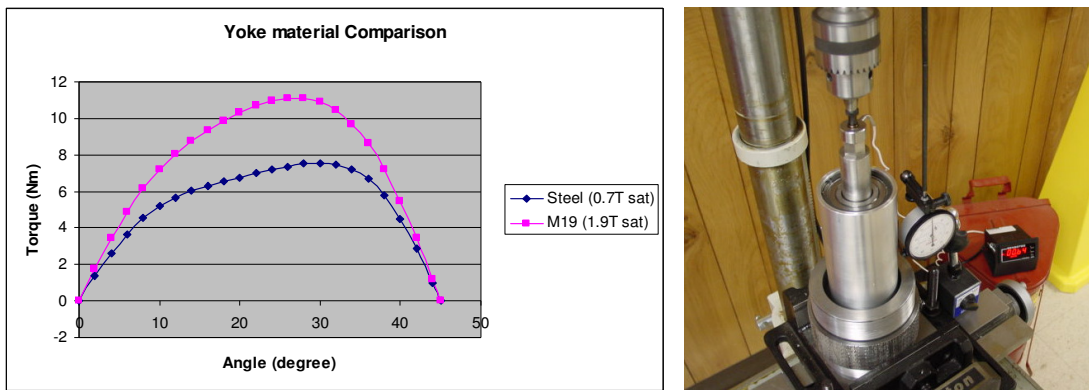


Fig. 6.16 Initial magnetic coupling concept, test results (left) and test setup (right).

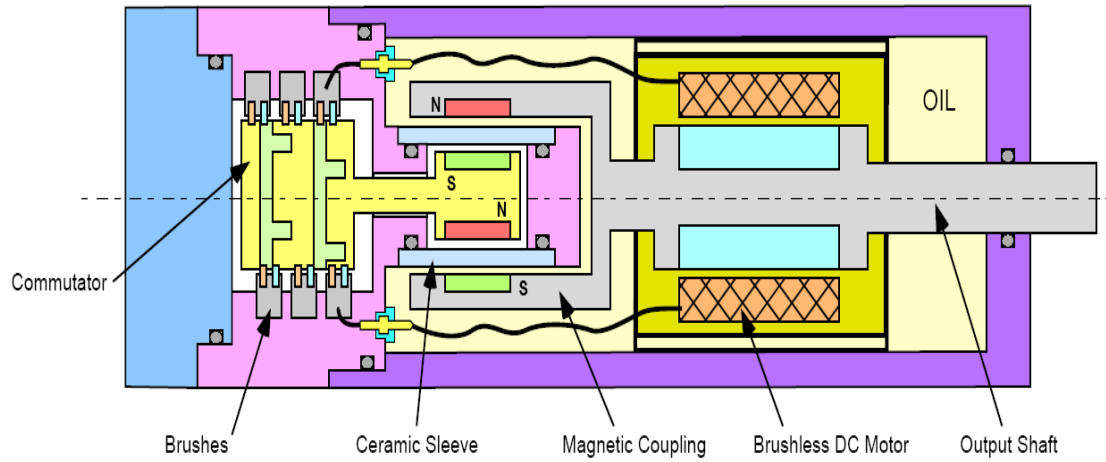


Fig. 6.17 Schematic illustration of the proposed system.

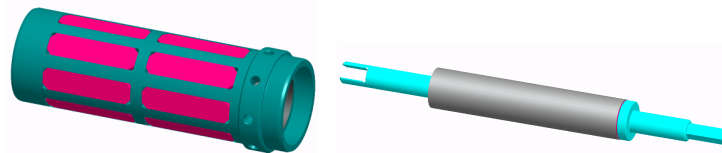


Fig. 6.18 Components of the magnet coupling of the second prototype

A model of the actual magnetic coupling using the developed prototype is shown in Fig. 6.18. The ceramic pressure barrier is not shown in this figure. The magnetic coupling design followed the same design procedure as in [39] and the result was an eight pole design rated for a brake away torque of 2 lb in.

## 6.9 System Progress and Experimental Results

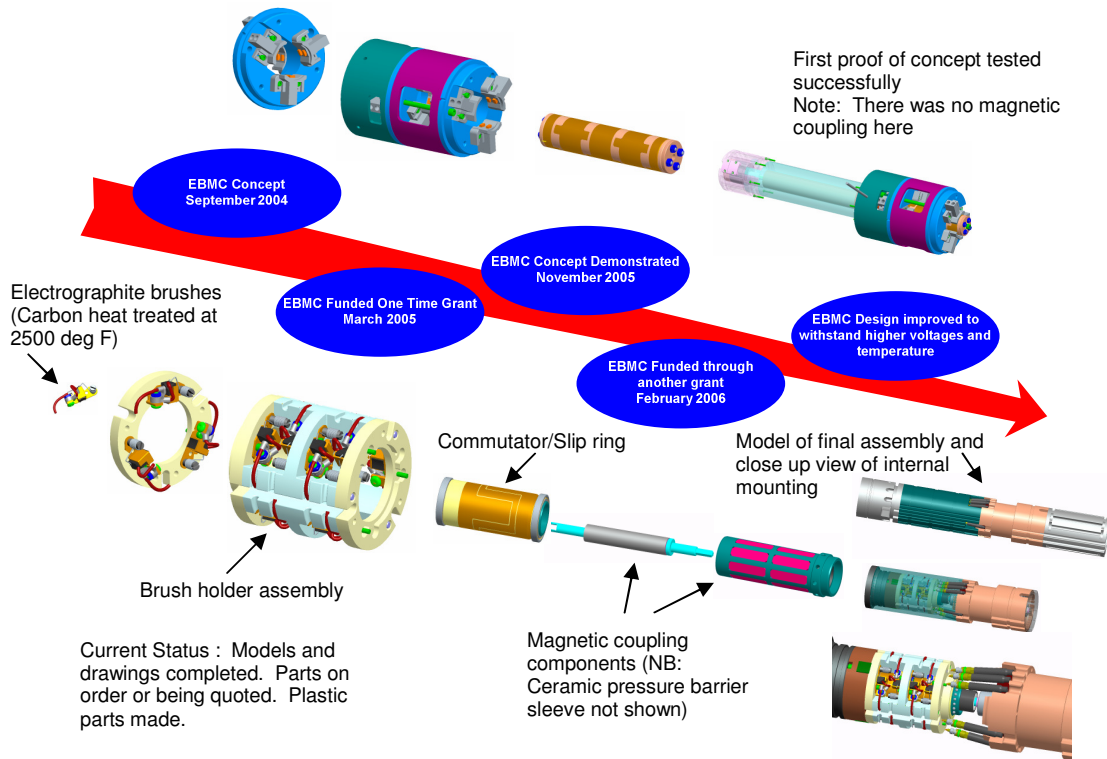


Fig. 6.19 Stages of the development.

The stages of the development starting from the initial concept until the writing of this work are shown in Fig. 6.19. The first proof of concept was very encouraging. The actual prototype is shown in Fig. 6.20. Although no magnetic coupling, bearings, proper commutator, etc were used, the concept was illustrated. Current and voltage waveforms are shown in Fig. 6.21.

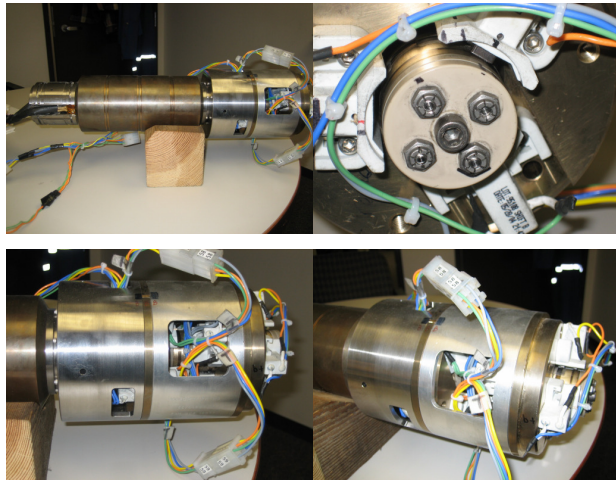


Fig. 6.20 First prototype of the commutator installed on the torque side of the motor

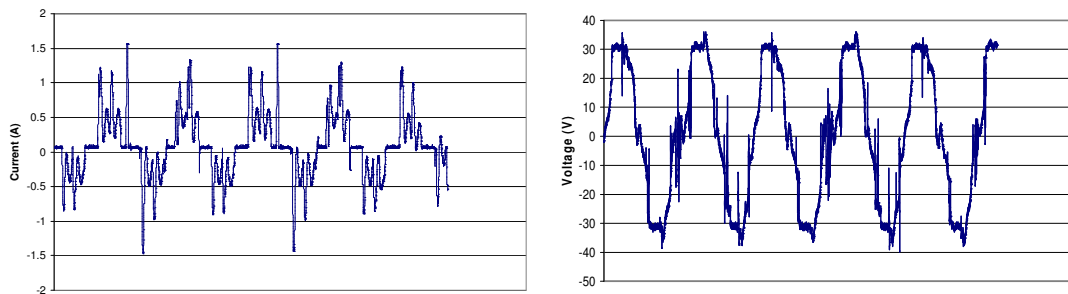


Fig. 6.21 Line current (left) and voltage (right) waveforms

A look Fig. 6.21 shows that the current is very peaky and that besides the expected current humps typical of a BLDC motor's current, there is sometimes a spike due to the arcing of the commutator. The lack of bearings and proper alignment was the main cause of this. These effects were drastically reduced in the second prototype built and shown in Fig. 6.22. Proper bearing support and a magnetic coupling were implemented in this prototype. It was installed on the resolver side of the motor after removing the resolver. Speeds up to 2000 rpm were achieved, and detailed characterization is

currently under way. Increasing the machine's load however, revealed the negative effects of sparking, however, the freewheeling diode addition mitigated that in one direction. Bidirectional operation is a topic of future work and can make use of the soft commutation principles described above.

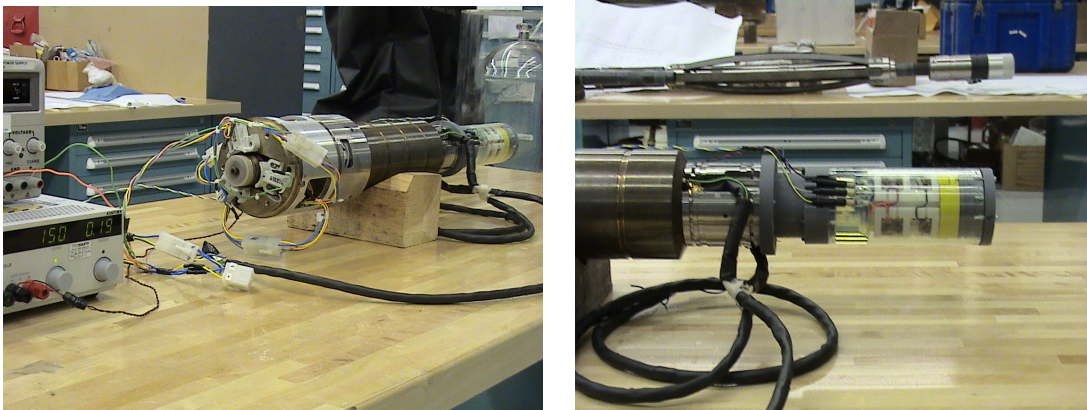


Fig. 6.22 Second prototype of the commutator installed on the resolver side of the motor

## 6.10 Conclusion and Recommendations

A novel system for brushless motor commutation and control was presented in this chapter. This task is most commonly accomplished using an electronic motor drive. One of the main contributors to the development costs of an electromechanical project can be the development of the motor drive. This is especially true in downhole tool development where the harsh environmental conditions limit the application of commercially available electronics. This was clearly demonstrated in the first section of the dissertation. The objective of this novel principle is to reduce or eliminate the need for power conversion electronics and control electronics used in brushless motor

commutation and control for operation under elevated temperatures. Which will in turn reduce project development time and costs.

The work at hand presented a novel solution that can be of great value in the development of downhole tools. It would be an ideal candidate for a project where a monocable (single conductor) operation is a big market entry barrier, and emphasis is placed on extreme temperature and compactness. It would also be an ideal candidate for projects aimed at multiconductor cables where the project team has decided to use induction motors with a maximum efficiency of 65% in some cases to eliminate the need for an electronic controller down hole. The proposed solution would in such a case increase the system efficiency allowing the tool to meet full specifications. The technical challenges were illustrated and possible solutions paths for future development were outlined.

## **CHAPTER VII**

### **CONCLUSIONS AND FUTURE WORK**

#### **7.1 Dissertation Conclusions**

In conclusion, it is safe to say that the research proposed as the subject of this dissertation provided an essential contribution to current research in the field of compact harsh environment energy conversion systems. A comprehensive study of the previous literature presented in the area has been thoroughly carried out. The significance of the research in solving current practical industry needs has been stressed. A need for future research in this area can highly benefit from the recommendations and conclusions made in this work. The work can be seen as divided into three main areas:

1. Electromechanical subsystems
2. Power electronic subsystems
3. A novel energy conversion system development that benefits from the understanding of the first two subsystems and an appreciation of the operating environment.

In chapter II, the influence of the operating environment is shown to play an important role in the design of electrical machines. This fact was illustrated in this work by investigating the design of a permanent magnet synchronous machine submersed in a viscous fluid. The work was prompted by a significant difference between an experimental setup tested in air and one tested in oil. After compiling the results of current literature into a machine design optimization algorithm, analytical and CFD analysis of the submersible machine was also presented. The need to use CFD for the estimation of the viscous loss component was demonstrated by the inadequacy of the

analytical solutions in the presence of the turbulent flow properties of the fluid present in the air gap. Different factors that affect the viscous loss component were analyzed in detail. An iterative machine design procedure is then presented as a complement to the conventional optimization methods.

Chapter III demonstrated the effective utilization of application considerations and the nature of the connected load in the design and application of electrical machines for demanding applications. It is apparent that the application at hand was unique in its utilization of PM machines. The work at hand utilized the available volume and produced a significantly improved actuator. The different phases of the actuator improvement were discussed. This was concluded with the design of a dual winding or six phase PM actuator. The coupling between the two sets of windings was used in favor of the application. A dynamic model of the dual winding exterior rotor PM actuator was developed along with a d-q steady state one. The advantage of utilizing the coupling between the sets of windings for the application was demonstrated using the dynamic model. Experimental results corroborating the presented theory and simulations demonstrated the effectiveness of the presented theory. The utilization of a dual winding machine for the application produced significant improvements in the braking torque capability of the brake winding. This was mainly due to the ability to eliminate two sets of end windings and effectively utilize the original actuator volume.

The second part of the dissertation starts on chapter IV. An investigation into compact harsh environment power electronic systems is presented. The stringent needs of the oil well logging industry on the power electronic conversion systems used was the main driver for the work at hand. Because of the compact nature of such systems, the

ability to operate without the need for active cooling is seen as a critical technology. This can only be achieved using a combination of good device selection, topology design, and material selection. The research started by assessment of the basic device choices and their application at elevated temperature. The interaction of the selected devices in the basic switching unit is then studied and a mitigation technique for the experienced failure mode was presented. This was justified with experimental and simulation results. To enable the operation at higher power, a custom power module is designed based on extensive thermal simulations.

Chapter V built on the knowledge and testing results of chapter IV, and illustrated the need for using multilevel power converters to deliver higher power to down hole tools. During the progress of the work, both dc-dc and dc-ac converters were developed and tested. The major discussion presented in the chapter is related to the development of a multilevel PMSM motor drive. A verified SVPWM algorithm from literature was used, and simulation and experimental results verified its potential. The series blocking diode overvoltage failure mode and the capacitor packaging constraints were seen as the main challenges to a high temperature compact application. The passive mitigation technique previously proposed also proved successful in the multilevel inverter case where voltage values across the diode reached full bus voltage during the deadtime and was the cause of significant failures. The use of Mosfet devices enabled the increase of the switching frequency to a limit that enabled the successful packaging of the flying capacitors and the operation at the rated power levels even with the limited capacitance value seen at elevated temperature.

In chapter VI, a novel system for brushless motor commutation and control was presented. The objective of this novel principle is to reduce or eliminate the need for power conversion electronics and control electronics used in brushless motor commutation and control for operation under elevated temperatures. Although such environments would benefit from the simplicity of using a conventional dc motor, the challenges faced would inhibit this. The thought process involved and all the system's components were presented. Simulation and experimental results were used to verify the presented theory. A prototype mechanical commutator was built and tested with success upto 2000 rpm. The technical challenges faced were illustrated and possible solutions paths were introduced.

## **7.2 Recommendations for Future Work**

The dissertation addressed challenges and novel solutions of many of the main components in a harsh environment energy conversion system. This section will provide a set of recommendations for future work in the different areas addressed.

The work in chapter II can trigger further research into coupled field analysis and optimization of electrical machines. It was shown that analytical solutions may not prove adequate due to the properties of the fluid in the air gap. Although it may be difficult to derive a general closed form equation for such flow, the derivation of an empirical formula for the simple geometries featured in motor design may be possible.

Dual winding machines have long been used in many high power applications like railroad traction and power generation. However, the novel use of the six phase or dual winding machine presented in chapter III may trigger other novel uses of such machines.

Areas such as automotive and aerospace are possible candidates. The compact nature of such systems may prompt the need for such machines.

Chapter IV presented a very active area of research that is of great interest to the automotive and aerospace industries. Qualification of new devices outside the realm of manufacturer specification is a continuous research and development need. SiC technology tested as part of this work may not be the current state of the art. Feedback from our study alone has prompted some manufacturers to improve their devices. Thus, further testing is needed for late market entries. A systematic means of derating power components would also be of great benefit. This would help in designing predictive maintenance systems that would be used to replace such components before a costly failure in the field.

The implementation of the algebraic SVPWM in chapter V was carried out on a DSP. A digital logic implementation would be of benefit. The extension of the algorithm to more than three levels is also an area of interest. The current device rating of 800 V prevents safe, reliable operation of the downhole power system beyond about 1.1 kV. A higher level extension of the algorithm combined with an FPGA implementation can provide a much more reliable system for elevated temperatures.

The novel solution for an elevated temperature motor drive system presented in chapter VI requires comprehensive testing at elevated temperatures and higher voltages. This was limited because all the parts of the prototype were made of printed plastic. The operation at higher voltages and currents requires novel means of suppressing arcs occurring due to the current interruption. The current solution of using free wheeling diodes, although acceptable, does not provide bidirectional operation.

## REFERENCES

- [1] G. R. Slemon, "On the design of high-performance surface-mounted PM motors," *IEEE Trans. Industry Applications*, vol. 30, No. 1, pp. 134-140, Jan. - Feb. 1994.
- [2] T. A. Lipo, *Introduction to AC Machine Design*, 1<sup>st</sup> edition, Madison, WI: WisPERC, 1999.
- [3] R. B. Bird, E. N. Lightfoot, W. E. Stewart, *Transport Phenomena*, 2<sup>nd</sup> edition, New York: John Wiley & Sons Inc, 2002.
- [4] F. P. Incropera, D. P. Dewitt, T. L. Bergman, A. S. Lavine, *Introduction to Heat Transfer*, New York: John Wiley & Sons Inc, 2006.
- [5] *Fluent Users Manual*, Fluent Corp., Lebanon, NH, 2004.
- [6] *Fluent Training Manual*, Fluent Corp., Lebanon, NH, 2005.
- [7] M. Negrea, and M. Rosu, "Thermal analysis of large permanent magnet synchronous motor for different permanent magnet rotor configurations," in *Proc. 2001 IEEE International Electrical Machines and Drives Conf.*, Cambridge, MA, pp. 777-781.
- [8] J. Driesen, R. Belmans, and K. Hameyer, "Methodologies for coupled transient electromagnetic-thermal finite element modeling of electrical energy transducers," *IEEE Trans. Industry Applications*, vol. 38, No. 5, pp. 1244-1250, Sept.-Oct. 2002.
- [9] D. J. Perreault, and V. Caliskan, "Automotive power generation and control," *IEEE Trans. on Power Electronics*, vol. 19, No. 3, pp. 618-630, May 2004.
- [10] T. E. Heikkila, "Permanent magnet synchronous motor for industrial inverter applications: Analysis and design," Ph.D. dissertation, Dept. Elect. Eng., Lappeenranta Teknillinen Korkeakoulu (Helsinki), Finland, 2003.
- [11] P. J. Lampola, "Directly driven, low-speed permanent-magnet generators for wind power applications," Ph.D. dissertation, Dept. Elect. Eng., Teknillinen Korkeakoulu (Helsinki), Finland, 2000.
- [12] E. F. Fuchs, and L. T. Rosenberg, "Analysis of an alternator with two displaced stator windings," *IEEE Trans. Power App. Syst.*, vol. PAS-93, pp. 1776-1786, Jan 27-Feb 1, 1974.

- [13] A. Arkadan, T. Hijazi, and N. Demerdash, "Computer-aided modeling of a rectified dc load-permanent magnet generator system with multiple damper windings in the natural abc frame of reference," *IEEE Trans. on Energy Conversion*, vol. 4, No. 3, pp. 518-525, Sept. 1989.
- [14] R. F. Schiferl and C. M. Ong, "Six phase synchronous machine with AC and DC stator connections part I: Equivalent circuit representation and steady state analysis," *IEEE Trans. Power App. Syst.*, vol. PAS-102, pp. 2685-2693, August 1983.
- [15] R. M. Nelms, and R. W. Johnson, "200°C operation of a 500-W DC-DC converter utilizing power Mosfets," *IEEE Trans. on Industry Applications*, vol. 33, No. 5, pp. 1267-1272, Sept./Oct. 1997.
- [16] R. W. Johnson, J. R. Bromstead, and G. B. Weir, "200°C operation of semiconductor power devices," *IEEE Trans. on Components, Hybrids, and Manufacturing Technology*, vol. 16, No. 7, pp. 759-764, Nov. 1993.
- [17] C. V. Godbold, and J. L. Hudgins, "Temperature variation effects in MCTs, IGBTs, and BMFETs," in *Proc. 1993 IEEE Power Electronics Specialists Conf.*, Acapulco, Mexico, pp. 93-98.
- [18] P. McCluskey, R. R. Grzybowski, L. Condra, D. Das, J. Fink, J. Jordan, T. Torri, "Reliability concerns in high temperature electronic systems," in *Proc. 1998 IEEE High Temperature Electronic Materials, Devices and Sensors Conf.*, Boston, MA, pp. 199-206.
- [19] A. M. Abou-Alfotouh, "Characterization of silicon carbide power semiconductor schottky diodes and JFETs for high-switching frequency applications," Ph.D. dissertation, Dept. Elect. Eng., University of Kentucky, Lexington, 2004.
- [20] P. J. Vivierge, J. J. Rousseau, J. P. Chante, and B. Allard, "Low power converter for high temperature applications," in *Proc. 1993 European Conference on Power Electronics and Applications.*, Clamart, France, pp. 232-236.
- [21] Y. F. Pang, "Assessment of thermal behavior and development of thermal design guidelines for integrated power electronics modules," Ph.D. dissertation, Dept. Elect. Eng., Virginia Tech, Blacksburg, 2005.
- [22] Q. Zhao, and G. Stojcic, "Characterization of  $c dv/dt$  induced power loss in synchronous buck DC-DC converters," in *Proc. 2004 IEEE Applied Power Electronics Conf.*, Anaheim, CA, pp. 292-297.

- [23] B. Ozpineci, "System impact of silicon carbide power electronics on hybrid electric vehicle applications," Ph.D. dissertation, Dept. Elect. Eng., The University of Tennessee, Knoxville, 2002.
- [24] W. A. Tabisz, M. M. Jovanovic, and F. C. Lee, "Present and future of distributed power systems," in *Proc. 1992 IEEE Applied Power Electronics Conf.*, Anaheim, CA, pp. 11-18.
- [25] M. Belkhat, R. Cooley, and A. Witulski, "Large signal stability criteria for distributed systems with constant power load," in *Proc. 1990 IEEE Power Electronics Specialists Conf.*, Atlanta, GA, pp. 1333-1338.
- [26] V. Rajasekaran, and B. S. Heck, "On stability enhancing control methods in power electronic converters," in *Proc. 2002 Power Electronics Specialists Conf.*, Cairns, Australia, pp. 1593-1598.
- [27] T. Bruckner, S. Bernet, and H. Guldner, "The active NPC converter and its loss-balancing control," *IEEE Trans. on Industrial Electronics*, vol. 52, No. 3, pp. 855-868, June 2005.
- [28] M.A.S. Mendes, Z.M.A. Piexoto, P.F. Seixas, and P Donoso-Garcia, "A space vector PWM method for three-level flying capacitor inverters," in *Proc. 2001 Power Electronics Specialists Conf.*, Vancouver, Canada, pp. 182-187.
- [29] A. K. Gupta, and A. M. Khambadkone, "A space vector PWM scheme for multilevel inverters based on two-level space vector PWM," *IEEE Trans. on Industrial Electronics*, vol. 53, No. 5, pp. 1631-1639, June 2005.
- [30] J. Huang, and K. A. Corzine, "Extended Operation of flying capacitor multilevel inverters," *IEEE Trans. on Power Electronics*, vol. 21, No. 1, pp. 140-147, Jan. 2006.
- [31] A. Nabae, I. Takahashi, and H. Akagi, "A new neutral-point-clamped PWM inverter," *IEEE Trans. on Industry Applications*, vol. IA-17, pp. 518-523, Sept./Oct. 1981.
- [32] J. K. Steinke, "Control strategy for a three phase ac traction drive with a 3-level GTO PWM inverter," in *Proc. 1988 IEEE Power Electronics Specialists Conf.*, Reno, NV, pp. 431-438.
- [33] D. W. McGaughey, "Apparatus and method of mechanically commutating a brushless motor," U.S. Patent 6,239,531, May 29, 2001.
- [34] W. A. Pengov, "Mechanically commutated switched reluctance motor," World Patent WO 01/50578 A1, July 12, 2001.

- [35] T. M. Bui, "Mechanically commutated DC motor," U.S. Patent 6,667,564, Dec. 23, 2003.
- [36] M. Liwschitz-Garik, and R. T. Weil, *D-C and A-C Machines Based on Fundamental Laws*, Ann Arbor, MI: D. Van Nostrand Company, 1952.
- [37] J. S. Hsu, "Soft commutated direct current motor," in *Proc. 1998 Power Electronics in Transportation Conf.*, Dearborn, MI, pp. 95-102.
- [38] R. C. Perrine Sr., *Design Handbook for PM Motors and Tachometers*, Lebanon, OH: Magna Physics Publishing Div. of Motorsoft, 2000.
- [39] M. H. Nagrial, "Analysis, design and performance of magnetic couplings," in *Proc. 1995, International Conference on Power Electronics and Drive Systems*, Orlando, FL, pp. 634-638.

## APPENDIX A

### IRON LOSS CALCULATION METHOD

Calculation of the lamination material core loss is one of the considerations in a new motor design. The eddy and hysteresis coefficients are required in the calculation of the iron loss. These coefficients are obtained here from curve fitting of several manufacturer data points. The following set of equations, provide a detailed step by step method for calculating the iron losses of a lamination material. The calculations, however, do not include the effect of voltage harmonics produced by the PWM inverter switching, however, provide a reasonable approximation of the losses. The calculations were implemented in Mathcad.

Iron loss calculation constants:

$$\rho_{M19} = 7.639 \text{ gm/cm}^3$$

$$line = \frac{1}{6.452} \text{ gauss} \cdot \text{in}^2$$

$$Lam\_wt = 1 \text{ lb}$$

$$B = 12000 \text{ gauss}$$

$$f = 240 \text{ Hz}$$

$$t = 0.014 \text{ in (actual lam thickness)}$$

Selection of three power points from the material datasheets:

$$d = 0.014 \text{ in (Basis thickness for Epstein values)}$$

$$P_1 = 0.85 \frac{W}{lb} \quad f_1 = 100 \text{ Hz} \quad B_1 = 8000 \text{ gauss}$$

$$P_2 = 53 \frac{W}{lb} \quad f_2 = 1000 \text{ Hz} \quad B_2 = 12000 \text{ gauss}$$

$$P_3 = 1.86 \frac{W}{lb} \quad f_3 = 100 \text{ Hz} \quad B_3 = 12000 \text{ gauss}$$

Let core volume/10 = A

$$A = \frac{Lam - wt}{\rho_{M19} \cdot 10} = 5.938 \times 10^{-6} m^3$$

$$a = \frac{f_2}{f_1} = 10$$

$$C = \left( A \cdot d^2 \right) \frac{1.645}{10^5} = 0.012 \text{ mm}^5$$

Calculate hysteresis exponent:

$$x = \frac{\log \left[ \frac{B_2^2 \cdot (P_2 - a^2 P_3)}{B_2^2 \cdot a \cdot P_1 \cdot (1-a) + B_1^2 (P_2 - a \cdot P_3)} \right]}{\log \left( \frac{B_2}{B_1} \right)} = 1.914$$

Calculate the eddy current coefficient:

$$\lambda = \frac{(P_2 \cdot B_1^x - a \cdot P_1 \cdot B_2^x)}{\left[ \frac{C \cdot f_2^2}{a} \right] \cdot (a \cdot B_2^2 \cdot B_1^x - B_1^2 \cdot B_2^x)}$$

$$= 4.738 \times 10^{12} \frac{s^3 A^2}{kg^2 m^3}$$

and

$$\lambda \cdot C = 5.852 \times 10^{-5} \frac{m^2 s^3 A^2}{kg^2}$$

Calculate the hysteresis coefficient:

$$\eta = \frac{P_3 - (f_1^2 \cdot \lambda \cdot C \cdot B_2^2)}{f_1 \cdot A \cdot B_2^x}$$

$$= 3.871 \times 10^3 \frac{s^{1.828} \cdot A^{1.914}}{kg^{1.914} \cdot m}$$

Hysteresis losses per pound:

$$P_{hys} = f \cdot B^x \cdot A \cdot \eta = 3.547 \frac{W}{lb}$$

Eddy Current losses per pound:

$$P_{eddy} = f^2 \cdot B^2 \cdot C \cdot \lambda \cdot \left( \frac{t^2}{d^2} \right) = 2.202 \frac{W}{lb}$$

Total Iron Loss:

$$P_{total} = (P_{eddy} + P_{hys}) \cdot Lam\_wt = 5.748 W$$

**VITA**

Name: Shehab Ahmed

Address: 111A Zachry Engineering Center  
Dept. of Electrical Engineering  
Texas A&M University  
College Station, TX 77843-3128  
USA

Educational Background:

B.S. in Elec. Engineering, Alexandria University, Alexandria, Egypt 1999.

M.S. in Elec. Engineering, Texas A&M University, College Station, TX 2000.

Ph.D. in Elec. Engineering, Texas A&M University, College Station, TX 2007.